Electro-Luminescent and Photovoltaic Responses of poly (propylene imine) dendritic CuInSe₂ (CIS) Quantum Dots

By

Muziwenkosi Memela

(BSc Honours)

A thesis submitted in partial fulfilment of the requirements for the degree

of

MAGISTER SCIENTIAE IN NANOSCIENCE

In the

Faculty of Science
University of the Western Cape, South Africa

Supervisor: Prof Emmanuel Iwuoha

Co-supervisors: Dr Usisipho Feleni

December 2019

i

ABSTRACT

The development of renewable energy has attracted more attention due to the increasingly serious energy and environmental crisis in the world nowadays. Second generation photovoltaics based on thin films of binary semiconductor nanocrystals such as cadmium sulphide (CdS), cadmium selenide (CdSe), cadmium telluride (CdTe), lead sulphide (PbS) and lead selenide (PdSe), have shown considerable potential with their power conversion efficiencies (PCEs) improving from 0,1 % to about 6-7% within a space of 2 years. However, they have failed to surpass the efficiency of silicon solar cells and their lower efficiency has resulted in the overall cost of the second-generation photovoltaics to be similar to silicon solar cells, thus limiting their domestic and commercial use. For this reason, efforts have been made through the third-generation solar cells to improve efficiencies while lowering the production costs through simple processing technologies. Copper indium selenide (CuInSe$_2$) based quantum dots (QDs), are perceived to be a promising alternative to those cadmium or lead chalcogenide based QDs in serving as light-harvesting sensitizer materials in hybrid solar cells due to their near-infrared (NIR) absorbing capacity and low toxicity. Hence, in this present study, we report the synthesis of electroactive copper indium selenide quantum dots (CuInSe$_2$ QDs) capped with generation 1 poly (propylene thiophene) (G1PPT) dendrimer with a high potential for photovoltaic application, via hot injection method. The synthesis of G1PPT-CuInSe$_2$ QDs commenced with the functionalization of generation 1 polypropylenimine tetramine dendrimer (G1PPI) into G1PPT via Schiff condensation in reaction flask with 2-Thiophenecarboxaldehyde under an inert N$_2$ environment. Proton nuclear magnetic resonance spectroscopy (^{1}H-NMR) and Fourie transform infrared spectroscopy (FT-IR) confirmed the successful transformation of G1PPI into G1PPT. The G1PPI was functionalized in order to improve its surface passivating and electron donating effects. Besides preventing nanoparticles agglomeration, the modification of nanocrystal

surface by organic ligands such as dendrimers is a useful tool for enhancing their luminescent quantum yields and photophysical properties due to their unique structural qualities, dendritic effect and polydentate nature ^{1}H-NMR gave rise to a new chemical shift at 8.31 ppm for N=C-H, which confirmed the incorporation of 2-Thiophenecarboxaldehyde into the G1-PPI dendrimer structure and FT-IR showed that strong bands appeared at 1673 cm^{-1} for N=C in the dendrimer moiety, and 755 cm^{-1} for C-H at α-position of the thiophene ring. Cyclic Voltammetry of G1PPT displayed no distinct oxidation or reduction peaks. An increase in current was observed for the G1PPI modified electrode over the bare GCE owing to the nano-dimensional nature of PPI which increases the surface area of the electrode. The dependence of peak current and potential on scan rate (ν) from 10 to 50 mVs^{-1} a linear relationship, suggesting that the kinetics are diffusion controlled on the G1PPI modified electrode. Optical, microscopic and electrochemical studies were performed on the G1PPT-$CuInSe_2$ QDs. HR-TEM images revealed continuous lattice fringes and very clear crystal facets for the pentagonal shaped nanocrystals with an average size of 8.5 nm. The crystallinity was further confirmed from the SAED pattern, which also exhibited multiple diffraction rings corresponding to CISe. UV-vis spectroscopy showed gradual shift towards longer wavelengths from 713 nm to 784 nm for the G1PPT-$CuInSe_2$ QDs with an optical bandgap of 1.51 eV determined from Tauc plots extrapolation. XRD pattern gave rise to Bragg's reflections at 2θ value of 27,71°, 46,39°, 54,63° representing (111), (220) and (311) planes of the zincblende metastable structure of $CuInSe_2$ with a crystal diameter of 6.3 nm. The HOMO and LUMO levels of the G1PPT-$CuInSe_2$ QDs calculated from cyclic voltammetry (CV) were -5.140 eV and -3.537 eV, respectively. The corresponding electrochemical bandgap (E_{gap}^{el}) and the electron-hole Coulomb interaction energy $J_{e,h}$ were found to be 1.60 eV and 90 meV respectively.

KEYWORDS

Electroluminescent

Energy bandgap, Eg

G1PPT-CunInSe$_2$ QDs

HOMO

LUMO

Quantum dots (QDs)

Solar cells

ABBREVIATIONS

Carbon dioxide (CO2)

Copper Indium Diselenide (CuInSe2)

Copper Indium Sulfide (CIS)

CuInSe2 (CISe/CIS)

Cyclic voltammetry (CV)

Cyclotriphosphazene (PMMH)

Dendrimer-encapsulated (DE)

Dichloromethane (DCM)

Electrochemical impedance spectroscopy (EIS)

Fourier transform X-ray spectroscopy (FTIR)

Full widths at half maximum (FWHM)

Generation 1 Poly(propylene thiopheneimine) dendrimerG1PPT

Hard-soft acid-base (HSAB)

Highest occupied energy level (HOMO)

High-resolution transmission electron microscopy (HR-TEM)

Lowest unoccupied energy level (LUMO)

Multiple exciton generation (MEG)

Multifunctional Nanoparticles (MNPs)

Nanocrystals (NCs)

Nanoparticles (NPs)

Near-infrared (NIR)

Nuclear magnetic resonance spectroscopy (NMR)

Octadecene (ODE)

Octylamine (OctAm)

Oleylamine (OlAm)

Particulate Matters (PM)

Power conversion efficiences (PCEs)

Photoluminescence quantum yield (PLQY)

Poly(amidoamine), or PAMAM

Poly (propylene imine) densrimer (PPI)

Polyamidoamine dendrimers cappe

d-carbon dots (PAMAM-CDs)

Photoluminescence (PL)

Photovoltaics (PVs)

Quantum dots (QDs)

Quantum dot solar cells (QDSCs)

Quantum Yield (QY)

Tetrabutylammonium perchlorate (TBAClO4)

Trioctylphosphine-selenide (TOPSe)

Trioctylphosphine oxide (TOPO)

Ultraviolet-visible spectroscopy (UV)

X-ray diffraction (XRD)

Zinc stearate (ZnSt$_2$)

1-dodecanethiol (DDT)

DECLARATION

I declare that **Electro-Luminescent and Photovoltaic Responses of poly(propylene imine) dendritic CuInSe$_2$ (CIS) Quantum Dots** is my own work, that it has not been submitted before for any degree or examination in any other university, and that all the sources I have used or quoted have been indicated and acknowledged as complete references.

Signature ---------------------------------

Muziwenkosi Memela   **15 December 2019**

UNIVERSITY *of the*
WESTERN CAPE

DEDICATION

This work is dedicated to: my late father M.P. Memela and my mother N.E. Memela, who has been my strength, my pillar, and light throughout many difficult times; to my beautiful daughter and my future wife; my late brother I. S. Memela who I lost tragically earlier this year and the rest of my family and extended family.

ACKNOWLEDGEMENTS

Wholesome gratitude to God almighty for giving me the strength to bring this work to completion.

A special thanks to my supervisor, Prof. Emmanuel Iwuoha, who has been my guide, my support structure and who kept believing in me even when I did not believe in myself.

I am grateful to my family and my friends for their unwavering support and faith in me throughout my studies.

To Chemistry Department staff and SensorLab researchers, thank you for your friendship and support.

TABLE OF CONTENTS

Section	*Page*

LIST OF FIGURES

LIST OF SCHEMES

LIST OF TABLES

xvii

CHAPTER 1:

INTRODUCTION

1.1   Background

The modern world economy is built upon the substantial use of fossil fuels which has brought about a great convenience in people's lives. The consumption rate of fossil fuels has seen an exponential increase over the years due to the increasing world population, which has caused an imbalance in the energy supply versus demand. In addition, the expandable use of fossil fuels such as oil, coal and natural gases also pollutes the atmosphere greatly through the release of greenhouse gases such as CO_2; challenging the sustainable development of human society [1–4]. The CO_2 levels in the atmosphere have risen to > 400 ppm today from 278 ppm since the beginning of the industrial revolution. Other environmentally detrimental pollutants such as SO_x, NO_x, particulate matters (PM), volatile organic compounds and toxic heavy metals are also released during the combustion of fossil fuels. These pollutants have caused a significant change in the climate of the earth, which has led to global warming heat waves, droughts, torrential rainfalls and accompanying floods. Therefore, growing concerns for human health and the environment has led researchers in the scientific community to turn to renewable energy as a viable solution [5–8].

Renewable energy sources are the primary, domestic and clean or inexhaustible energy resources and they include wind, biomass, solar, hydropower, and geothermal. They possess great potential because in principle they can meet the world's energy demand many times over compared to conventional energy sources. Photovoltaic and wind power systems are the focus today because their costs have declined greatly in the last 30 years while oil and

1

gas costs fluctuate continuously [9, 10]. Photovoltaics (PVs) devices are more prevalent and superior in fostering green energy consumption and overcoming environmental impact caused by current energy sources. Solar energy is preferred and mostly used because of its global availability and low environmental impact. There are three subdivisions of the photovoltaics cells and they include first, second, and third generations. The first generation of PVs is largely made up of pure single-crystalline silicon materials. They have high efficiencies, which makes them leaders in the solar cell industry. They are, however, too expensive due to production steps and for this reason, researchers have continued searching for a new technology that will target the reduction of materials cost and overall production steps. Second generation PVs are slightly cheaper to manufacture compared to generation one PVs and are associated with thin-film solar cell designs that use minimal materials. They were developed to combat the issue of the high cost of the 1st generation PVs, but because of low efficiencies and overall costs that lean closer to that of the 1st generation, researchers have turned to third-generation PVs which aim to produce low-cost solar cells with high efficiencies. Third-generation solar cell technologies include but are not limited to multi-junction photovoltaic cells, tandem cells and nanocrystals-based cells [10–13].

The global photovoltaic industry growth is largely affected by the different materials used. Photovoltaic devices are being developed based on their principal component which is the active layer. Semiconductor nanocrystals quantum dots (QDs) have features that make them leading candidates for application in active layer development and overall solar performance for 3rd generation photovoltaics. A widespread of research has been carried out on II-IV semiconductor sensitizers such as cadmium sulphide (CdS), cadmium selenide (CdSe), and cadmium telluride (CdTe) for application in quantum dot solar cells (QDSCs). The considerable attention they have received is due to their unique properties such as ease of

2

fabrication, tunable energy bandgap through size control and possible multiple exciton generation (MEG). The use of toxic precursors in this kind of material has, however, restricted their application [10, 14, 15]. The conduction band position and the size of semiconductor sensitizers are critical to achieving efficient charge separation in QDSCs and broad light harvesting, and this, in turn, depends on the complete alignment between semiconductor sensitizer and a layer of metal oxide, i.e. titanium oxide (TiO_2). These two requirements are generally difficult to achieve and therefore tuning of electronic and optical properties of QDs purely by changing their particle sizes has its limitations. In addition, the low to moderate power conversion efficiencies (PCEs) of these binary semiconductor sensitizers loiter due to their poor charge injection efficiency [16, 17].

Ternary semiconductor QDs tailored through alloying have emerged as leading alternatives for binary QDs in the quest to mitigate the above-mentioned challenges. They are made up of elements from groups I, III, and VI, such as copper, gallium, indium, sulfur, selenium, and tellurium. The physical and optical properties of ternary QDs depend on size and composition, and this, therefore, makes them superior to their binary counterpart parts because the desired bandgap can possibly be achieved by varying stoichiometric ratios while keeping the particle size constant [18–20]. Their tunable optical band gap covers a wide range of wavelengths from near-infrared (NIR) through the visible spectrum, to the ultraviolet spectrum. They exhibit unique chemical and physical properties including larger Stokes shifts and a longer photoluminescence lifetime. In addition to these advantages, alloyed QDs offer a "green" route to highly efficient QDSCs since less toxic precursors are utilized [21].

The first synthesis of type I-III-VI colloidal chalcopyrite $CuInS_2$ (CIS) QDs prepared by the thermal decomposition of the molecular single-source precursor (PPh3)2CuIn(SEt)4 in the presence of hexanethiol above 200°C was reported by Castro et al, in 2014. Since then, several publications of I-III-VI type colloidal QDs with improved performances and more "greener" synthesis routes have been realized. For example, by varying the relative reactivity of copper and indium precursors in a non-coordinating solvent, Peng et al were able to develop a green synthesis route for the nearly monodisperse $CuInS_2$ semiconductor nanocrystals in 2009. The $CuInS_2$ QDs prepared exhibited an emission peak position tuneable from 500 to 950 nm, and the same synthesis was also used to synthesize $AgInS_2$ nanocrystals which produced similar results [21]. Other synthetic methods for the preparation of I-III-VI type QDs developed over the years include but are not limited to hot-injection [22, 23], solvothermal [24], thermal decomposition [25]–[27], hydrothermal [28] and very recently microwave irradiation/assisted synthesis[15, 29–31]. Several studies have demonstrated that the synthesis of nanocrystals via microwave-assisted synthesis was generally faster, simpler, and very energy efficient [15]. However, the particles prepared by Hosseinpour-Mashkani *et al* [32] using microwave irradiation for their studies on the effect of preparation parameters such as microwave power, irradiation time, and type of copper precursor on the particle size of the products, suffered from severe agglomeration. In this study I-III-VI type QDs namely; copper indium selenide ($CuInSe_2$) were prepared in a non-coordinating solvent using poly generation 1 (propylene thiopheneimine) dendrimer (G1PPT) as a capping agent via hot-injection method.

4

1.2   Problem statement

With the increasing urgent need for versatile materials with power conversion efficiencies (PCEs) exceeding the Shockley−Queisser limit of 32% in solar cell applications [32, 33], a variety of research has been carried out on second-generation photovoltaics based on semiconductor nanocrystals such as CdS, CdSe, CdTe and Pd-based (PbS, PdSe) types. These materials demonstrate broad absorption, hot electron extraction and multiple exciton generation (MEG), and addition their PCEs were improved from 0,1 % to about 6-7% within a space of 2 years [34–38], however, they have failed to surpass the efficiency of silicon solar cells. The lower efficiency of second-generation photovoltaics based on these materials has resulted in their overall cost to be similar to silicon solar cells, thus limiting their domestic and commercial use. In addition, the utilization of highly toxic precursors such as cadmium and lead further limits their commercial use due to environmental health concerns. Hence, efforts have been made through the third-generation solar cells to improve efficiencies while lowering the production costs through simple processing technologies. The exploration of new materials with new properties may be an advantage in improving the performance of photovoltaic devices and expending the associated technology.

1.3   Project motivation

South Africa is one of the leading coal export nations worldwide. Notably, in 2014 the share of coal in its basic energy consumption was 70%, which is far greater than the global average of 30%. In addition, 92% of the country's power generation is based on the traditional production of coal [39]. It is then clear from these numbers that coal plays a significant role in the economy of South Africa. However, coal is a limited resource and is facing depletion due to population increase and increased energy demands. Nationally and globally, coal also

has major concerns associated with carbon dioxide (CO_2) emissions which as a major player in climate change and global warming. This, therefore, calls for an urgent need for efficient, clean and sustainable energy systems. Studies have indicated that solar and wind power systems are the two primary sources of renewable energy. The global availability of energy from the sun and the low environmental impact of solar power systems makes them by far the most preferable and widely researched. Efforts have been made through the third-generation solar cells to improve efficiencies while lowering the production costs through simple processing technologies. Semiconductor nanocrystals such as quantum dots exhibit excellent optical, electronic and photo-physical properties compared to their quantum wells counterparts due to three-dimensional quantum confinement. Their unique properties make it possible to design their bandgaps by manipulating their size and shape, and very recently ternary quantum dots have opened stoichiometric manipulation as another property to engineer the bandgap. In addition, small amounts of these materials can easily be utilized along with other different materials such as polymers and other inorganic materials to produce hybrid structures and in this way, make it possible to develop low-cost nanocrystals solution based-thin photovoltaic devices which are highly efficient.

This research work involved the synthesis and investigation of photovoltaic properties of $CuInSe_2$ QDs capped with generation 1 poly (propylene imine) dendrimer that was previously functionalized with 2-thiophenecarboxaldehyde. The $CuInSe_2$ QDs were synthesized via the organic phase high-temperature route in a noncoordinating solvent. For morphological analysis, the QDs were characterized by high-resolution transmission electron microscopy (HR-TEM). The structure and bonding were investigated using X-ray diffraction (XRD), nuclear magnetic resonance spectroscopy (NMR), Small angle X-ray Scattering (SAXS), Fourier transform X-ray spectroscopy (FTIR) and Raman spectroscopy.

Ultraviolet-visible spectroscopy (UV) and photoluminescence (PL) will be used to access the photo-physics of the materials while their electron transfer and charge transfer properties will be studied with cyclic voltammetry (CV) and electrochemical impedance spectroscopy (EIS).

1.4 Project aims and objectives

The goal of this project was based on the preparation and characterisation of $CuInSe_2$ quantum dots and possibly apply them for photovoltaic responses. The first part involved the functionalization of G1-poly (propylene imine) dendrimer with thiophene. Subsequently, the functionalised G1-PPI was employed in the preparation of $CuInSe_2$ QDs in a noncoordinating solvent. To fulfill the above, the following objectives were identified:

- Functionalization and characterization of generation one poly (propylene imine) dendrimer with 2-Thiophenecarboxaldehyde.

- Synthesis of poly (propylene thiopheneimine) dendritic $CuInSe_2$ (CIS) QDs using the hot-injection method

- Characterization of poly (propylene thiopheneimine) dendritic $CuInSe_2$ (CIS) QDs using a number of techniques such as UV-vis, HR-TEM, XRD, CV, SAXS among others

1.5   Thesis Layout

This thesis is presented in five chapters.

Chapter 1: Gives brief background information on the project, problem statement, and motivation as well as aims and objectives.

Chapter 2: Provides a detailed literature review.

Chapter 3: Provides a brief background on dendrimers and their application, spectroscopic, morphological and electrochemical results obtained from functionalization of g1 poly (propylene imine) dendrimer with 2-Thiophenecarboxaldehyde.

Chapter 4: Provides a brief background of ternary quantum dots and their application in photovoltaics, morphological, spectroscopic and electrochemical results obtained from nanomaterial (G1PPT-CuInSe$_2$ QDs.

Chapter 5: Represents conclusion and recommendations
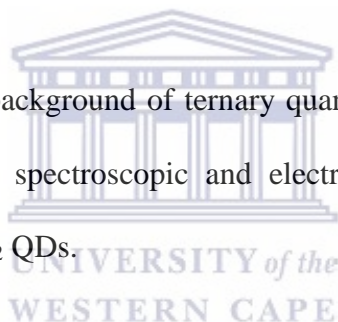
CHAPTER 2:

LITERATURE REVIEW

2.1   Summary
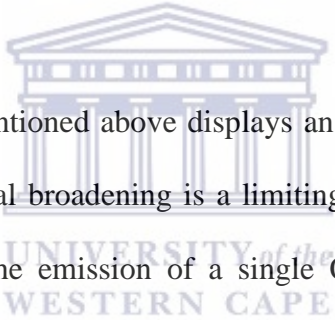
This chapter covers the theory of both binary and ternary semiconductor nanocrystals or quantum dots and their application on photovoltaics. The chapter also covers different synthetic strategies for quantum dots because of the huge role they play on the composition and properties of these materials. It further details the conditions affecting the synthesis and properties of quantum dots. Dendrimers and their application as capping agents are also included in this chapter.

2.2   Semiconductor Nanocrystals

Semiconductor nanocrystals (NCs) (usually referred to as quantum dots) are small crystalline particles within the range of 1-10 nm. Their small size gives rise to material properties that are not comparable to those of corresponding bulk materials because of quantum confinement, which is a phenomenon that occurs when the nanoparticles' size becomes smaller than the exciton Bohr radius of the bulk semiconductor [40]. A downright effect of the 3D confinement is that the energy levels of excitons become discrete and approach molecular behavior as the size of the particle decreases. A spherical quantum box is usually used to describe an ideal quantum dot and will demonstrate an atomic like absorption spectrum. The Schrödinger equation and the effective mass approximation can be used to quantify the energies of the quantized states in the conduction band and valence band. However, the solutions of the equation are difficult to achieve because the electron and hole

9

cannot be considered as mutually independent since they are both confined into a space smaller than the Bohr radius. A decrease in nanoparticle size causes an increased overlap of the confined charge carriers wave functions, resulting in strongly enhanced absorption coefficients. Because photon energy causes an increase in the number of possible transitions, there is a steady increase in the absorption coefficients as the excitation wavelength shifts towards the blue region. Emission processes in QDs are a result of electron-hole recombination and depend intensely on whether the process of recombination is radiative or non-radiative. Non-radiative processes take place mainly at defects located at the surface of nanocrystals. By controlling the surface chemistry and passivation of surface defects, the large surface/volume ratio of QDs allows the achievement of enhanced quantum yields [41], [42].

The ideal quantum dot, as mentioned above displays an atomic-like absorption spectrum, however, in reality, the thermal broadening is a limiting factor in synthetic nanocrystals. Thus, at room temperature, the emission of a single QD can have full widths at half maximum (FWHM) of a few nanometres. Size distribution is, however, the major cause of broadening when it comes to QDs. The emission of a QD is size related, and since the solid particles in colloidal dispersion have different sizes, there is a slight variation in the emission wavelength. For this reason, the emission spectrum of a certain nanocrystal ensemble will be much broader than the individual QDs spectra. Size distributions with a variation lower than 5% are currently possible to obtain. This elucidates into a FWHM of approximately 25-30 nm, which is relatively small compared to the spectral response of many luminescent dyes.

Much of the application of semiconductor nanocrystals on solar cells has focused on CdS, CdSe or PbS and PbSe as the active nanocrystal material layer. Diguna *et al* [43] reported a

CdSe sensitized-type solar cell based on the TiO$_2$ inverse opal with a conversion efficiency of 2.7% under solar illumination of 100 mW/cm^2, which was relatively high at that time. In 2009, Lee and Lo [44] reported a CdS/CdSe co-sensitized photoelectrode for QD-sensitized solar cell application. They compared the two QDs CdS and CdSe, realizing CdS has a higher conduction band edge compared to that of TiO$_2$, which is a much-needed consequence for the perfect injection of hot electrons from CdS. On the other hand, the electron injection efficiency of CdSe is much lower than that of CdS albeit its absorption range can extend to ca.720 nm, and this is because the band edge of CdSe is located below that of TiO$_2$. They took advantage of both CdS and CdSe by using them as co-sensitizers sequentially assembled onto TiO$_2$ thin film, forming a cascade co-sensitized structure and were able to achieve a conversion efficiency of 4,22 %. More recently, Huang *et al* [45] reported a CdS/CdSe quantum dot sensitized solar cell with a conversion efficiency of 7,24% achieved by inserting two ZnSe layers at the interface between CdS/CdSe QDs and the TiO$_2$ electrolyte in order improve light absorption and to suppress charge recombination, which is a hindering factor in achieving high energy conversion efficiencies. Recent progress on PbSe was reported by Zhang *et al* [46], where they applied CsPbBr$_3$ perovskite quantum dot back layer on a PbSe quantum dot solar cell and achieved an efficiency of more than 7,22% accompanied by a fill factor 62,4%. These Cd, Pb-containing QDs based solar cells indeed exhibit excellent photo- and chemical stability, and high PCEs, but the use of toxic heavy metals still restricts their commercial application.

2.3   Ternary I-III-VI Semiconductor Nanocrystals

In the quest to explore low-toxic QDs for PV applications, ternary I-III-VI$_2$ QDs have emerged as leading alternatives due to their high absorption coefficient (~10^5 cm^{-1}) and narrow bandgap properties. For more than a decade, CuInS$_2$ and CuInSe$_2$ have been studied

11

as suitable p-type semiconducting materials for highly efficient thin-film solar cells [47]. They are regarded as better light harvesters compared to their binary counterparts because their bandgap can be fine-tuned by varying stoichiometric ratios while keeping the particle size constant. For example, Pan *et al* [48] were able to effectively passivate the surface of ternary $CuInS_2$ and thereby achieving efficiencies of about 7,04% under AM 1.5G one sun irradiation. However, compared to $CuInS_2$ (CIS), $CuInSe_2$, is regarded as a more promising material due to its larger exciton Bohr radius (~$10.^6$ nm) and narrower bandgap (1.04 *vs*. 1.5 eV of the CIS), which can widen the light-absorbing range to near-infrared (NIR) region [48, 49].

Ternary QDs, like binary QDs have a lot of advantages compared to bulk materials. Their electronic properties and bandgap can be tuned by varying their size, they allow composition tuning and internal structure control prior to materials processing and they use low-cost solution-based methods for deposition on various substrates [50]. Composition and structure control remain one of the biggest challenges in the synthetic chemistry of I-III-VI$_2$ semiconductor nanocrystals. Chalcopyrite semiconductors accommodate a wide range of non-stoichiometry in the bulk state. A good example of this family of compounds is copper indium selenide, which has a phase diagram demonstrating several off-stoichiometric ordered structures, such as $CuIn_5Se_8$, $CuIn_3Se_5$, $Cu_2In_4Se_7$, etc. Cu-In-Se phases, such as $CuIn_3Se_5$ and $CuIn_5Se_8$, exhibit larger optical band gaps (direct, 1.21 and 1.15 eV, respectively). The broadening of the optical band gap is associated with repulsion weakening between Cu d and Se p valence band states, which leads to the lowering of the valence band maximum for In-rich Cu-In-Se materials. In binary semiconductor nanocrystals, the off stoichiometry leads to poor performing devices due to deep trap states [51]. However, for In-rich I-III-VI NCs the nonstoichiometric arrangement does not necessarily compromise

12

their properties. On the contrary, I-III-VI NCs were found to be better emitters than stoichiometric or Cu-rich/ Ag-rich I-III-VI compositions [52–54]. High photoluminescent (PL) quantum yields (QY) belonging solely to off-stoichiometry $AgIn_5S$, $CuIn_5S$, $Cu_3In_5Se_9$, and $Ag_3In_5Se_9$ have been reported [55–58]. As early as 2005, Zunger *et al* [59] were able to demonstrate that in the case of copper-poor conditions defect-pair formation between $2V_{Cu}$ vacancies and In_{++Cu} antisite defects eliminates deep trap levels. In addition, their very low formation enthalpy favors the formation of these defect pairs. The tendency of $CuInSe_2$ to form Cu vacancies, on the other hand, is also at the origin of its efficient self-doping. In a more general sense, both p- or n-type doping can possibly be obtained depending on the stoichiometry, which has been used for the realization of $CuInS_2$ or $CuInSe_2$ homojunction solar cells [59–61].

2.3.1   Synthesis of Ternary I-III-VI nanocrystals

The Pearson acid-base concept, widely known as the hard-soft acid-base (HSAB) theory was introduced by Ralph Pearson in the 1960s to rationalize a variety of chemical information by giving a qualitative description of reactions in inorganic and coordination chemistry. In the HSAB concept, reactants accepting electrons are classified as acids and reactants donating electrons as bases. The qualitative definition of HSAB was converted to a quantitative one by using the idea of polarizability. A less polarizable atom or ion is "hard", and a more easily polarized atom or ion is "soft." According to the HSAB theory, hard-hard and soft-soft acid-base configurations form more stable compounds than the ones of mixed hard-soft nature [62, 63]. The HSAB concept can be extended to the synthesis of colloidal NCs where, in this context, metal centers are defined as acids, anions and coordination ligands as bases [64]. The HSAB may be used as a guide for precursor and ligand selection when designing colloidal synthesis. As can be expected from the definition of the HSAB

13
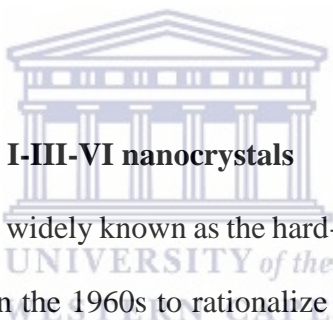
theory, metal salts of hard-soft nature experience accelerated decomposition at low temperatures compared to hard-hard or soft-soft precursors. The reaction kinetics of precursors undergo modification to different extents in the presence of coordination ligands, where either soft-soft and hard-hard complexes (relatively slower decomposition) or hard-soft and soft-hard compounds which decompose relatively faster The HSAB concept guidelines benefit the overall understanding of the synthesis of ternary I–III–VI NCs. During synthesis, the reaction flask contains M^+ (Cu^+ or Ag^+) which is a soft acid and M^{3+} (In^{3+}, Ga^{3+}, etc.) which is hard acid; hence there is an inherent difference in the reactivity of two identical metal precursors (e.g. AgCl and InCl$_3$). In addition, chalcogen anions are soft bases according to the HSAB and their softness is directly proportional to their atomic radius (S^{2-} $< Se^{2-} < Te^{2-}$). This fact makes the synthesis of I–III–Se NCs is, therefore, more challenging than for I–III–S NCs, due to strong preferential bonding of Se and Cu (or Ag) precursors. The synthesis of colloidal I–III–VI tellurides represents the worst-case scenario [65].

The strategy that was developed by Xie *et al* [66] forms the basis for most CuInS$_2$ NCs syntheses. This approach involves an injection of elemental sulfur into a reaction mixture which contains Cu^+ and In^{3+} salts, dodecanethiol, oleic acid, and octadecene at 180 °C. Long-chain thiols play a critical role in the synthesis. Dodecanethiol, which is a soft base preferentially complexes the Cu^+ ion, which is soft acid. In order to balance the reactivity between the Cu^+ and the In^{3+}, an excess of dodecanethiol must be added to the reaction flask. The use of soft-acid/soft-base CuI precursor, alternative S precursor (i.e., S-oleylamine solution), changes in injection temperature, and other reaction parameters represent some of the follow-up moderations of the alkanethiol-mediated synthesis [67–69]. There are also several heating-up approaches of CuInS$_2$ NCs synthesis where dodecanethiol has been used, and this because of its high decomposition temperature ($\geq$200 °C) which makes it suitable

to serve as a sulfur precursor. Prolonged heating times are however required for such heating up approaches due to slow decomposition kinetics [70–73].

Approaches for CuInSe₂ and AgInSe₂ NCs syntheses are significantly less developed compared to I–III–S NCs [73]. The M^+/M^{3+} reactivity challenge is the reason methods for I–III–S NCs show limited applicability when it comes to I–III–Se NCs syntheses. For example, slow decomposition of long-chain thiols at high temperature leads to anion-mixed quaternary I–III-(S; Se)₂ NCs [74, 75] and metal–Selenium bonded precursors are more difficult to synthesize than metal–sulfur precursors [76, 77]. Stoichiometric preparation of CuInSe₂ and AgInSe₂ NCs is achieved by using alkylamine- or phosphine-based reaction mixtures. In general, elemental Se is dissolved in oleylamine or trioctylphosphine (TOP) and heated with (or hot-injected to) the solution of metal salts. The temperature of the reaction is kept relatively high, while growth times are prolonged, and this approach counts on the completeness of the reaction. Relatively big sizes of I–III–Se₂ NCs are obtained via this strategy (typically >8–10 nm) [78–80].

Small-size CuInSe₂ and AgInSe₂ NCs can be obtained by accelerating reaction kinetics. Reaction promoting agents (e.g., diphenylphosphine [81] lithium silylamide [82–84]) are introduced into the reaction in order to achieve this or by using highly reactive selenium source (e.g., trimethylsilyl selenide [85, 86]) as an alternative. For example, utilizing diphenylphosphine allows one to tune the size of CuInSe₂ NCs from ∼1 to 9.2 nm, while their stoichiometries remain constant (∼0.92–0.97 Cu:In atomic ratio) [81]. The idea of this approach is derived from the synthesis of PbSe NCs, where it was demonstrated that adding secondary phosphines induces the reaction mechanism to proceed via reduction of cationic precursor to metal centers and rapid homolytic cleavage of trioctylphosphine-selenide

(TOPSe) precursor. This then eventually increases the reaction kinetics and this coupled with an increase in chemical yield [87]. In general, advancing the reaction kinetics of NC provides an eminent strategy to mitigate the difference in reactivity of the two metals (M^+ and M^{3+}) [81–86].

2.3.2   Synthetic Strategies

Several methods of synthesis of ternary I-III-VI QDs have been reported. Choosing a suitable synthetic route largely depends on the desired use of the QDs and the selection of solvents to be used. Synthesis of ternary I-III-VI QDs is reported circuitous due to the reactivity of the most commonly used cations (Cu^{2+}, In^{3+}, and Zn^{2+}) [88]. Furthermore, due to the multifaceted equilibria that occur between the cation and anion precursor reactivities, the synthesis also faces some limitations because of shape, composition and size control [89]. Tuning of reaction parameters such as temperature, reaction time and precursor ratios, however, allows for the achievement of monodispersed size controlled QDs.

2.3.2.1 Organic Synthesis

The fundamental principle of organic synthesis involves the high boiling temperature (typically between 220 and 300 ^{o}C) decomposition of organometallic precursors in hydrophobic solvents and coordinating agents in an inert atmosphere. High-quality colloidal nanoparticles are produced via organic synthesis through the use of hydrophobic reducing agents and/ or ligands such as octadecene (ODE), 1-dodecanethiol (DDT), octylamine (OctAm), oleylamine (OlAm), tri-octylphosphine oxide (TOPO) [89]. These ligands render QDs hydrophobic by effectively passivating their surface. Different methods have been established for the synthesis of ternary I-III-VI QDs in organic solvents, and these include

the hot-injection method, solvothermal, thermolysis, and the heating up method. Each of these methods is briefly described in the following section.

2.3.2.2 Hot Injection

In the hot-injection method, reagents are injected into a hot solvent. In the synthesis of QDs, a solution of the anionic precursor is injected into a hot solution of cationic precursor at elevated temperatures; this is followed by rapid nucleation. This approach allows for particle size distribution control [90]. In 2013, Vahidshad *et al*., [91] prepared CIS nanocrystal using CuCl, InCl$_3$, and thiourea as precursors. They varied the injection temperature between 150 and 270 ^{o}C in order to tune the size of the nanocrystals. Their results demonstrated that rapid nucleation followed by retarded particle growth occurred at elevated temperatures compared to lower temperatures. The most effective temperature for injection was 240 ^{o}C. They were able to prepare the material with narrow size distribution and particle diameter between 10 and 30 nm by effectively tuning and controlling the temperature of the solution, rate of injection and coordinating solvent to capping agent ratios. The emphasis of the study was the significance of injection temperature with reference to the injection method. According to Yuan *et al* [92], using the injection method for large volumes is advised against as this can slow down the injection process; thus causing an overlap between nucleation and growth which often leads to undesired broad particle sizes.

2.3.2.3 Solvothermal

Solvothermal method is one of the most prevalent and advantageous synthetic routes to fabricate the nanomaterials with different morphologies. It involves placing the reactants

into an autoclave filled with water or organic compound to carry out the reaction under high temperature and pressure conditions [93]. The solvothermal method is an advantageous method for the production of I–III–VI type QDs at gram scale due to its simplistic and large-scale up properties. The first synthesis of highly fluorescent CIS/ZnS core/shell QDs capped with DDT prepared via solvothermal method was reported by Nam *et al.*, 2011 [92]. The core was prepared using $(In(Ac)_3)$, Cu(I) iodide (CuI) and DDT in a noncoordinating solvent ODE at 180 $^{\circ}$C for 5-6 h. The shell was grown over the core from zinc acetate with potassium ethyl xanthogenate at 200 $^{\circ}$C for 12 h. Yellow-to-red CIS/ZnS QDs with a quantum yield (QY) pf 65% were produced. Jia *et al.*, 2016 [94] used solvothermal method to prepare CIS QDs by heating up a mixture of precursors i.e. zinc stearate $(ZnSt_2)$, cuprous acetate $(Cu(OAc)_2)$, indium acetate $(In(OAc)_3)$ and oleylamine (OAm) in the presence of DDT/ODE. The excitation wavelength was varied in order to tune the PL intensity and peak position of the CIS and CIS/ZnS QDs. The emphasis of this work was the effect of excitation wavelength on the optical properties of CIS QDs. The increase of the excitation wavelength from 550 nm to 630 nm resulted in the PL peak position shifting from 665 to 685 nm. This shift in the PL peak position was attributed to the internal defect state of the material.

2.3.2.4 Thermolysis

Thermolysis is an extremely rapid method that involves the preparation of nanoparticles by heating the capping agent together with metal complex precursors at elevated temperatures using localized heat. Choi *et al.*, 2006 [95] prepared CIS heterostructured nanoparticles via thermolysis of a mixture of Cu-oleate and In-oleate complexes in dodecanethiol. Their study showed that the shape of the prepared CIS nanocrystals could be varied by changing reaction temperature and time to obtain either corn, bottle or larva shapes. Lee *et al.*, 2014 [95] were the first to describe the use of a hybrid flow reactor to prepared CIS/ZnS using thermolysis.

They grew the core of their QDs (CIS) at 210 ^{o}C for 1 minute using DDT/ODE. The core was passivated by growing the ZnS shell at 320 ^{o}C for 2 minutes. PL quantum yields increased from 20% to 60% after ZnS shell growth. The extremely short synthetic time provided by the thermolysis method is advantageous for nanoparticle preparation. The presence of multiple peaks (even at shorter wavelengths) in the PL spectra is a major drawback for this method.

2.3.2.5 Heating Up Method

In the heat-up based method (non-injection), all reagents are carefully mixed into a single reaction flask/vessel and rapidly heated in a controlled manner to induce nucleation and growth of nanocrystals. It is highly suitable for large scale synthesis compared to other methods [96] and also mitigate some of the challenges faced by the injection method, such as control of reagent mixing time, injection time and reproducibility. Using diesel as reaction solvent and at fast heating rate of 150-200 ^{o}C min^{-1}, Thuy *et al*., 2014 [97] were able to synthesize CIS/ZnS core/shell QDs by heating up copper (I) iodide (CuI), DDT, In(Ac)$_3$, zinc stearate and oleic acid as precursors. They obtained high-quality CuInS$_2$ QDs Core at a reaction temperature of 210 ^{o}C and 15 min reaction time using 1:1 Cu:In molar ratio. Regulacio *et al*., 2013 [98] were able to successfully prepared elongated CGS nanocrystals using a facile injection-free synthetic strategy that involves the thermal decomposition of metal dithiocarbamate complexes in the presence of dodecanethiol.

2.4 Several factors affecting the synthesis and properties of semiconductor nanocrystals

The quality of semiconductor nanocrystals has an influence on their properties. Attempts to control the synthesized nanocrystals are through many parameters which play crucial roles in their overall properties. Therefore, QDs can be tailored according to their specific application by precise control of the major parameters affecting their synthesis which include capping agent, precursor ratio, reaction time, temperature, and solvent type. All these parameters are explored below. Different applications require QDs that are defect-free, well dispersed and homogeneous. Optimizing each of the parameters to obtain ideal crystals is, however, more complex and practically [99], [100].

2.4.1 The effect of precursor ratio

The shape and size range of QDs is related to the stoichiometry of the constituents. The PL peak position and intensity of the CIS QDs can be optimized by changing the Cu:In ratio and this was demonstrated by Jiang *et al*., 2017 [101] studied the effects ratio change on optical properties by preparing CIS/ZnS QDs using different Cu: In ratio from 1:2 to 1: 48. They showed that a decrease in the Cu:In ratio causes a shift to shorter wavelengths, which indicates an increase in the bandgap under indium rich conditions. In 2016, Zheng et al., [102] synthesized CIS/ZnS QDs at gram scale and obtained a 20% photoluminescence quantum yield (PLQY). After examining different Cu:In ratios, they found Cu-poor CIS QDs produced higher PLQY. NIR CIS QDs were successfully synthesized by Kim *et al*., 2017 [103] and were able to tune the Cu:In ratio from 0.25:1 to 2:1 which caused a shift in the PL peak position from 680 to 850 nm. The donor-acceptor pair, where In_{Cu} (In substituted at the

Cu site) and/or V_S (S vacancy) probably act as donor states with V_{Cu} (Cu vacancy) as an acceptor state is responsible for the red-NIR emission observed in this case [101, 104, 105].

2.4.2   The effect of time and temperature

Growth and nucleation of particles from their precursors heated in a solution containing a coordinating solvent are the main stages involved in the preparation of nanoparticles. Time and temperature effects are studied in order to monitor this [106–113]. To effectively optimize the time and temperature for a given synthesis of nanoparticles, the Ostwald ripening effect is the main attribute that needs to be overcome. The Ostwald ripening effect permits the grouping of particles together, with the smaller ones tending to stick to onto big ones leading to the formation of larger materials [114]. In their report, Govindraju *et al*., 2014 [115] varied the time from 2 minutes to 60 minutes during the synthesis of copper selenide and observed the growth of particles as the time increased. The particles became more monodispersed and crystallized into a centered cubic phase of Cu_2Se. Tang *et al* [116] used the hot-injection method to prepare to synthesize of copper indium gallium selenide nanoparticles, and the nanoparticles were formed as a result of a rapid injection of precursors in oleylamine at high temperatures. They found that higher injection temperatures (such as 270^oC), however, favored the growth of larger particles. Kim *et al* [117] prepared NIR DDT capped CIS/ZnS QDs in noncoordinating solved ODE by varying the temperature from 180 to 250 ^oC to control Zn ion diffusion during ZnS shell growth. They found that at lower temperatures, the diffusion rates were low compared to elevated temperatures due to the effect of temperature on the activation energy for diffusion. There are a few studies have been reported on the direct aqueous synthesis of CIS and CIS/ZnS QDs where low

temperatures (90–95 ∘C) have been used [118–120]. It has also been reported that the CIS crystal structure can be varied by changing the reaction temperatures [121].

2.4.3   The effect of solvent

Different solvents can be used for the synthesis of ternary QDs. However, different reaction pathways and additives can be employed to optimize the overall synthesis to obtain nanoparticles with exceptional properties [122–124]. While a number of solvents can be used for the preparation of metal selenide nanoparticles; fatty acids, polyols, long-chain phosphines, and long-chain amines solvents are considered more suitable for growth control and stability of QDs [125–127]. Klimov *et al*., 2011[128] reported an efficient synthesis of CuInS$_2$ QDs with strong photoluminescence in the NIR. They were able to obtain yields of excess 90% coupled with minimal solvent waste. Shell growth of either ZnS or CdS on the core CIS resulted in a remarkable increase in PL quantum yield—up to 10-fold for ZnS and a little higher for CdS. In general, CIS QDs with single-monolayer shell exhibit PL QYs of >60%, while in their recorded value is 86%. Several others employing a similar strategy obtained dramatically improved PL quantum yields [129–134]. Das *et al*., 2008 [135] employed thiourea as a sulfur precursor in the synthesis of CuInS$_2$ nanocrystals. They used alcohols used as solvents and obtained big particles of more than 100 nm. On the other hand, when a corresponding selenide (selenourea) source was used, employing oleylamine as solvent and as well as a capping agent, nanocrystals of <20 nm were obtained [136], [137]. Pan *et al*., [138] demonstrated the importance of the capping ligands ratio (OA, DDT, OLA) for the control of the crystal structure and were the first to report the synthesis of wurtzite CuInS$_2$ nanocrystals.

2.5   Dendrimers

Dendrimers are a highly branched and unique class of macromolecules with three-dimensional architectural design [139]. Dendrimers are characterized by three components: a central core, branches and the periphery. They are nearly spherical in shape (nanostructure ranging from 10 to 200 Angstroms in diameter) and their extremely regular structure is the reason for this. Dendrimers are built upon an initiator core, with several branching interior layers composed of repeating units and multiple active primary amine groups at its surface. The functional groups that characterize the surface of the dendrimer can be used as a backbone for the attachment of a number of biological materials or any type of material depending on the specific application [140]. Dendrimers are produced in an iterative sequence of reaction steps, in which additional iteration leads to a higher generation material. One of the best examples of controlled hierarchical synthesis is the creation of dendrimers using specifically designed chemical reactions; this specificity allows the 'bottom-up' creation of systems that are otherwise complex. A new 'generation' with a double number of active sites (end groups) and an approximately double molecular weight of the previous generation is created by each layer. The appealing aspect to technology that dendrimers have is that it is relatively easy to precisely control their size, composition and chemical reactivity [141, 142].

Dendrimers were first discovered by Fritz Vogtle in 1978, by Donald Tomalia and co-workers in the early 1980s, and at the same time, but independently by George R. Newkome [143]. Fritz Vogtle imagined the core of the dendrimer as a potential host for guest molecules. It wasn't until 1985, however, that dendrimers were at the frontline of chemistry and were exhibited as possible incarceration devices for molecules. During this time period,

Newkome [144] and Tomalia [145] simultaneously reported work demonstrating the synthesis of dendrimer molecules. A variety of dendrimers have been developed since that time; different molecules have been employed to functionalize to the periphery of the dendrimer. Dendrimers have found themselves as excellent carrier molecules for use in nanoscale medical applications due to their unique architecture and functionality. They have been explored as light-harvesting agents [146], chemical sensors [147], catalysts [148] and cross-linking agents [149]. Many of the intriguing properties of dendrimers, as well as their syntheses and possible applications, are discussed [150–153]. There are many types of dendrimers; the first dendritic structures that were thoroughly investigated and have received widespread attention are Tomalia's PAMAM dendrimers [145].

2.5.1   Poly (propylene imine) Dendrimers

Poly(propylene imine) (PPI) dendrimers are highly branched macromolecules terminated with amino groups with a number of interesting preparties. Poly(propylene imine) dendrimers have also been called Astramol dendrimers, or have simply been abbreviated as PPI-dendrimers, or DAB-Am-x dendrimers. DAB stands for the diaminobutane core and x=4, 8, or 16 for the number of primary amine end groups associated with the generations 1, 2, or 3, respectively [154], [155]. These dendrimers are generally poly-alkyl amines having primary amines as end groups, the dendrimer interior consists of numerous tertiary tris-propylene amines and their commercial availability extends to G5 [156]. Vögtle *et al.* reported the first cascade structure of oligo (propylene imine) synthesized based on a repetitive reaction sequence of double Michael additions of an amine to acrylonitrile, followed by the reduction of the nitriles to primary amines [144, 157, 158]. Poly (propylene imine) dendrimers have various interesting characteristics which makes

24

them suitable building blocks to acquire well-defined amphiphilic structures such as the combination of hydrophilicity, highly branched structure and chemical functionality [159, 160].

2.5.2   Dendrimers as Coordinating Agents

Many capping agents with variable sizes including large polymers such as chitosan, large macrocycles such as a-cyclodextrin and smaller molecules such as tert-butyl functional groups have been studied. However, comparing the efficiency of various capping agents is very difficult due to complexity of capped systems [161]. Dendrimers are becoming more popular as nanomaterial stabilisers or capping agents. One of the reasons for this is because in general, they have high loading capacity due to their nanocavities. In dendrimers, the nanoparticles can be formed either in the interior cavities of the dendrimer (dendrimer encapsulated nanoparticles) or in the periphery of the dendrimers (dendrimer stabilized nanoparticles) [162]. Malinga *et al* [162] successfully synthesized generation 2 and 3 poly(propylene imine) dendrimer capped NiFe nanoalloy. The HRTEM micrograph for the nanoalloy showed an average size range of 1 to 4 nm and the presence of Ni and Fe as the alloy was confirmed by energy dispersive spectroscopy. Polyamidoamine dendrimers capped-carbon dots (PAMAM-CDs) were fabricated using a one-step microwave approach by Gao *et al* [163] and were applied in immunosensing, where the proposed immunosensor demonstrated a wide linear detection range from $100\,\text{fg}\,\text{mL}^{-1}$ to $100\,\text{ng}\,\text{mL}^{-1}$ with a detection limit of $0.025\,\text{pg}\,\text{mL}^{-1}$. Gayen *et al* [164] used colloidal synthesis to prepare hybrid cadmium sulfide–dendrimer nanocomposite and investigated their spectroscopic properties. The nanoparticles fluoresced from 375 to 650nm650nm under near-ultraviolet excitation, and their absorption spectra exhibited a strong blueshift of the band edge

compared to that of the bulk CdS. They discovered that the stability of nanocomposites depended significantly on the dendrimer generation, while the size and spectroscopic properties exhibited a weaker dependence. Wisher *et al* [165] prepared thiolated PAMAM dendrimer-coated CdSe/ZnSe nanoparticles and used them as protein transfection agents. Their study showed that partial thiolation of PAMAM dendrimers makes them good ligands for CdSe/ZnSe nanoparticles. The dendrimer-protected nanoparticles were soluble in water and demostrated good stability and were able to effectively transport other molecules across the cell wall and hence are promising fluorescent transfecting agents.

2.6   Ternary Solar Cells

Application of nanoparticles as either a sensitizer or electron donating component in the structure of organic photovoltaic devices' (OPVs') photoactive layer has led to the development of a new class of ternary systems called hybrid solar cells. Among several nanoparticles, ternary QDs such as $CuInSe_2$ are at the centre of attention due to the promising applicability they have shown in many optoelectronic devices, particularly solar cells, due to their high absorption coefficient, tunable band gap, multiple exciton generation with single photon absorption, tunable energy levels, slow exciton relaxation and low cost [166–170]. The need to extend the absorption spectra of the large bandgap polymers to cover the full range of the sun's irradiation spectrum was the main drive for the development of ternary solar cells. Unlike tandem solar cells, in ternary systems the sensitizer is merely incorporated into the host active layer which simplifies the device fabrication as a single junction solar cell. For this reason, fabrication of ternary solar cells becomes possible with lower costs, which is an important issue for industrial applications.

In general, the most widely used sensitizers in ternary blend systems are the donor (D) components, forming donor:donor:accepter (D:D:A) ternary systems. However, the acceptor components may be also introduced as sensitizer forming D:A:A ternary systems as shown in Figure 2.1. Various sensitizers based on low band gap polymers, small molecules, dyes and nanoparticles are employed in the structure of the photoactive layer in combination with donor material which is usually consists of a large bandgap polymer and fullerene derivative as acceptor. In an ideal photoactive layer the sensitizer not only broadens the absorption width but can also facilitate the exciton dissociation and provide excellent charge transporting properties [171, 172].
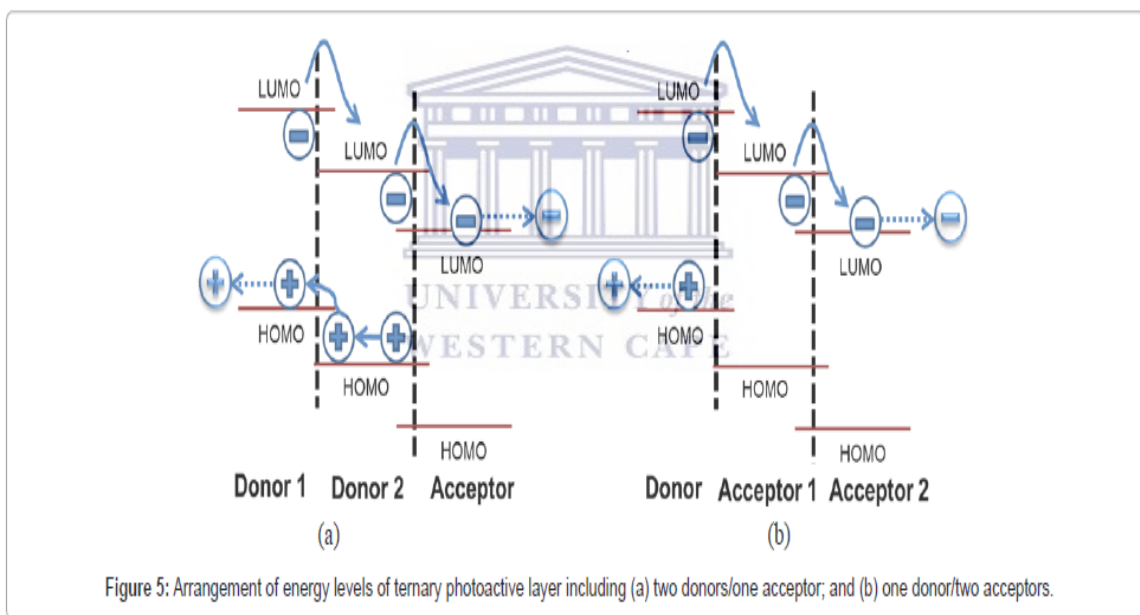

Figure 5: Arrangement of energy levels of ternary photoactive layer including (a) two donors/one acceptor; and (b) one donor/two acceptors.

Figure 2.1: Arrangement of energy levels of ternary photoactive layer including (a) two donors/one acceptor; and (b) one donor/two acceptors [173].

CHAPTER 3:

FUNCTIONALIZATION OF G1 POLY (PROPYLENE THIOPHENEIMINE) DENDRIMER

3.1   Introduction

Dendrimers are a class of three-dimensional synthetic monodisperse macromolecules with well-defined and hyperbranched and globular shaped architecture. The term dendrimer comes from the two Greek words "dendron;" which means a tree and "meros," which means a part; it refers to its characteristic appearance [174, 175]. They are characterized by three distinct regions: the core, branches, and periphery (surface). The core is bonded covalently to layers of repeating units called generations and several terminal groups [176–178]. The structure of these macromolecules tends to become denser and more compact as the branches emanate from the central core. Their chemical and physical properties are affected by parameters such as the shape and multiplicity of the core, the size, and shape of end groups and their chemical composition. In addition, the interdependency of generations creates a unique molecular shape and leads to essential properties such as high solubility and low viscosity [176, 179]. Due to the well-defined structures that allow chemists to precisely tailor them with different property-responsive groups, interest in these macromolecules continues to increase despite their large sizes and complexities that come with functionalizing their periphery. For example, unsymmetrical-type dendrimers (like those pioneered by the groups of Fréchet and Newkome) provide motifs for core functionalization, while the symmetric types such as the commercially available poly(amidoamine) (PAMAM),

28

cyclotriphosphazene (PMMH), and poly- (propylene imine) (PPI) dendrimers are generally the most widely used in studies of periphery modification [180, 181].

Poly (propylene imine) dendrimers are generally poly-alkyl amines having primary amines as the periphery, the dendrimer interior is made up of many tertiary tris-propylene amines [182]. They have also been called Astramol dendrimers, or have simply been abbreviated as PPI-dendrimers, or DAB-Am-x dendrimers. DAB stands for the diaminobutane core and x for the number of primary amine end groups associated with each generation [183]. Vögtle *et al.* reported the first cascade structure of oligo (propylene imine) synthesized based on a repetitive reaction sequence of double Michael additions of an amine to acrylonitrile, followed by the reduction of the nitriles to primary amines [184–186]. Poly (propylene imine) dendrimers have various interesting characteristics which makes them suitable building blocks to acquire well-defined amphiphilic structures such as the combination of hydrophilicity, highly branched structure and chemical functionality [187, 188].
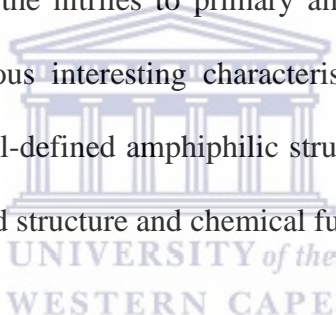
The properties of dendrimers are mainly attributed to the peripheral functional groups [189]. The unique combination of dendritic properties, i.e. multifunctional nature and high density of peripheral groups, tunability to design any type of dendrimer and ability to encapsulate small molecules, have established them as an ideal choice of capping agent to create multifunctional nonaparticles (MNPs). In this regard, various types of dendrimer-encapsulated (DE) and dendrimer-coated (DC) metal nanoparticles have been created by utilizing a variety of chemical processes. The DE-MNPs, where the MNPs (size range of 1 – 2 nm) are entrapped within the dendritic cavity, has been found highly useful for catalytic and imaging applications, and have been discussed in many excellent reviews [190–194]. Whereas on the other hand, the DC-MNPs, where the MNPs are relatively larger in size (>5

nm) compared to the size of single dendrimer molecule (i.e. 2 – 5nm for G2 to G6), the outer surface of MNPs is protected by many dendrimer molecules, generating high density of surface functional groups. These DC-MNPs exhibit physicochemical properties, such as stability, hydrophilicity, conjugation ability, like the DE-MNPs, but the unique combination of LSPR properties & high absorption coefficient of MNPs and high ligand carrying capacity of dendrimers makes them more useful for biomedical and other technological applications [190–192].

The use of dendrimers as capping agents and host molecules is not only limited to metal nanoparticles but also extends to semiconductor nanocrystals. For example, CdS-QDs and/or ZnS-QDs have been synthesized using dendrimer structure, where polyamide dendrimer (PAMAM) is employed as host confinement (Jin et al., 2008; Sooklal et al., 1998; Wisher et al., 2006; Ling & Cong, 2008) [195–198]. Hybrid CdS DAB dendrimer nanocomposite have been synthesized and characterized in methanol (Lemon & Crooks, 2000; Gayen et al., 2007) [199, 200]. These nanocomposites are formed by the arrested precipitation of nanometer-scale CdS clusters in the presence of polyamide dendrimers. Jie et al also reported a novel dendrimer/CdSe–ZnS–quantum dot nanocluster (NC) was fabricated and used as an electrochemiluminescence (ECL) probe for versatile assays of cancer cells for the first time [201]. Polyamidoamine dendrimers capped-carbon dots (PAMAM-CDs) were fabricated using a one-step microwave approach by Gao et al and were applied in immunosensing, where the proposed immunosensor demonstrated a wide linear detection range from 100 fg mL^{-1} to 100 ng mL^{-1} with a detection limit of 0.025 pg mL^{-1} [202].

In this present study, generation 1 poly-(propylene imine) (PPI) dendrimer has been fuctionalized with thiophene and characterized using proton nuclear magnetic resonance

30

spectroscopy (^{1}H-NMR), Fourier transform infrared spectroscopy (FT_IR), ultraviolet-visible (UV-Vis) spectroscopy, powder x-ray diffraction (XRD) and cyclic voltammetry. The end goal was to use the as prepared G1- poly (propylene thiopheneimine) dendrimer (G1PPT) as a capping agent for $CuInSe_2$ QDs.

## 3.2   Experimental Protocols

3.2.1   Chemicals and Materials

All manipulations were carried out using standard Schlenk line technique under N_2. 2-Thiophenecarboxaldehyde (98%; Sigma Aldrich), DAB-Am-4, Polypropylenimine tetramine dendrimer, generation 1 (Sigma Aldrich) and Methanol anhydrous (99.8%; Sigma Aldrich).
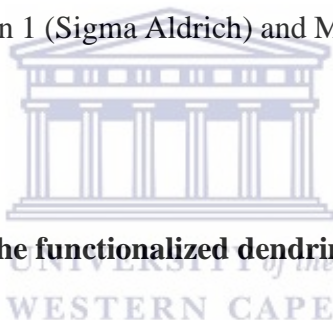
3.2.2   The preparation of the functionalized dendrimer

Prior to the functionalization of the dendrimer, a 100 mL 3-neck round bottom flask was washed, rinsed then dried for two (2) hours to remove all moisture. Then the glassware was cleaned with nitrogen (N2) gas. Synthesis of the G1 poly (propylene thiopheneimine) (G1PPT) dendrimer was carried out by condensation reaction of PPI with 2-thiophene carboxaldehyde, A reaction mixture of poly (propylene imine) generation one dendrimer (1.60 g or 5.1 mmol) and 2-thiophene carboxaldehyde (2.29 g or 20.40 mmol) in a 50 mL dry methanol was stirred magnetically under a positive pressure of nitrogen gas for 48 hours in a 100 mL three-necked round-bottom flask.
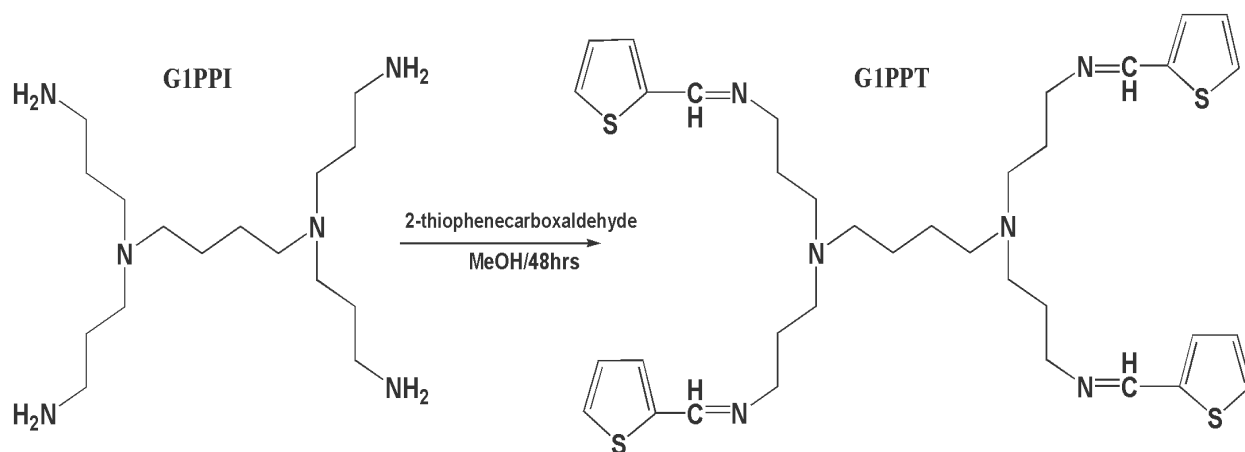
Scheme 3.1: Functionalisation of G1PPI

The methanol from the reaction mixture was removed with a rotatory evaporator and the residual oil was dissolved in 50 mL dichloromethane (DCM). The organic phase was then be washed with 50 mL of water 6 times to remove unreacted monomer. The DCM was removed by rotary evaporation to obtain the desired product as a yellow oil.
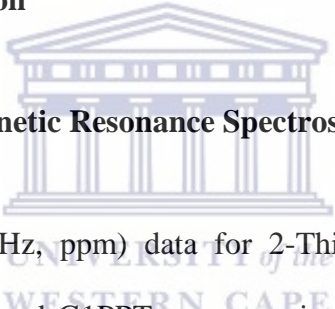
3.2.3 Instrumentation

All electrochemical measurements were done using BAS100W integrated automated electrochemical workstation from Bio Analytical Systems (BAS), Lafayette, USA, and Princeton Applied Research Potentiostat model 273A. All cyclic voltammograms were recorded with a computer interfaced with BAS 100W and Princeton 273A electrochemical workstation using a 10 mL electrochemical cell with three electrodes set up was used. The electrodes used in the study were (1) glassy carbon working electrode (A = 0.071 cm^2) from BAS, (2) platinum wire from Sigma Aldrich acted as counter electrode and (3) Ag/AgCl from BAS kept in (3 M NaCl) was the reference electrode and alumina micro polishing pads were obtained from Buehler, LL, USA and were used for polishing the gold electrode before modification. Ultraviolet-visible (UV-Vis) measurements were made using a Nicolet

Evolution 100 UV-Visible spectrometer (Thermo Electron, UK) where the samples were placed in quartz cuvettes before analyses. ^{1}H NMR spectra were recorded on a 200 MHz, Varian Gemini XR200 spectrometer, using CDCl3 as the solvent, and tetramethylsilane as internal standard. All FTIR spectra were recorded on spectrum 100 FTIR spectrometer (PerkinElmer, USA) in a region of 450 to 4000 cm^{-1}. X-ray Diffraction (XRD) measurements were taken with a D8 Advanced diffractometer from BRUKER AXS using an X-ray tube with copper K-alpha radiation operated at 40 kV and 40 mA and a position sensitive detector Vantec_1 which enables fast data acquisition. Measurements were taken in the 2 theta range of 10º- 80º with a step size of 0.028º.

3.3   Results and Discussion

3.3.1   Proton Nuclear Magnetic Resonance Spectroscopy

The ^{1}HNMR (CDCl$_3$ 400 MHz, ppm) data for 2-Thiophenecarboxaldehyde, G1 poly (propylene imine) dendrimer, and G1PPT were acquired for comparison and in order to monitor the changes after functionalization. The ^{1}HNMR data for 2-Thiophenecarboxaldehyde yielded the expected results with the H-1 proton given rise to a singlet at δg 9.779 ppm due to deshielding caused by the migration of the electron density during conjugation. The H-2 proton gave rise to doublet at δg 7.8 ppm, which is a slightly lower chemical shift than the H-1 proton because of the increased distance from the deshielding effect. The H-3 proton gave rise to a doublet of double at δg 7.79 ppm due to interaction with neighboring H-2 and H-4 protons. In contrast, the H-4 proton gave rise to a doublet at δg 7.23 ppm, which is at lower frequencies than the rest due to an even farther distance from the deshielding effect [203–205]. On the other hand, the NMR spectrum of G1PPT is shown in figure 3.1 below. The ^{1}HNMR (CDCl$_3$ 400 MHz, ppm) data for G1PPT

are 1.307 (s,br,4H, H-1), 1.740 (t,8H, H-2), 2.414 (m,br,12H, H-2&3), 3.517 (t,8H), 6.974(t,8H, H-8), 7.20 (s4H, H-7), 7.289 (s4H, H-6), 7.85 (C$_4$H$_3$S). A new ^{1}HNMR of chemical shift was observed at 8.31 ppm for G1PPT analysis. The new chemical shift was originally not present in the parent G1-PPI, which therefore indicates that the G1PPT was functionalized [206, 207].
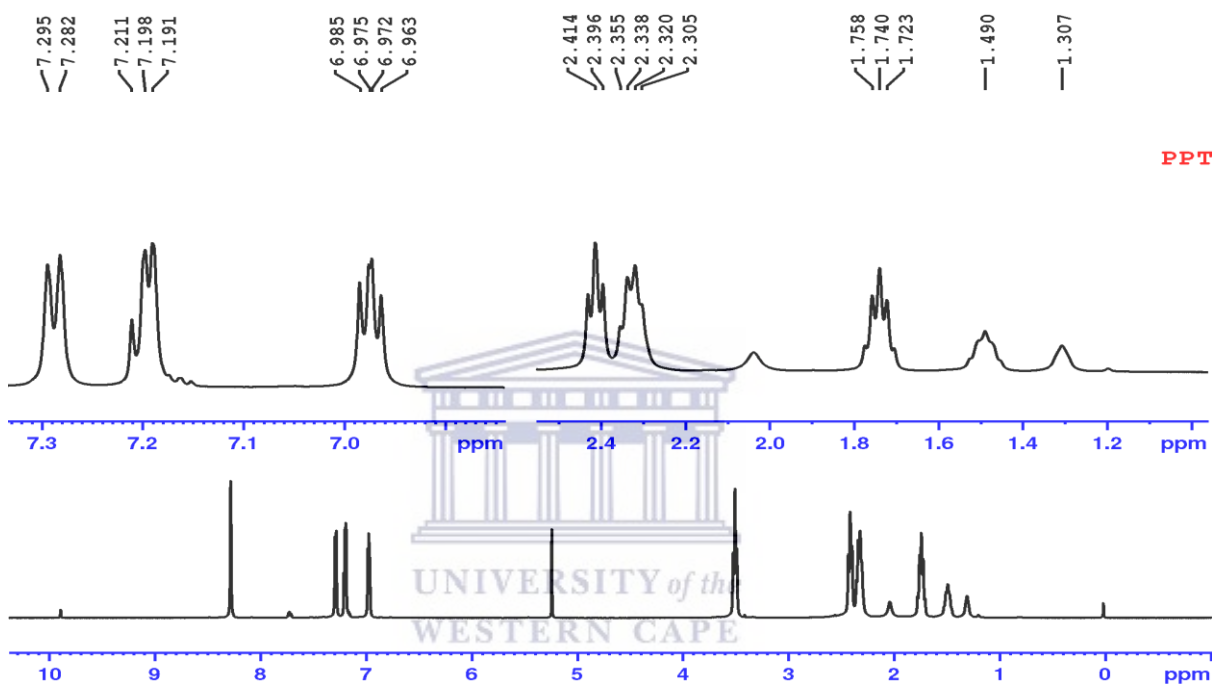

Figure 3.1: ^{1}H-NMR Spectrum of G1PPT

3.3.2   Fourier Transform Infrared spectroscopy of G1PPT (FT-IR)

FT-IR spectroscopy was performed on G1PPT to validate the functionalization of the dendrimer. The spectrum, which is shown in Figure 3.2 and the corresponding overlay in Figure 3.3 below, depicts several peaks which are characteristic to G1PPT at755, 929, 1039, 1221, 1428, 1527, 1673, 2339, 2841, 2945, 3022 cm^{-1}. In comparison to G1-PPI, the G1PPT exhibited an out-of-plane bending of C-H bond located at the α-position to the thiophene

34

ring was observed at 755 cm^{-1} [206]. The medium-weak multiple bands accounting for the C=C and C-C stretching in the 5- membered aromatic ring of thiophene can be observed at 1428 cm^{-1} and 1527 cm^{-1} respectively. The peak at 929 cm^{-1} was assigned for C-S bending deformation stretching of G1PPT [167]. The other peaks at 1039 cm^{-1} and 1221 cm^{-1} were due to deformation of C-H bending and CH in-plane of vibrations. The C=N bond stretching vibration present in the dendrimer moiety appeared as a sharp band at 1673 cm^{-1}. The bands at 2841, 2945, 3022 cm^{-1} in G1PPT indicate the presence of the CH_2 stretch in the dendrimer moiety [207].
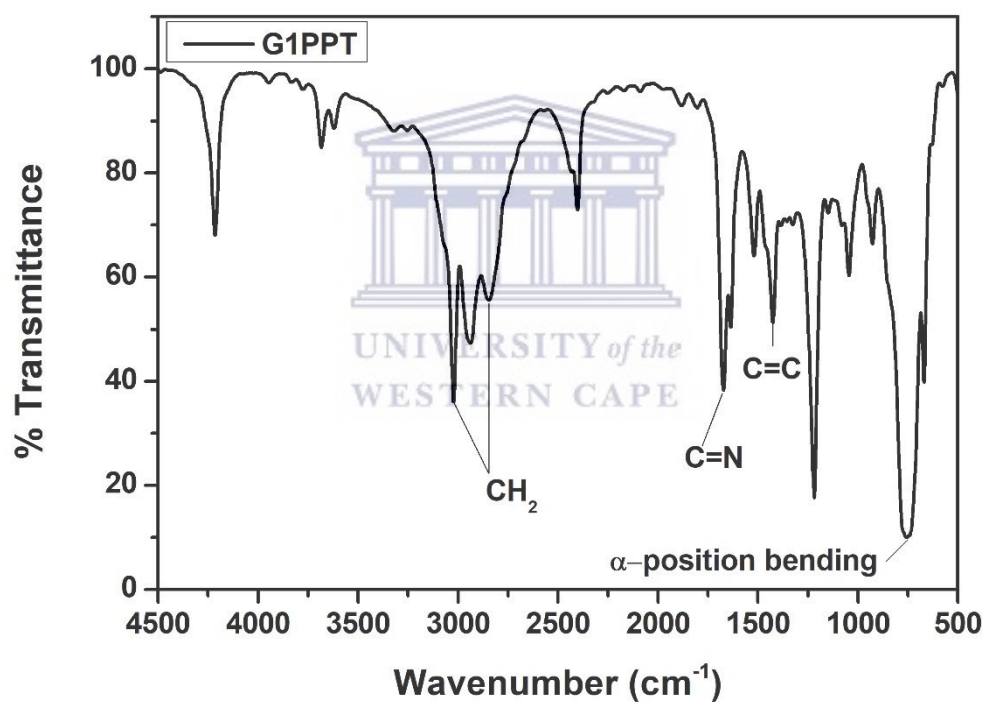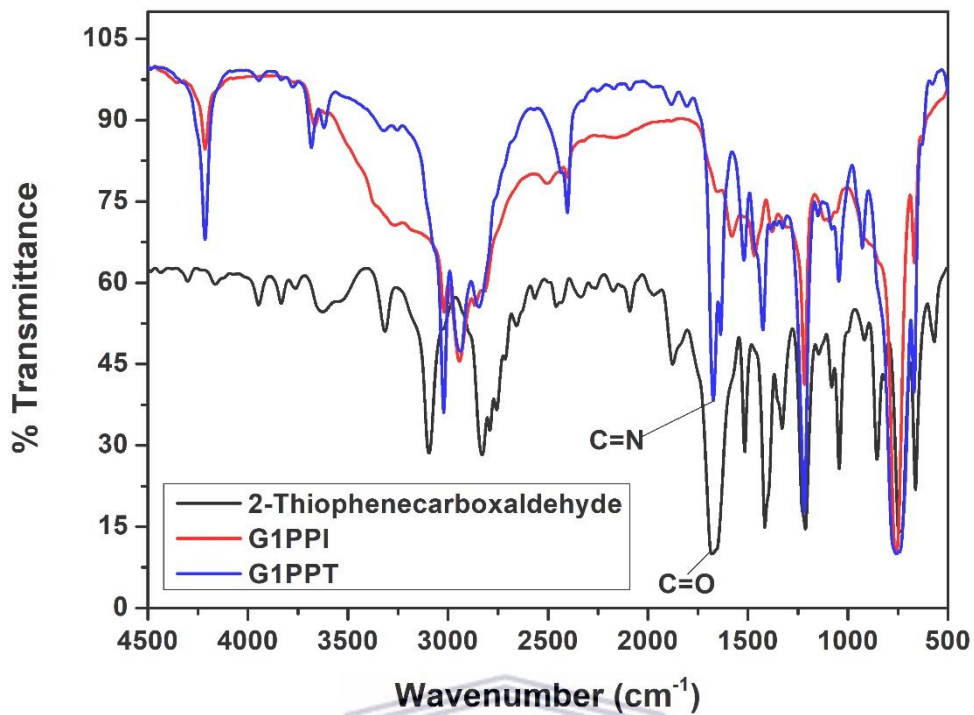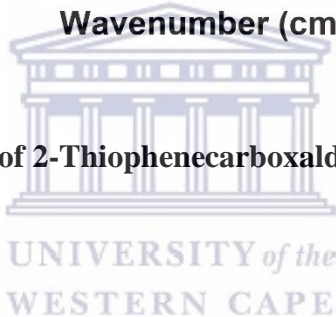

Figure 3.2: FT-IR Spectrum of G1PPT

Figure 3.3: FT-IR Spectrum of 2-Thiophenecarboxaldehyde, G1-PPI, and G1PPT

3.3.3 UV-Vis Spectroscopy of G1PPT

UV-vis spectroscopy was used to study the optical properties of G1PPT. A typical spectrum of G1PPT dissolved in chloroform obtained at room temperature is shown in Figure 3.4 and Figure 3.5 below. The spectrum characterizes the total transmittance loss due to the absorption and scattering of light when passing the G1PPT solution [208–210]. The spectrum of G1PPT shows two distinct absorption bands at 241 nm and 304 nm. These two bands are characteristics of the absorbance of the two chromophores C=N and C-S-C respectively, present in the functionalized dendrimer whose transitions are respectively π-π* and n-π* [211–213]. Figure 3.5 shows an overlay of G-PPI, 2-Thiophenecarboxaldehy and G1PPT. The absorption bands show a shift towards longer wavelengths after functionalization compared to the original G1-PPI. This onset shift is supported by the shift of the energy bandgap after functionalization. G1-PPI has a bandgap of 4.29 eV and the resulting G1PPT after functionalization has a bandgap of 3.1 eV.
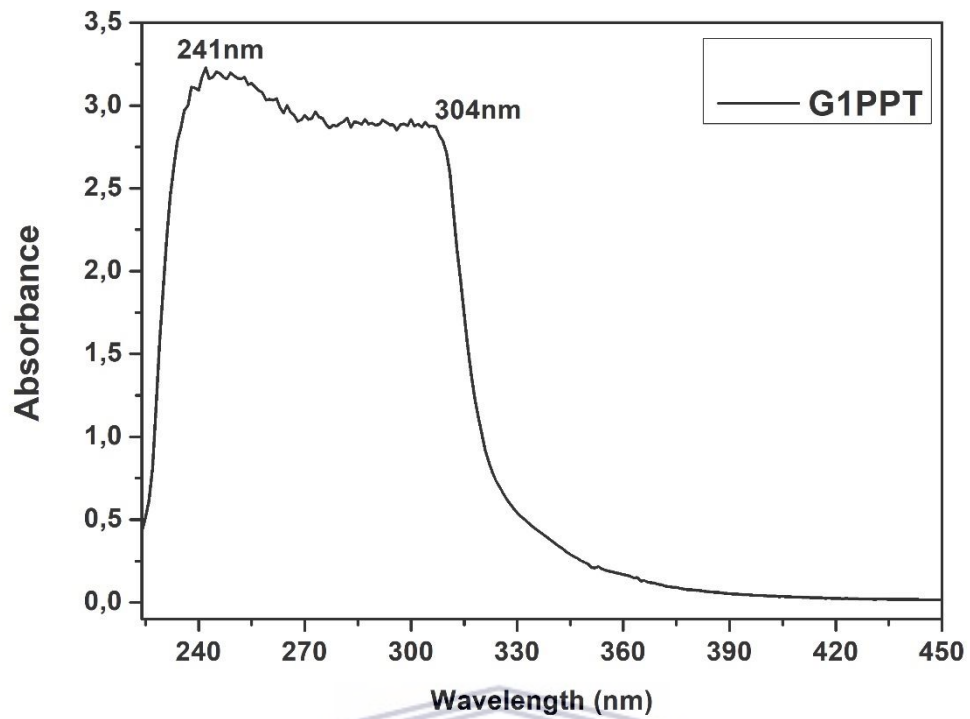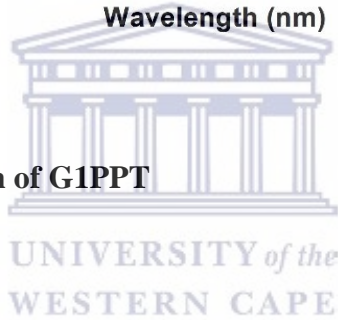
Figure 3.4: UV-Vis Spectrum of G1PPT
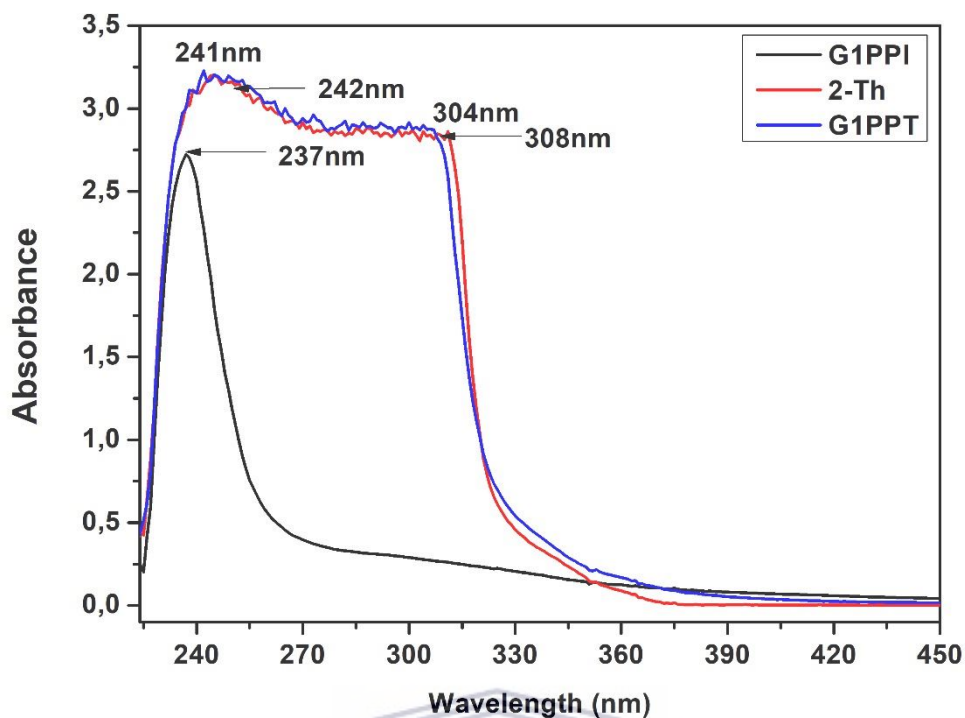
Figure 3.5: UV-Vis Spectrum of G1PPI (black line), 2-Thiophenecarboxaldehyde (black line), and G1PPT (blue line).
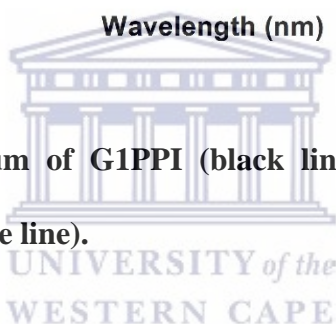
3.3.4   Powder X-ray Diffraction (XRD) of G1PPT

X-ray powder diffraction-a technique that has matured significantly in recent years-is used to identify solid samples and determine their composition by analyzing the so-called "fingerprints" they generate when X-rayed [214, 215]. Figure 3.7 below presents the powder x-ray diffraction of G1PPT. G1PPT has an amorphous morphology and therefore no measurable X-ray patterns or does not display any crystallinity.
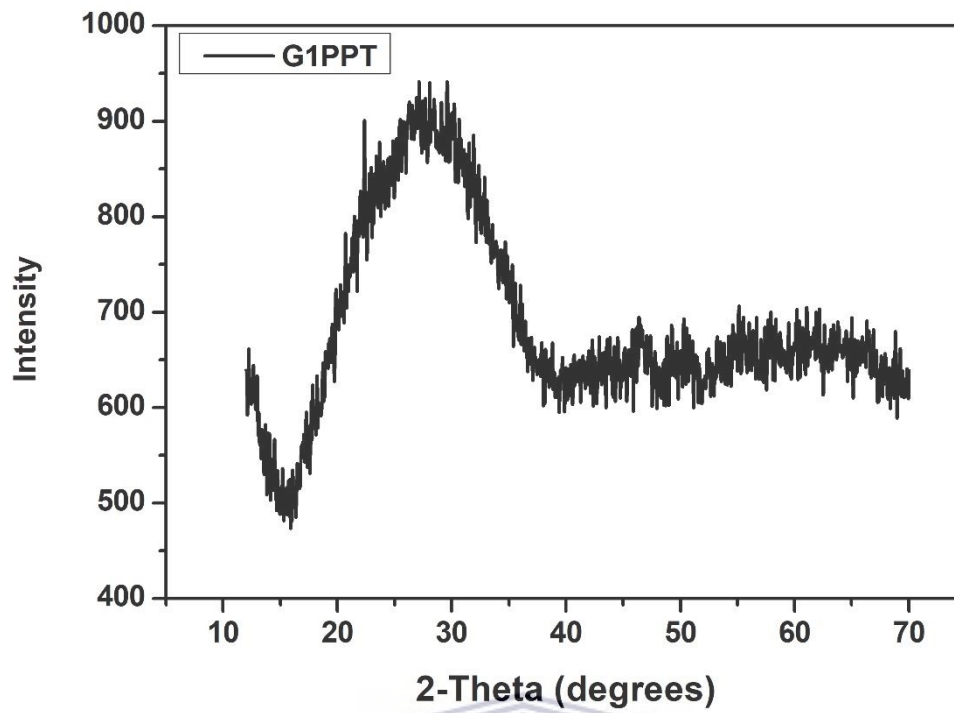
Figure 3.7: Powder X-ray diffraction of G1PPT

3.3.5   Electrochemical Studies of G1PPT

3.3.5.1 Cyclic Voltammetry of G1PPT
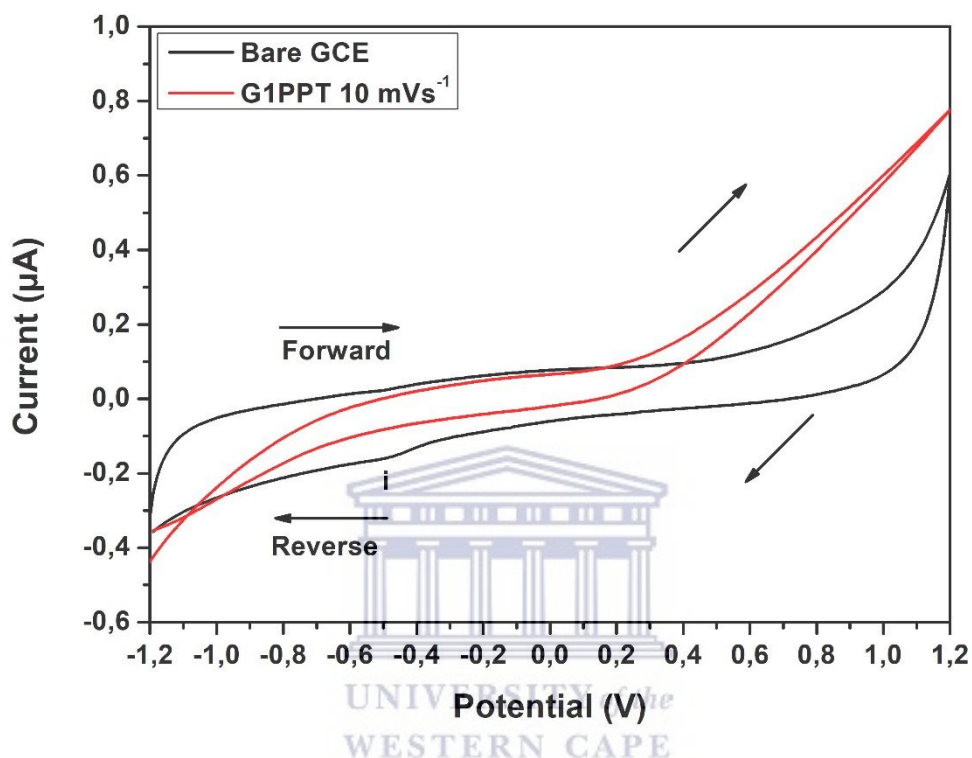
Figure 3.8 Cyclic voltammograms of bare GCE and G1PPT/GCE in 0.05 M TBAClO4/chloroform solution at 10 mVs⁻¹ scan rate

G1PPT was further studied using cyclic voltammetry technique. Figure 3.8 above represents the cyclic voltammograms of bare GCE and G1PPT in the range -1.2 V to +1.2 V vs. Ag/AgCl at scan rate of 10 mV s⁻¹. As can be seen, G1PPT displays no distinct oxidation or reduction peaks. The only visible electrochemical activity is the change of shape of the voltammogram, indicating that the presence of a modified electrode surface. The peak marked **i** appearing at -0.52 V is attributed to oxygen [216], a residual amount present due to possible incomplete bubbling before experiments were conducted. An increase in current

was observed for the G1PPI modified electrode over the bare GCE owing to the nano-dimensional nature of PPI which increases the surface area of the electrode. [217].
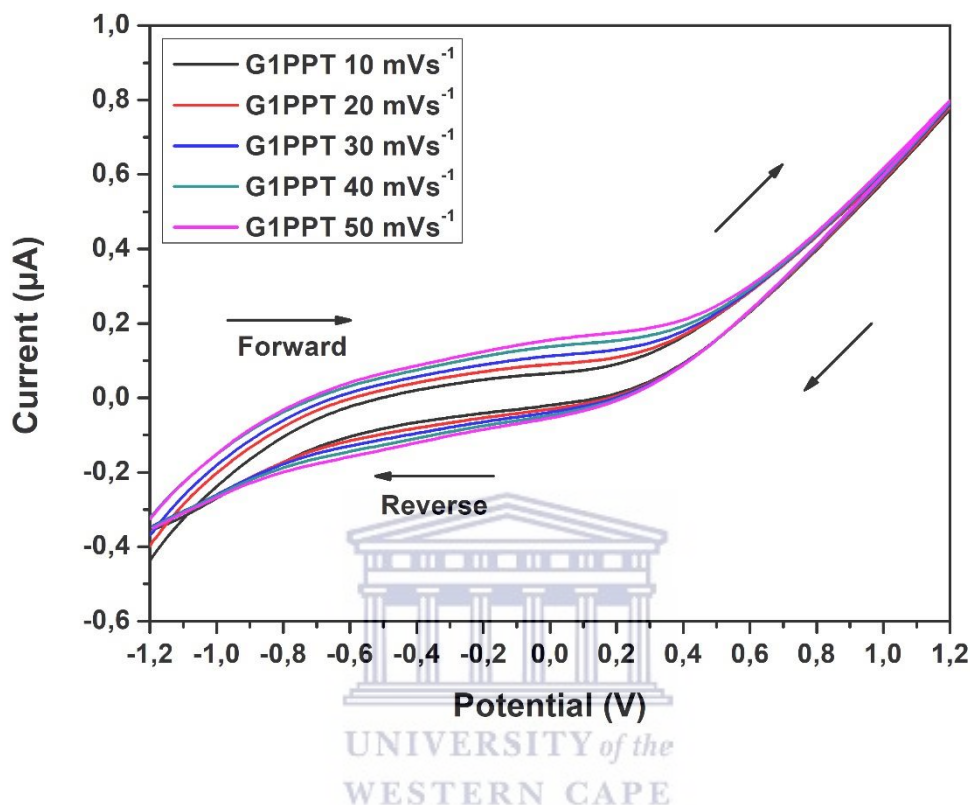
Figure 3.9: Cyclic voltammograms of G1PPT/GCE in 0.05 M TBAClO4/chloroform solution at different scan rates

Figure 3.9 above shows the dependence of peak current and potential on scan rate (ν) from 10 to 50 mVs^{-1}. The voltammograms show a direct increase in current with an increase in scan rate, suggesting a linear relationship. This also suggests that the kinetics are diffusion controlled on the G1PPI modified electrode. Furthermore, the stability of the G1PPT film is depicted by shift in peak potential as scan rate increases. A large shift or irregular peak potential is expected when the film on the electrode is unstable or leaching into the solution, but this is not the case in Figure 3.9 [218].
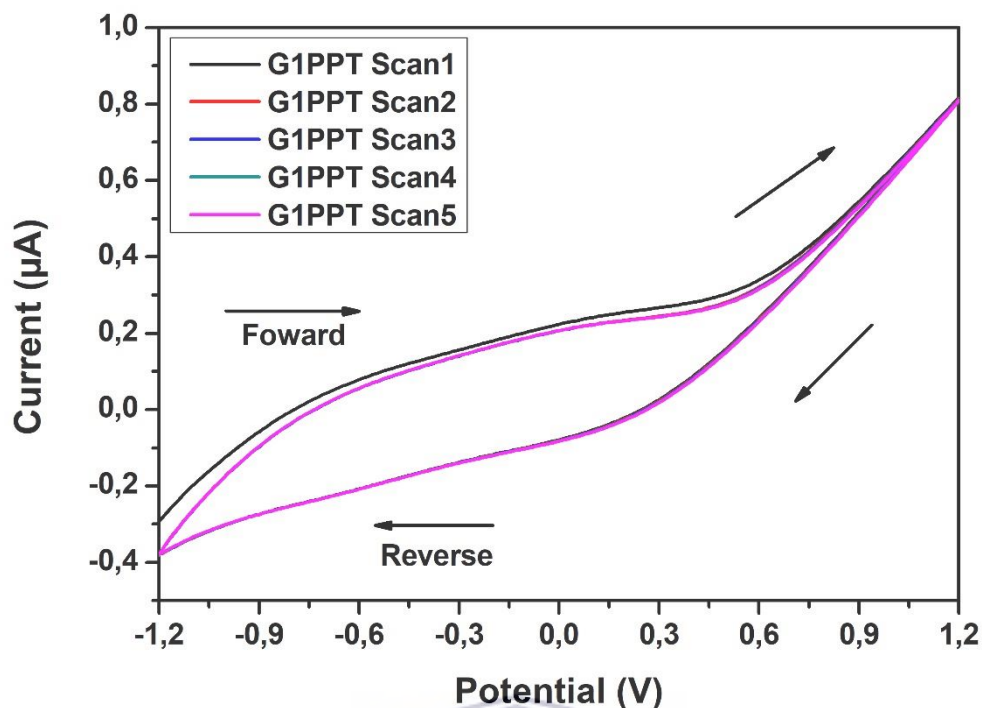
Figure 3.10: Cyclic voltammogram of G1PPT/GCE in 0.05 M TBAClO4/chloroform solution over five cycles

In rder to further confirm that the G1PPT exhibits no redox peak potentials, a sweep over five cycles under the same conditions at scan rate 10 mVs^{-1} was performed. As can be seen from Figure 3.10 above, the voltammograms remain consistent after the first sweep, showing no signs of reduction or oxidation peaks and they also show no apparent increase or decrease in peak current during the sweep. Thus, G1PPT further demonstrated a clearly stable nature.

3.3.6 Conclusion

In this work, the functionalization of generation 1 poly (propylene imine) dendrimer with 2-Thiophenecarboxladehyde was carried out. The Proton Nuclear Magnetic Resonance (^{1}H NMR) of G1PPT gave rise to a new chemical shift at 8.31 ppm for N=C-H, which confirmed

the incorporation of 2-Thiophenecarboxaldehyde into the G1-PPI dendrimer structure and Fourier transform infrared spectroscopy (FT-IR) showed a corresponding band appeared at 1673 cm^{-1} for N=C in the dendrimer moiety, and another at 755 cm^{-1} for C-H at α-position of the thiophene ring. On UV-Vis, there was shift to longer wavelengths upon incorporation of 2-Thiophenecarboxladehyde on G1-PPI. This onset shift was supported by the shift of the energy bandgap after functionalization. G1-PPI has a bandgap of 4.29 eV and the resulting G1PPT after functionalization has a bandgap of 3.11 eV. Due to its amorphous nature and therefore lack of Crystallinity, XRD showed no distinct peaks. On cyclic voltammetry, no distinct oxidation or reduction peaks were observed on the modified GCE electrode. A study of the dependence of peak current and potential on scan rate resulted in a linear relationship being observed. The G1PPT demonstrated stability due to increasing shift in peak potential with respect to scan rate. Given the results of this study, successful functionalization of G1PPI was realized.
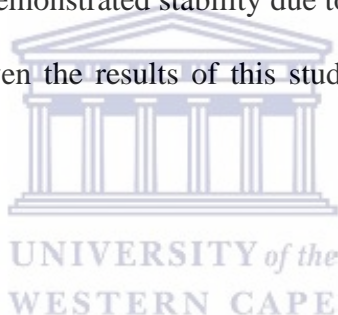
CHAPTER 4:

SYNTHESIS AND CHARACTERIZATION OF G1PPT-CuInSe$_2$ QUANTUM DOTS

4.1   Introduction

Semiconductor nanocrystals or quantum dots (QDs) exhibit an abundance of size-dependent physical and chemical properties, including quantum confinement effects, shape-dependent electronic structure, and control over assembly using different surface capping agents [219–221]. These unique electronic and optical properties have rendered them a leading novel class of light-absorbing and -emitting materials for many applications such as photovoltaics (PVs), light-emitting diodes (LEDs), thin-film transistors, etc [222–224]. Several binary QDs, like CdSe, CdTe, Cu$_2$S, InP, and InAs, have been explored for photovoltaic devices [224–228]. Most of these QDs, however, are derived from toxic heavy metals and this often raises concerns about their impact on the environment, especially in large-area deployment, such as in the case of solar cells, is sought [229–231]. For this reason, a lot of research is focused on developing alternative materials that are environmentally friendly and can be used daily. Ternary I-III-VI$_2$ type QDs such as CuInS$_2$, CuInSe$_2$, and Cu(InGa)Se$_2$ (CIGS) are suitable alternatives to heavy metal-containing QDs since they are prepared using nontoxic precursors. These greener materials preserve hope for today's technological applications for their quality of low cost and easy processing [232–234]. The ternary QDs family demonstrates the ternary family a wide emission window compared to their binary counterparts due to their size and composition variation. In addition, these materials have a longer excited-state lifetime, spectral broadening of a large full width at half-maximum (fwhm), wide Stokes shifts, high quantum efficiency, easy and cost-effective synthesis, and certainly have all greener elements [235–237].
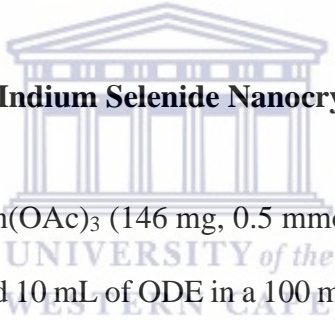
Among these materials, CuInSe$_2$, with a direct energy bandgap of 1,04 eV in its bulk state and an absorption coefficient that exceeds 3×10^4 cm^{-1} at wavelengths below 1000 nm has been widely exploited in the fabrication of low-cost photovoltaic devices [238–240]. For example, De Kergommeaux *et al* [241] prepared CuInSe$_2$ of low size and shape distribution for application in thin-film photovoltaics. They were able to obtain a current density of 1 µA/cm^2 at 1 V in the dark, which increases to 16 µA/cm^2 under illumination with white light; which they determined using *I/V* measurements of a 1 µm thick film sandwiched between the ITO substrate and an aluminum electrode. Pernik *et al* [242] fabricated plastic photovoltaic devices (PVs) by spray-depositing CuInSe$_2$ nanocrystals into micrometer-scale groove features patterned into polyethylene terephthalate (PET) substrates. Using the active area and photovoltaic response of devices determined from light-beam-induced current (LBIC) and photoreflectivity measurements gave PCE values as high as 4.4%. Near recent, Kondrotas *et al* [243] synthesized CuInSe$_2$-ZnSe (CZISe) thin films by a two-step sequential process and proceeded to study its photovoltaic properties. The cell they prepared demonstrated an efficiency of 7,6% with an open-circuit voltage as high as 520 mV, which showed a possible application in the development of sustainable, cost-efficient and critical raw materials reduced thin-film photovoltaic technologies. There are other reports of CuInSe$_2$ prepared by vacuum methods with showing efficiencies of up to 15% [244, 245].

Dendrimers have gained attention as effective multifunctional capping agents for MNPs and QDs due to their unique structural qualities, dendritic effect and polydentate nature [189, 199, 246]. Here, we have prepared (in a non-coordination solvent) and functionalized CuInSe$_2$ QDs capped with g1-poly (propylene thiopheneimine) dendrimer. The proof for potential application of CuInSe$_2$ QDs in solar devices such as hybrid solar cell devices and the determination of the electrical properties were done.

4.2   Experimental Protocols

4.2.1   Chemicals and Materials

All manipulations were carried out using standard Schlenk line technique under dry argon.

Copper (I) Chloride (CuCl)Zinc acetate, indium(III) acetate (Aldrich, 99.999%), selenium

(Aldrich, 100 mesh, 99.5%,), oleic acid (OA, Aldrich, 90%), tri-*n*-octylphosphine (TOP,

Aldrich, 90%), 1-Dodecanethiol (98%, Sigma Aldrich), 2-Thiophenecarboxaldehyde (98%;

Sigma Aldrich), DAB-Am-4, Polypropylenimine tetramine dendrimer, generation 1 (Sigma

Aldrich) and 1-octadecene (ODE, Aldrich, 90%) were used as purchased and without further

purification.

4.2.2   Synthesis of Copper Indium Selenide Nanocrystals

CuCl (49 mg, 0.5 mmol) and In(OAc)$_3$ (146 mg, 0.5 mmol) were mixed with 1,24 g of G1-

PPI, 1,2 ml 1-dodecanethiol and 10 mL of ODE in a 100 mL three-necked flask. The mixture

was degassed at 120 °C for 30 min, then 0.5 mL of oleic acid was added into the solution,

and the solution was degassed continuously for another 30 min. After that, the solution was

heated to 210 °C under argon/N$_2$ flow. 2 mL of TOPSe precursor (made by dissolving 1

mmol of Se powder in 0.5 mL of TOP and 1.5 mL of ODE) was injected swiftly into the

flask and kept for a fixed 3 hours at the same temperature. During the reaction, aliquots were

taken via syringe at different times to monitor the growth of CuInSe$_2$ NCs by recording UV–

vis and PL spectra. Afterward, the reaction solution was cooled to room temperature and

precipitated by acetone, the flocculent precipitate formed was centrifuged, the upper layer

liquid was decanted, and then the isolated solid was dispersed in chloroform and re-

precipitated by adding acetone. The centrifugation and precipitation procedure were repeated

at least twice for purification of the prepared CuInSe$_2$ QDs. Finally, the final products were redispersed into chloroform for measurements.

4.2.3   Instrumentation

4.2.3.1 Optical Studies

Ultraviolet-visible (UV-Vis) absorption measurements were made using a quartz cuvette in a Nicolet Evolution 100 UV–visible spectrometer (Thermo Electron, UK). The measurements for most of the samples were carried between 200 – 1100 nm using both D2 (Deuterium) and W (tungsten) lamps. All the samples were dispersed in chloroform and the standard consisted of only chloroform. Also, to ensure good absorbance peaks while avoiding noise, the samples were sufficiently diluted.

High-resolution transmission electron microscopy (HR-TEM) images were recorded using a using Tecnai G2 F20X-Twin MAT 200kV Field Emission Transmission Microscopy from FEI (Eindhoven, Netherlands). X-ray diffraction (XRD) for the phase identification of the crystalline structures of G1PPT-CuInSe$_2$ was performed by using a Bruker AXS D8 Advance diffractometer (voltage 40 kV; current 40 mA). The XRD spectra were recorded in the range of 10-80 degrees. Raman spectra were recorded with a laser-spectrometer LABRAM HRVIS (model Jobin-Yvon) fitted with an Olympus BX41 optical microscope (from France). Raman spectra are usually excited using the 532 nm laser. Spectra were collected over the range 0–4000 cm^{-1}. All Fourier-transform Infrared spectroscopy (FT-IR) spectra were recorded on spectrum 100 FTIR spectrometer (PerkinElmer, USA) in a region of 450 to 4000 cm^{-1}. Small-angle X-ray scattering (SAXS) measurements were collected using a SAXSpace system (Anton Paar, Ashland, VA, USA).

All electrochemical measurements were done using BAS100W integrated automated electrochemical work-station from Bio Analytical Systems (BAS), Lafayette, USA, and Princeton Applied Research Potentiostat model 273A. Cyclic voltammograms were recorded with a computer interfaced with BAS 100W and Princeton 273A electrochemical work station using a 10 mL electrochemical cell with three electrodes set up was used. The electrodes used in the study were (1) glassy carbon working electrode (GCE) (A = 0.071 cm^2) from BAS, (2) platinum wire from Sigma Aldrich acted as counter electrode and (3) Ag/AgCl from BAS kept in (3 M NaCl) was the reference electrode and alumina micro polishing pads were obtained from Buehler, LL, USA and were used for polishing the gold electrode before modification.

4.3   Results and Discussion

When it comes to binary II-VI semiconductor nanocrystals, balancing nucleation and growth by careful selection of suitable precursors and coordination ligands or systematic temperature control has been of utmost importance for their synthesis. A significant challenge for the synthesis of ternary I-III-VI$_2$ QDs is the control of their composition. Balancing the reactivity of the two cationic precursors by their ligands, solvent matrix composition, and the reaction temperature is critical to fine-tune the composition of ternary I-III-VI$_2$ QDs [247–249]. Understanding the synthesis of these types of QDs benefits from the HSAB theory. Cu^+ is a soft Lewis acid and In^{3+} is a soft Lewis base, therefore in a reaction flask, one gets two otherwise identical metal precursors (e.g., CuCl and InCl$_3$) with an inherent difference in reactivity. In addition, according to the HSAB theory, chalcogen anions such as Se^{2-} are soft bases; hence the synthesis of I−III−Se$_2$ QDs is therefore challenging, due to strong preferential bonding of Se and Cu precursors [250]. In this present

49

study, our synthesis is a slight modification of the approach developed by Xie *et al* [251] which involves an injection of elemental S solution into the reaction mixture, containing Cu and In precursors, dodecanethiol, oleic acid, and octadecene at 180 °C. Long-chain alkanethiols are a crucial part of this synthesis. Dodecanethiol preferentially complexes the reactive soft acid Cu^+ since according to the HSAB theory, it is a Lewis base. To balance reactivity between the Cu^+ and the In^{3+}, therefore requires an excess of dodecanethiol in the reaction flask. In a procedure reported by Zhong *et al* [252] for the preparation of $CuInS_2$ NCs, it was demonstrated that an intermediate complex of $CuIn(SC_{12}H_{25})x$ was formed and then subsequently decomposed into clusters which grew into $CuInS_2$ NCs. They then later refined this method and were able to obtain high-quality pyramidal $CuInS_2$ NCs [253]. In our work, we stand to reason that the intermediate Cu-In-(S-R)x clusters can react with TOPSe (TOP: tri-noctylphosphine) to grow $CuInSe_2$ QDs by cleaving Cu-S or In-S bonds [253, 254].
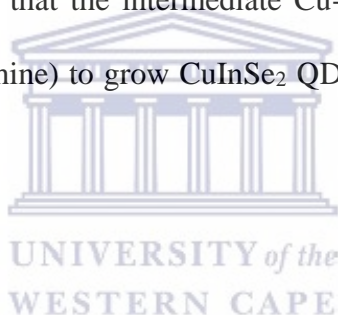
4.3.1 Uv-Vis Spectrometry of G1PPT-CuInSe₂ QDs

51

B
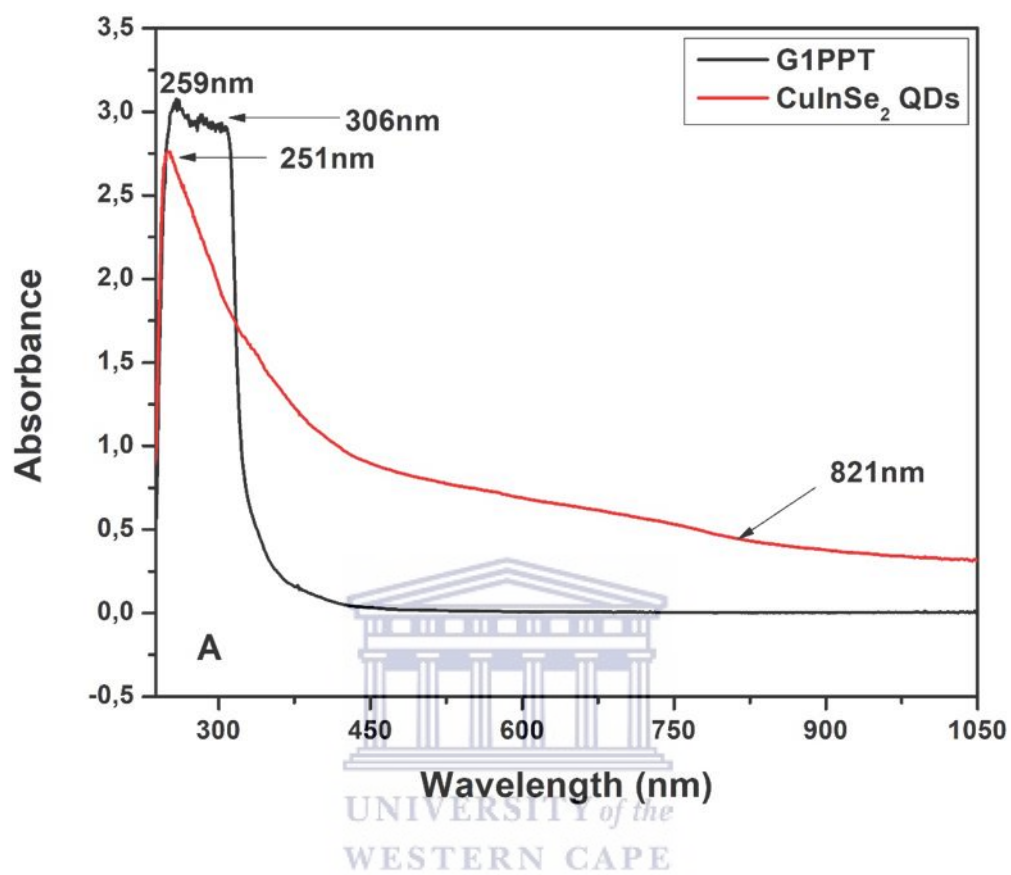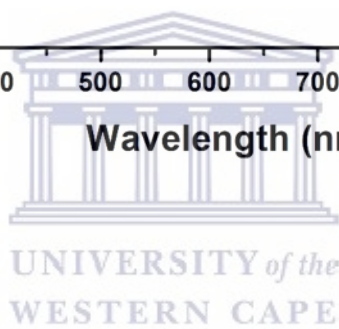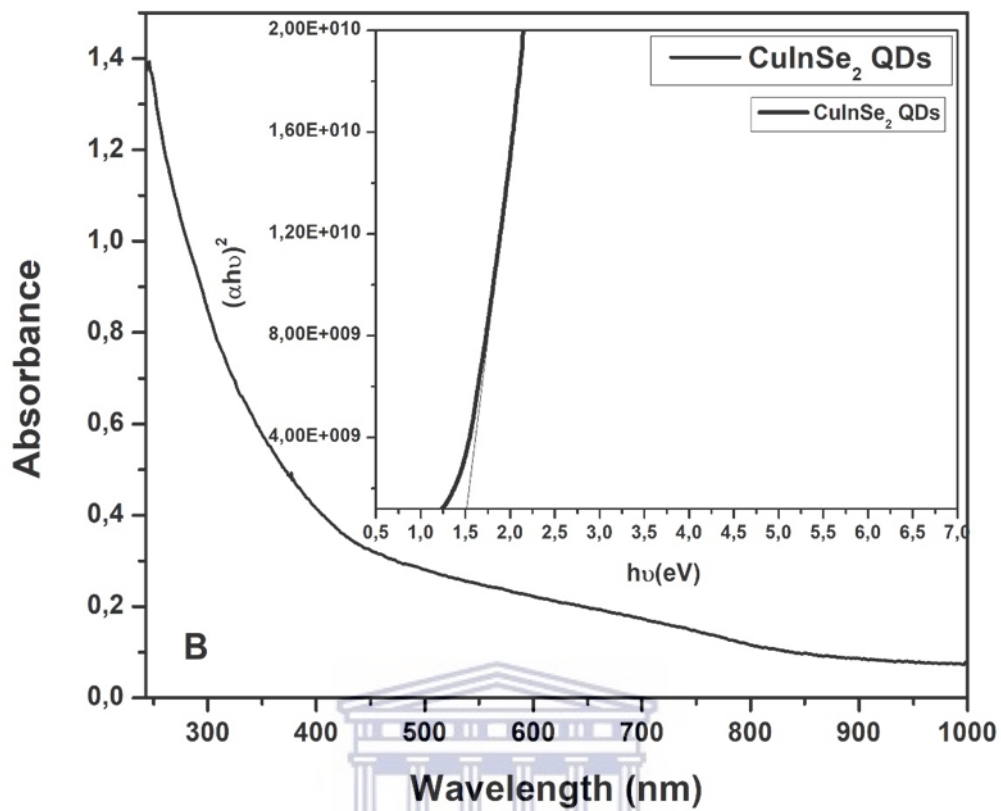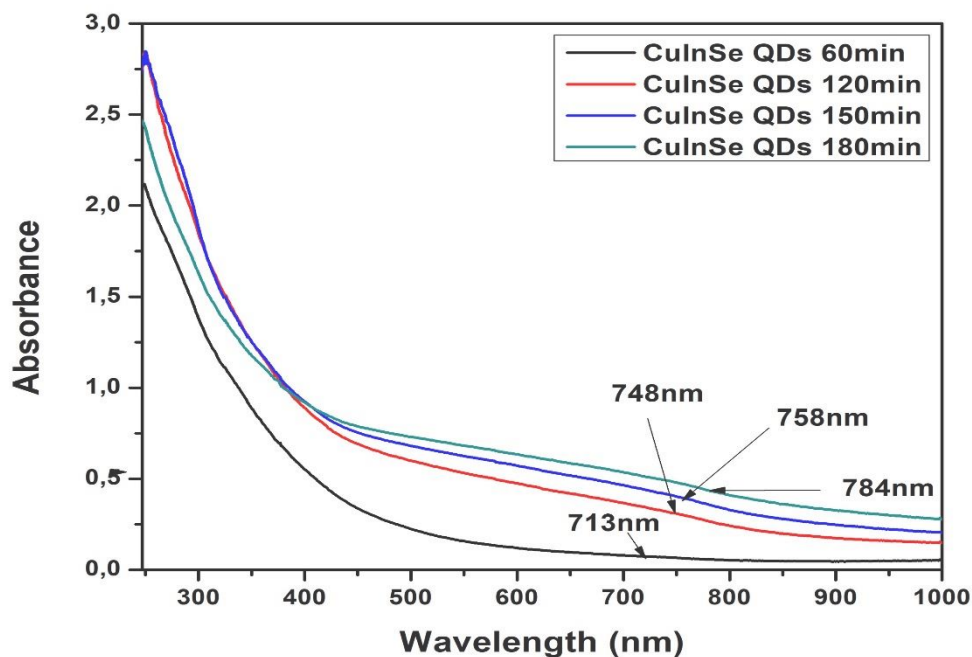
Figure 4.1: UV-Vis Spectra of (A) G1PPT and CuInSe2 QDs (B) CuInSe2 QDs insert Tauc plot (C) CuInSe2 QDs at different time intervals

The absorption spectra of G1PPT and CuInSe$_2$ QDs is shown above (figure 4.1A). In general, polymers are known to have a broad absorption peak over a wide spectrum range as can be seen above. The two peaks appearing in the spectrum of G1PPT at 259nm and 306nm are characteristics of the absorbance of the two chromophores C=N and C-S-C respectively, present in the functionalized dendrimer whose transitions are respectively π-π* and n-π*. In fact, these peaks were already identified in chapter 3 on the characterization of G1PPT. The peak at 306nm disappears in the absorption spectrum of CuInSe$_2$ QDs indicating that the S site has effectively passivated the surface of the QDs. Figure 4.1B shows the absorption spectrum of QDs with the absorption onset extending to 821 nm, suggesting the superior light-harvesting capacity for application in PV devices [255]. The Tauc plot (Figure 4.1B

inset) extrapolation shows the bandgap of typical CuInSe$_2$ QDs can be determined at 1,51 eV. This value is slightly larger compared to the bandgap of 1.16 eV reported for CuInSe$_2$ QDs with tetragonal structure and 7.0 nm size by other authors [256]. The evolution of absorption spectra during a typical growth of CuInSe$_2$ QDs at 200 ^{o}C is shown in figure 4.1C. There is a gradual shift to longer wavelengths that can be observed in the absorption spectra of QDs. Similar to previous reports, there is no apparent excitonic peak that was observed for the existence of inherent and surface trap states [257, 258].

4.3.2   Particle Morphology and Chemical Composition G1PPT-CuInSe2 QDs
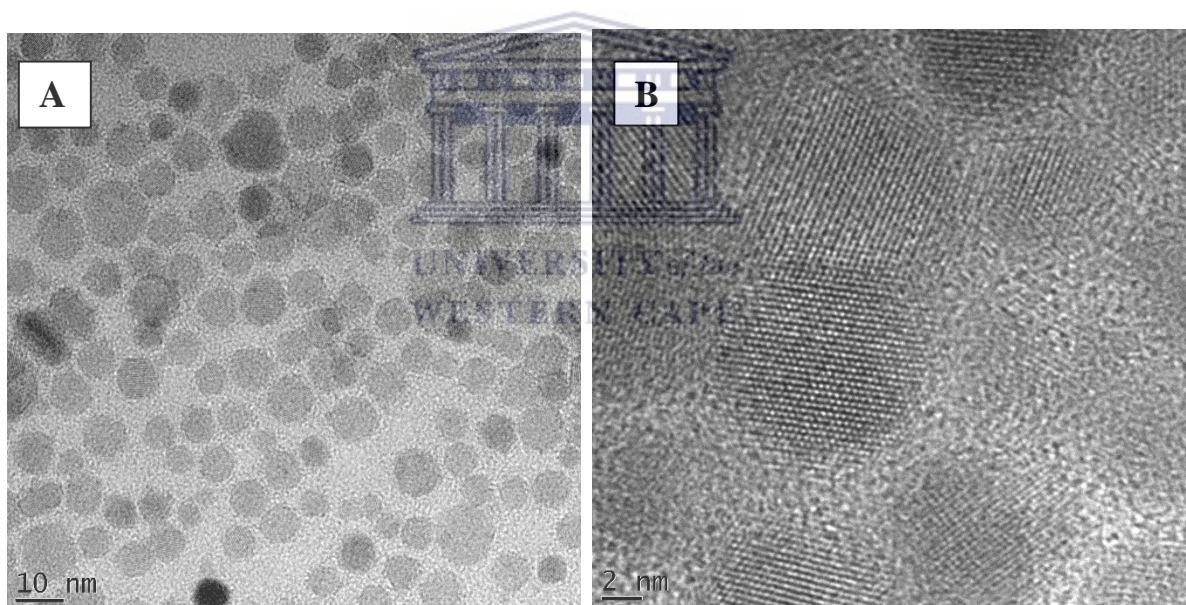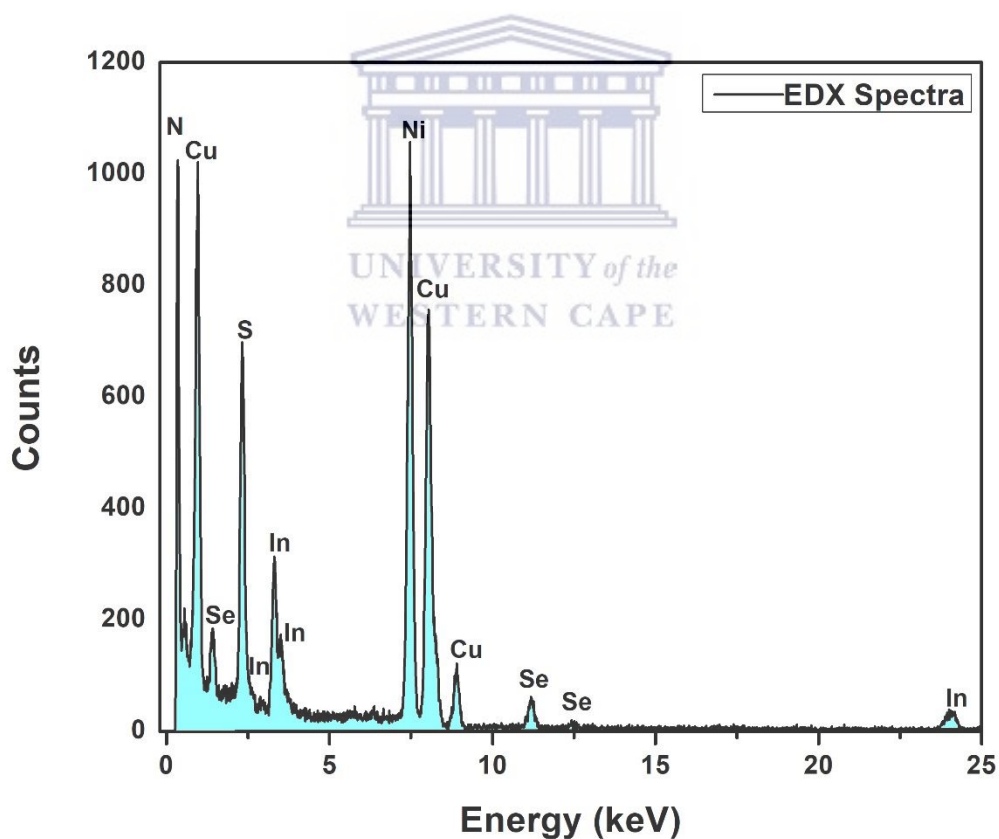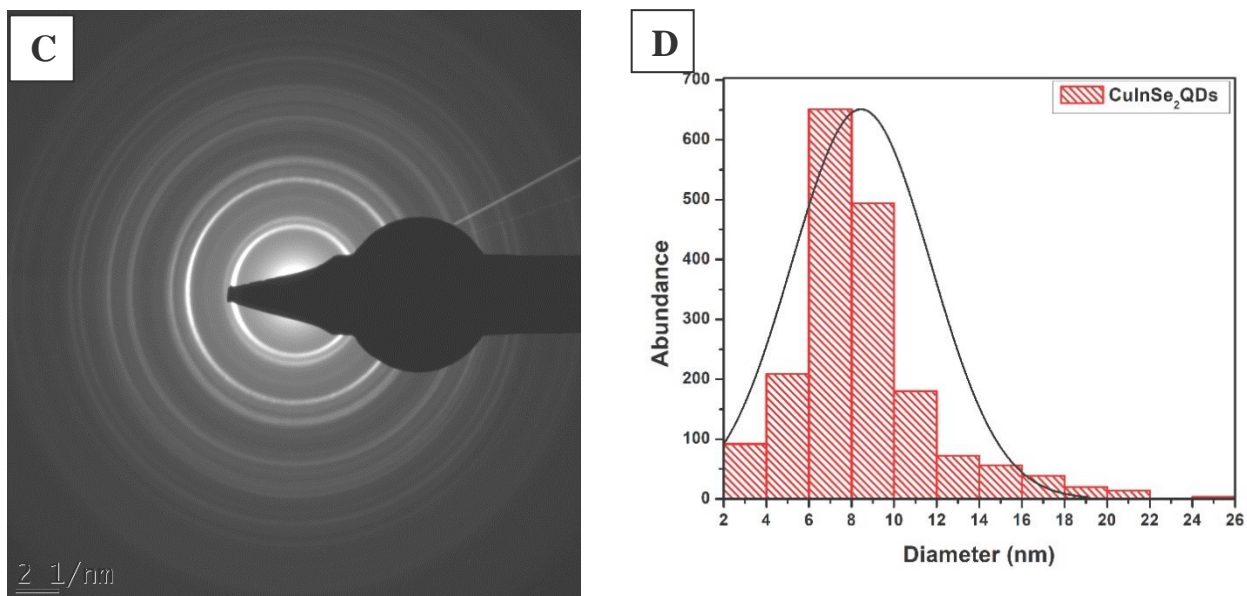
Figure 4.2: TEM Images of CuInSe2 QDs A and B respectively; with C the SAED showing crystallinity of CuInSe2 QDs; and D the EDS spectrum showing the elemental composition of the QDs

The crystal structures of individual CIS QDs were examined using transmission electron microscopy (TEM). The TEM images of the as-prepared CuInSe$_2$ QDs together with their size distributions and EDS spectrum are shown in figure 4.2. The EDS spectrum confirmed the presence of copper, indium, and selenium in the prepared QDs. The nickel appearing in excess in the spectrum is from the grid. The crystal quality was evidenced by the continuous lattice fringes and very clear crystal facets [257, 259, 260] as can be seen from a high-resolution TEM (HR-TEM) image of an individual CISe nanocrystal (figure 4.2 B) and further from the selected area electron diffraction (SAED) pattern (figure 4.2 C), which also exhibits multiple diffraction rings corresponding to CISe. The particles exhibit a pentagonal shape and are nearly monodispersed with a small degree of agglomeration since repeated sonication has been employed before TEM analysis [259–261]. The average size of the as-prepared CIS QDs determined from TEM is 8.5 nm.
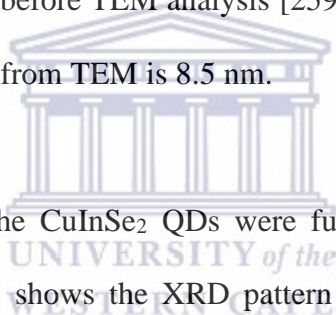
The structural properties of the CuInSe$_2$ QDs were further studied with X-ray powder diffraction (XRD). Figure 4.3 shows the XRD pattern of CuInSe$_2$ QDs prepared using G1PPT as a capping agent. Bragg's reflections for CuInSe$_2$ QDs are observed in XRD pattern at 2θ value of 27,71°, 46,39°, 54,63° representing (111), (220) and (311) planes of the zincblende metastable structure of CuInSe$_2$ [260, 262]. There is a very small difference between the chalcopyrite phase and zincblende phases, the CuInSe$_2$ NCs with zincblende phase usually have a diffraction peak of (200), which in the present case can be identified on the broad and prominent peak [253]. The energy dispersive X-ray Spectroscopy (EDS) (figure 4.2 E) confirmed the close-to 1:1:2 stoichiometry, with the tendency to be slightly copper-rich. The crystal diameter of the CuInSe$_2$ QDs was approximated to be 6.3 nm using the Debye–Scherrer equation ($D=0.9\lambda/\beta \cos \theta$), where D is the crystal size, λ is the wavelength of X-ray, θ is the Braggs angle in radians, and β is the full width at half

maximum of the peak in radians. The size calculated from XRD was less than the size calculated from TEM. Peak broadening is usually attributed to decreasing nanocrystal size, but in this case, the effect is due to the amorphous nature of the bulky dendrimer masking the nanocrystals [263].
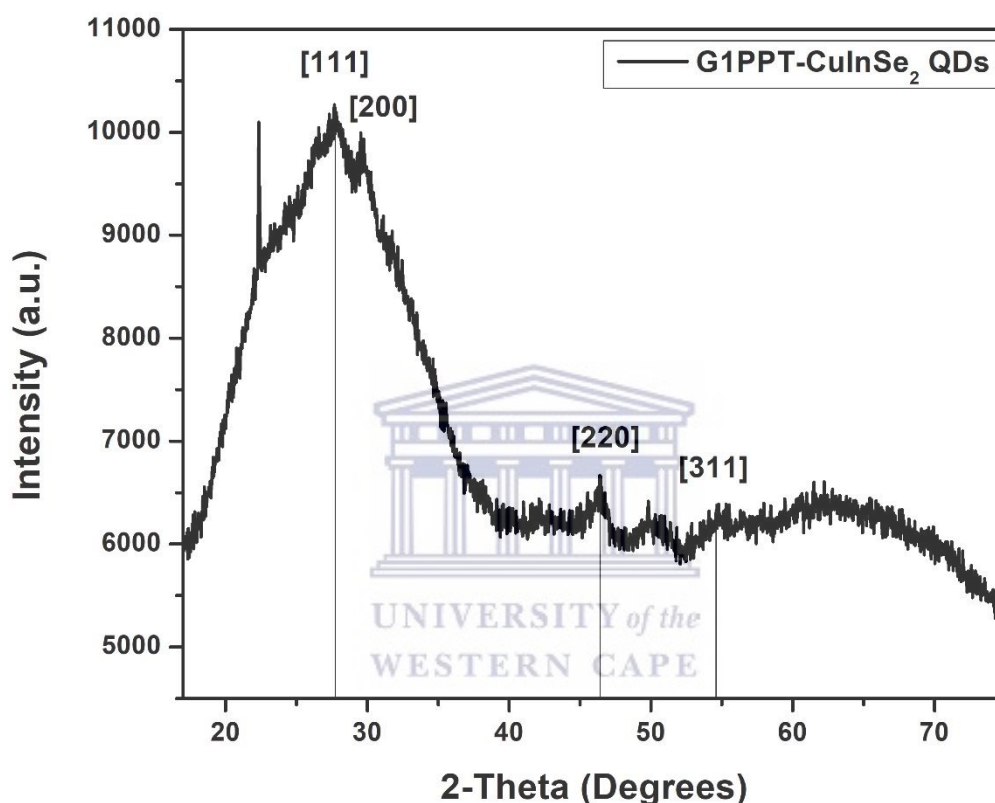
Figure 4.3: Powder X-ray diffraction (XRD) pattern of CuInSe2 QDs.

In addition, Raman measurement was conducted to further check the phase purity and crystal structure of the as-synthesized CISe nanocrystals. Figure 4.4 below shows the Raman spectrum of $CuInSe_2$ nanocrystals prepared at 210 °C. The peak attributed at 169 cm^{-1} corresponds to the characteristics of the A1 mode of the chalcopyrite CISe phase. A1 mode represents the vibration of the Se in the x–y plane with the cations at rest [264, 265]. The peaks at about 212 cm^{-1} and 225 cm^{-1} are usually attributed to the B2 and E vibration mode

of CuInSe$_2$ chalcopyrite modes [266, 267]. Thus, the main phase of the CIS dots synthesized in this study is CuInSe$_2$. However, the occurrence of binary compounds is largely expected in these systems due to decomposition and/or compositional issues [266], and a result, a small shoulder attributed at 259 cm^{-1} to the as-deposited sample is related to the Cu-Se binary phase. Two additional peaks of In-Se [268] located at 315 cm^{-1} (main peak) and 335 cm^{-1} (secondary peak) were also identified.
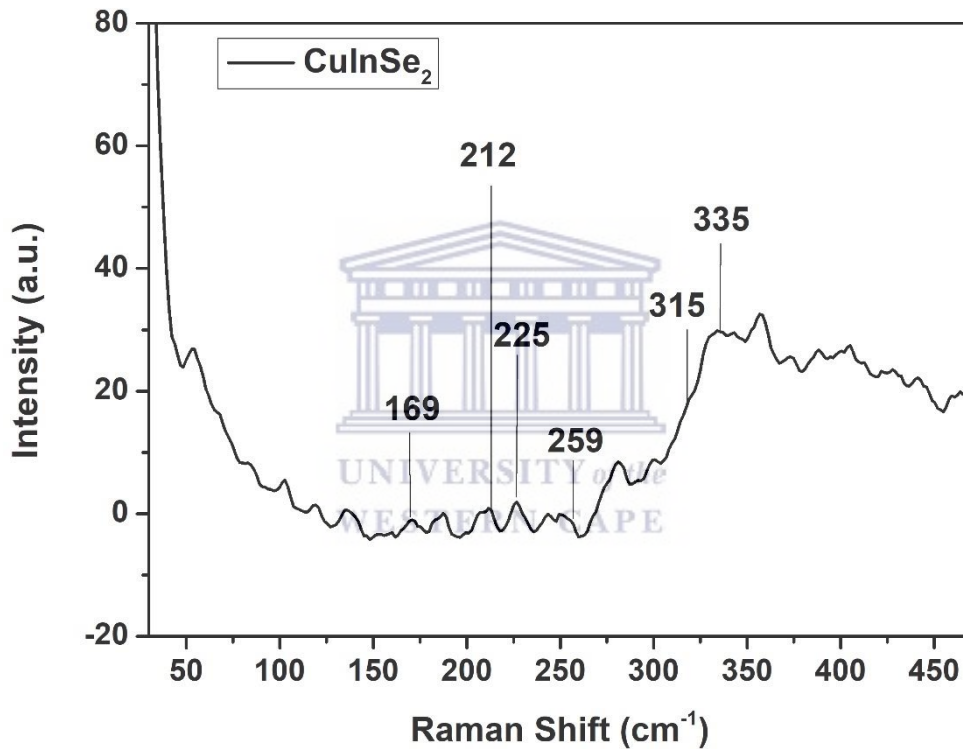
Figure 4.4: Raman spectrum of CuInSe2 prepared on a glass slide for analysis.

G1PPT and the as-prepared CuInSe$_2$ QDs were analyzed with Fourier transform infrared spectroscopy (FTIR) and their spectra are illustrated in Figure 4.5. Several peaks which are characteristic to G1PPT appear at 755, 929, 1039, 1221, 1428, 1527, 1673, 2339, 2841, 2945, 3022, 3616, 3691, 4220 cm^{-1}. In the spectrum of the G1PPT, the out-of-plane bending of C-

H bond located at the α-position to the thiophene ring was observed at 755 cm^{-1}. The medium-weak multiple bands accounting for the C=C stretching in the 5- membered aromatic ring of thiophene can be observed in the region 1039-1428 cm^{-1}. The C=N bond stretching vibration present in the dendrimer moiety appeared as a sharp band at 1673 cm^{-1}. The bands at 2841, 2945, 3022 cm^{-1} in G1PPT indicate the presence of the CH$_2$ stretch in the dendrimer moiety [206]. The peak at 891 cm^{-1} and at 661 cm^{-1} was assigned for C-S bending vibration and C-S-C ring deformation stretching. The spectrum of 1-dodecanethiol shows characteristics peaks at 2925 and 2855 cm^{-1} which are attributed to the C-H stretching vibrations. These same bands can be seen in the spectrum of CuInSe$_2$. However, the S-H vibration at 2572 cm^{-1} for 1-dodecanethiol and the C-S bending vibration and C-S-C ring deformation stretching at 891 cm^{-1} and at 661 cm^{-1} for G1PPT were absent in CuInSe$_2$ sample, suggesting the formation of metal–sulfide bonds in these compounds did occur[269–271].
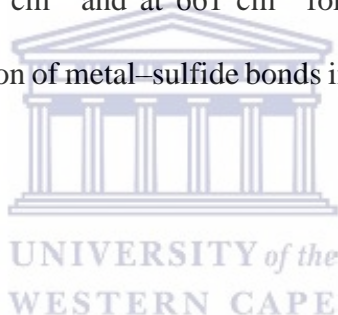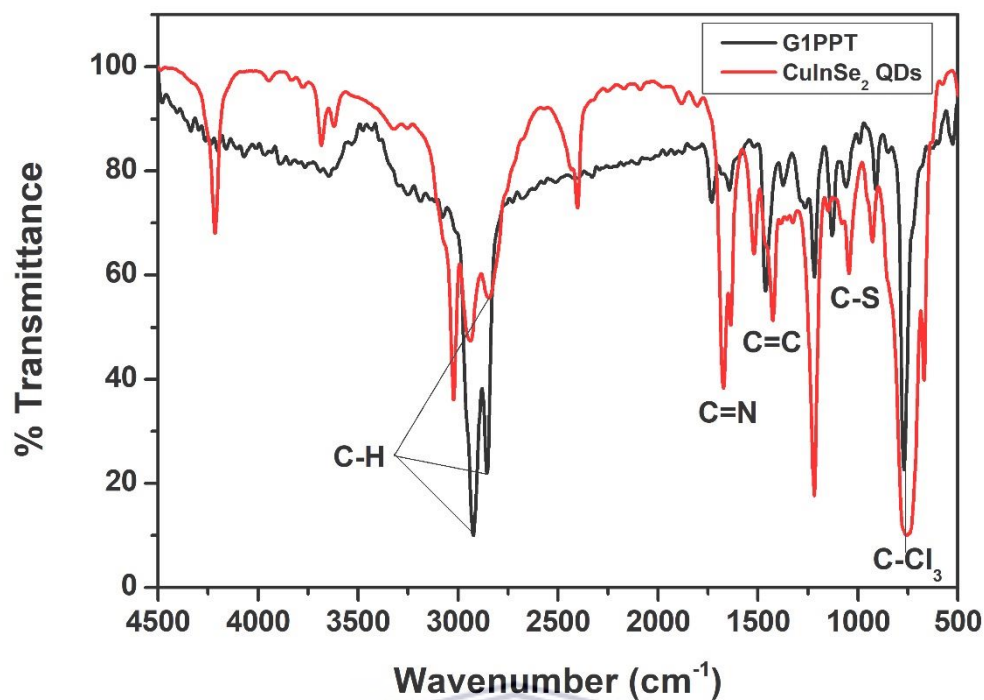
Figure 4.5: FT-IR Spectra of pure 1-dodecanethiol, G1PPT, and G1PPT-CuInSe₂ Quantum dots

B

C
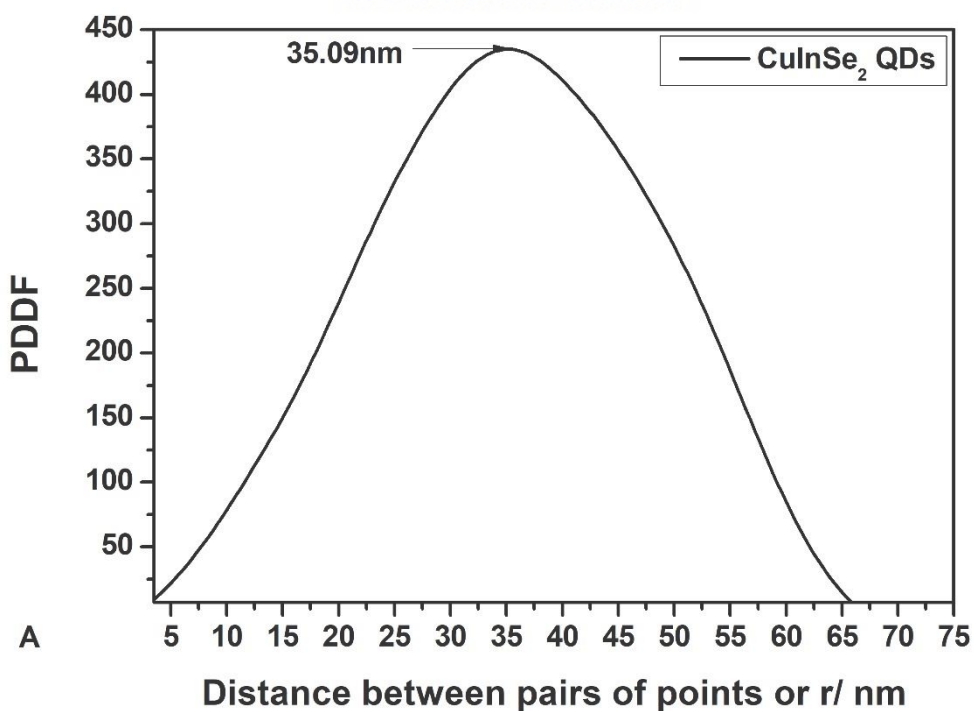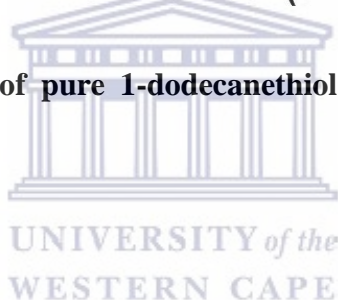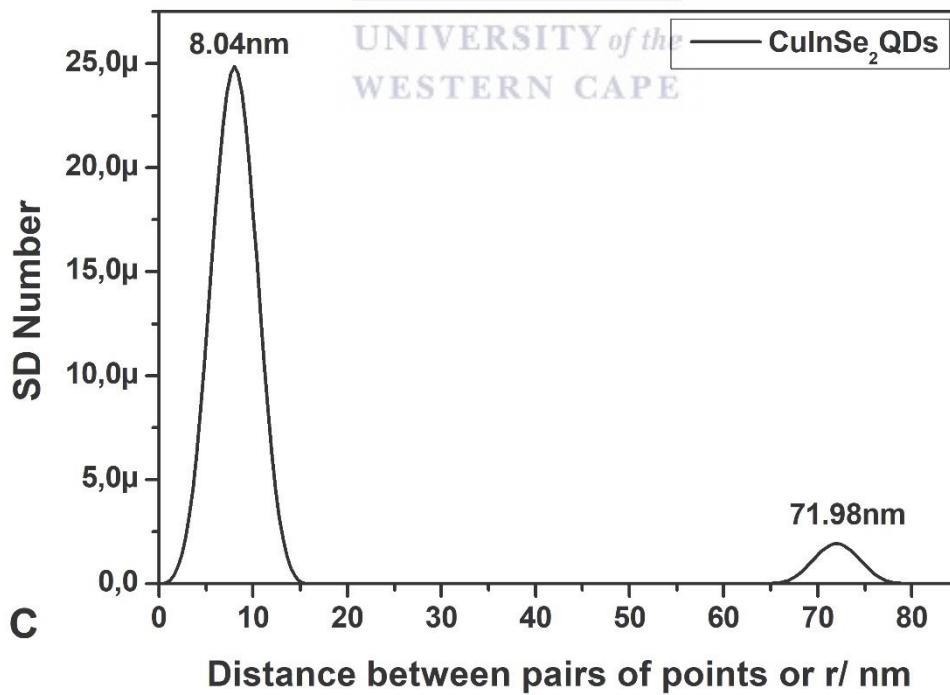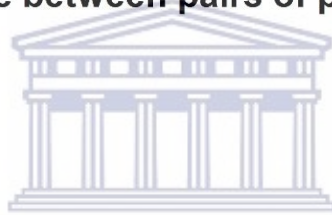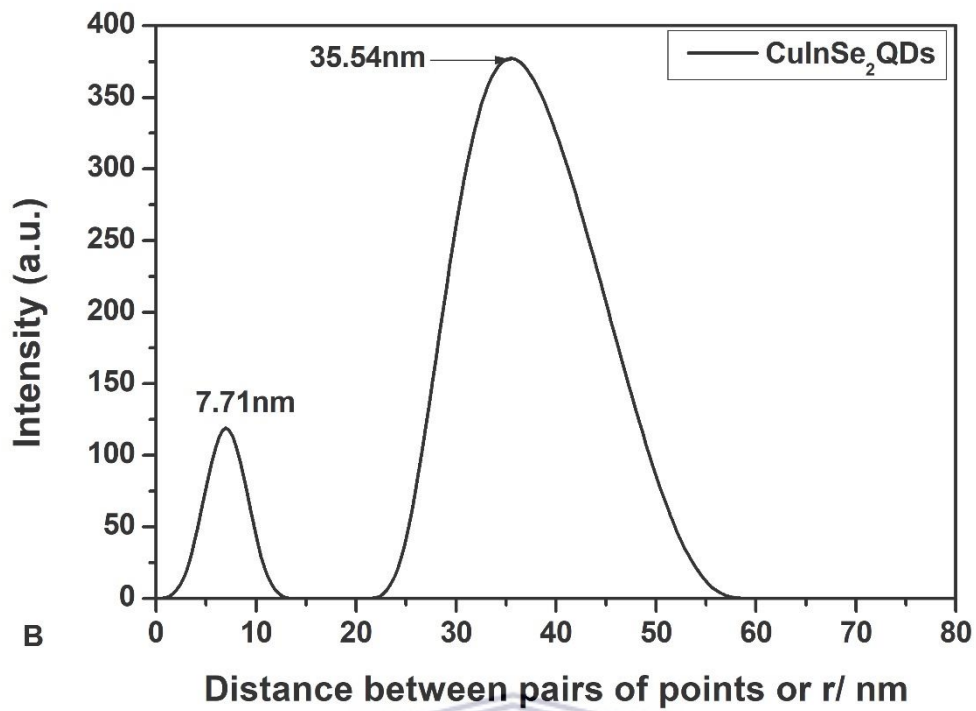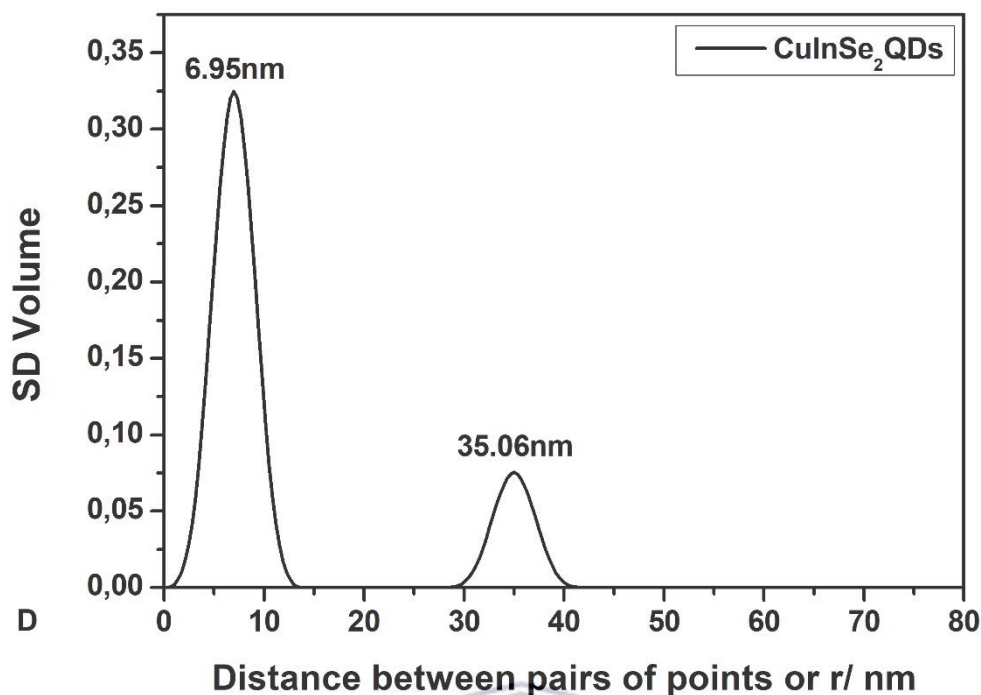
Figure 4.6: Small-angle X-ray scattering (SAXS) curves showing PDDF (A), Intensity (B), Number (C) and Volume (D) weighted curves of G1PPT-CuInSe₂ QDs

Small-angle X-ray scattering (SAXS) was further used to study the particle shape, size distribution and the internal structure of the as-prepared G1PPT-CuInSe$_2$ QDs. Figure 4.6 above displays SAXS results of PDDF number, intensity, and volume-weighted curves. From the PDDF curve (Figure 4.6 A), resembles a characteristic profile of a globular shaped structure [272–274]. The nanoparticle size distribution by particle volume (Figure 4.6 D) was determined with the indirect Fourier transformation method, assuming that the particles are globular as already discussed. A bimodal distribution was obtained with two distinct populations: the average particle diameter of population 1 (2) was determined as 6.95 nm (35.06 nm). From the ratio of the areas under the two main peaks in the size distribution

curve, the volume ratio ϕv,1/ϕv,2 could be estimated to be 4.3 [275]. The average diameter of the most dominant size was approximated close and in agreement with the particle size calculated from XRD (6.3 nm) with a 0.65 nm difference. The average particle size determined from TEM is 8.5 nm, which gives a 1.55 nm compared to the size determined from SAXS analysis. The main reason for these differences is that SAXS analysis does not separate the influence of particle shape and size distribution and when calculating particle sizes as the diameter of a sphere of equivalent cross-sectional area on the TEM images, there is also no separation of shape effects, whereas, XRD measures only the crystal structure. Hence, since SAXS and TEM visualize the whole primary particle; minor underestimates on the order of half a unit cell may occur [276, 277]. The particle size intensity curve (Figure 4.6 B) yielded the expected results, with bigger sized particles showing a high intensity due to biased interaction with the x-rays. Particle size distribution by number also shows the already expected results, population 1 had a high number of particles with an average diameter of 6.9 nm.
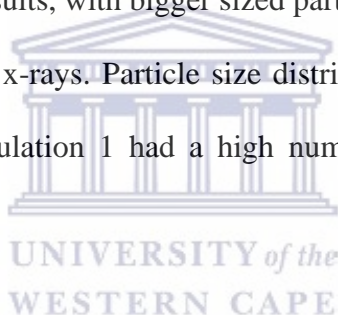
4.3.3   Electrochemical Studies of G1PPT-CuInSe2 QDs

4.3.3.1 Cyclic Voltammetry of G1PPT-CuInSe₂ QDs

There are two theoretical issues involved in using CV to map the band structures of semiconductor nanocrystals. As we already know, CV has been proven to be an effective tool to estimate the absolute energy value of the Evb (or ionization potential – Ip), Ecb (or electron affinity – Ea), and bandgap (Egap) of electroactive species including semiconductor nanocrystals [278]. The approach to extract this information is however still under contention. In some cases, for example, the peak potentials of the redox waves in the CV

curves were adopted to correlate with the Evb and Ecb energy levels [278–280], while the onset redox potentials were used instead for performing such correlation in other cases [281–284]. It is then necessary to first determine the principle to map out the band structures of semiconductor nanocrystals using CV in order to clarify this issue. The electrochemical oxidation of QDs corresponds to the removal of electrons from their valence bands to the electrode, while the electrochemical reduction to the injection of electrons into their conduction bands from the electrode. This is similar to the well understood e electrochemical investigation of the conjugated polymer [278, 285]. During a potential sweep, the electron removal and injection process should be started from the valence band edge (the highest occupied energy level) (HOMO) and the conduction band edge (the lowest unoccupied energy level) (LUMO) , respectively, owing to the energy limitation as well as the discrete energy level structures of QDs. For this reason, it is more rational to correlate the band edge energy levels (Evb and Ecb) with the onset redox potentials. It should, however, be stressed that the onset redox potentials should be determined by finding the intersections of the tangent of the peaks with the extrapolated baseline in order to overcome background interference. In addition, the CV curves need to be recorded at a low scan rate ($\geq$30 mV s^{-1}) so that the overpotential to initiate the redox reactions can be significantly reduced. The relationship between the band edge energy levels and the onset redox potentials can be described by the following equations:

$$E_{vb} = -I_p = -\left(e.\varphi_{ox}{}' + E_{ref}\right) \ eV \tag{6}$$

$$E_{cb} = -E_a = -(e.\varphi_{red}{}' + E_{ref}) \ eV \tag{7}$$

Where $\varphi_{ox}{}'$ and $\varphi_{red}{}'$ are the onset redox potentials relative to a selected reference electrode, while E_{ref} is the potential difference between the selected reference electrode and the vacuum energy level [278, 284–287]. If a saturated calomel electrode (SCE) is chosen as the reference electrode, the E_{ref} is equal to 4.4 eV, while if the ferrocene/ferrocenium

couple is selected as an internal reference, the E_{ref} is equal to 4.8 eV [287, 288]. Compared to the optical excitation process, the electrochemical oxidation or reduction of QDs, no matter it is carried out in solutions or in thin films, both suffer significant influences from their dielectric environments, capping ligands, and Coulomb interactions associated with charge injection processes. Thus, E_{gap}^{el} is expected to be larger than E_{gap}^{opt} and the correlation between them can be described by the following equation:

$$E_{gap}^{opt} = E_{gap}^{el} - J_{e,h} - E_{ligand}^{bar} \tag{8}$$

where $J_{e,h}$ is the total electron-hole Coulomb interaction energy including the direct and dielectric polarization-induced Coulomb interactions on the electrons and holes in QDs, while E_{ligand}^{bar} is the additional injection/extraction barrier from surface capping ligands [289–292].
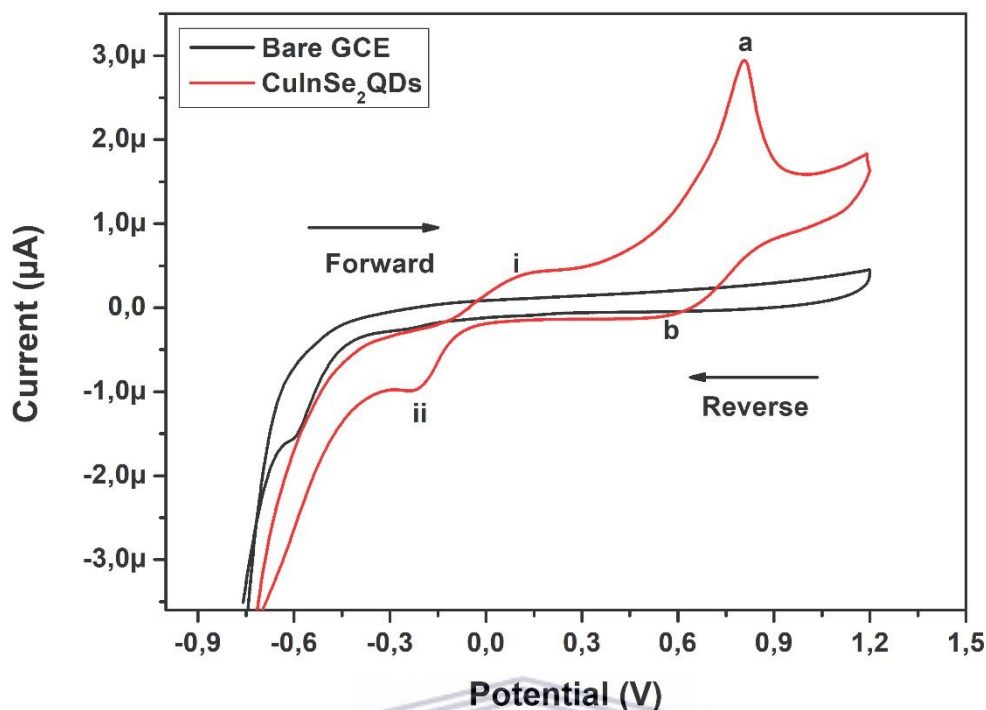
Figure 4.7: Cyclic voltammograms of bare GCE and G1PPT-CuInSe2 QDs in 0.05 M TBAClO4/chloroform solution at 10 mVs^{-1} scan rate

Cyclic voltammetry (CV) measurements were carried out under nitrogen in anhydrous solvents at a potential scan rate of 10 mVs^{-1} . The cell used three electrodes: a saturated silver chloride reference electrode (0.222 V vs. SHE), a glassy carbon working electrode, and a platinum counter electrode with a 0.05 M tetrabutylammonium perchlorate (TBAClO4)/chloroform solution (1:4 QD:TBAClO4 ratio) as an electrolyte. The QDs were not deposited onto a working electrode but instead, were dissolved directly in the electrolyte. This allows a unique opportunity to probe them in their native solution-based environment. This type of experiment is employed from Fuhr *et al* [289] and was chosen for many reasons. The first concern is the formation of intragap states due to strong dot-to-dot electronic interactions or stripping of ligands during film preparation. This challenge may not be

necessarily encountered in solution phase samples. Furthermore, cover artificial shifts in the band positions due to variations in film packing, which can affect the ability of electrolyte ions to access the surface of the QDs can be avoided [294]. Lastly, solution-phase measurements involve diffusion-limited electrochemical (EC) processes. This, therefore, mitigates concerns over the irreversibility of the oxidation step for hole injection into the VB, as not all the QDs will be oxidized during the potential sweep. Film measurements, on the other hand, generally oxidize all the QDs on the forward scan, which can possibly damage the QDs and make it difficult to determine energy levels on the reverse scan [289].

Figure 4.7 above shows a voltammogram of CuInSe QDs and bare GCE in the range -1.0 to +1.5 V vs. Ag/AgCl (0.01 M). The appearance of multiple peaks 0.122 V, -0.225 V, 0.809 V and 0.586 V marked i, ii, a and b respectively, that do not correspond to the HOMO or LUMO states can be observed on the CV curve. These peaks could be either the presence of free, unbound surface passivating ligands and/or the existence of surface trap states of QDs. Studies on size- and composition-dependent electrochemistry of copper-based ternary semiconductor (e.g., $CuInS_2$, Cu_2SnSe_3, and CuZnSeS) NCs that were investigated using the CV technique where NCs were deposited as a film onto an electrode surface, demonstrated similar results where the current potential profiles did not represent the electrochemical characteristics (position of the HOMO and LUMO and E_{gap}^{el}) of fully diffused and isolated NCs [253, 294, 295]. In their case, this was due to NCs being present in an aggregated film state, which causes a variation in the quantum confinement effects. In addition, there was the case of insulating ligand coating (oleylamine and or dodecanethiol) inside the NCs film, resulting in sluggish electron transfer, which in turn could trigger chemical reactions inside the film, causing a change in the film morphology and degradation of the sample. Lefrançois *et al* [297] effectively demonstrated the effect of different surface ligands on the quantitative

electrochemical characteristics of semiconductor NCs. In their experiments, they considered two cases: (i) NCs capped with ligands, which are electrochemically inactive in the studied potential range; (ii) NCs capped with electroactive ligands. In the first case, the electrochemical quantum confinement effect can be evidenced which is usually manifested by an increase of the potential of the first oxidation peak with decreasing NC size and by a correlated decrease of the first reduction peak potential [297, 298]. In the present study, dodecanethiol and G1PPT are the main surface passivating ligands that were employed during the synthesis of CISe QDs. Dodecanethiol is mainly used for the function of balancing the reactivity of the metals and G1PPT acts as the encapsulating ligand in order to improve the electronic properties of the CISe QDs for electroluminescent and solar cell application. However, the possible electrochemical activity of G1PPT can be cast aside since it showed no activity during electrochemical analysis. This then leaves dodecanethiol and the existence of surface trap states caused by defects as contributors to the appearance of multiple peaks.
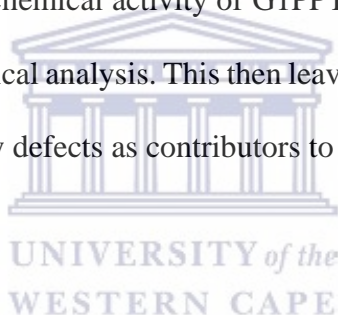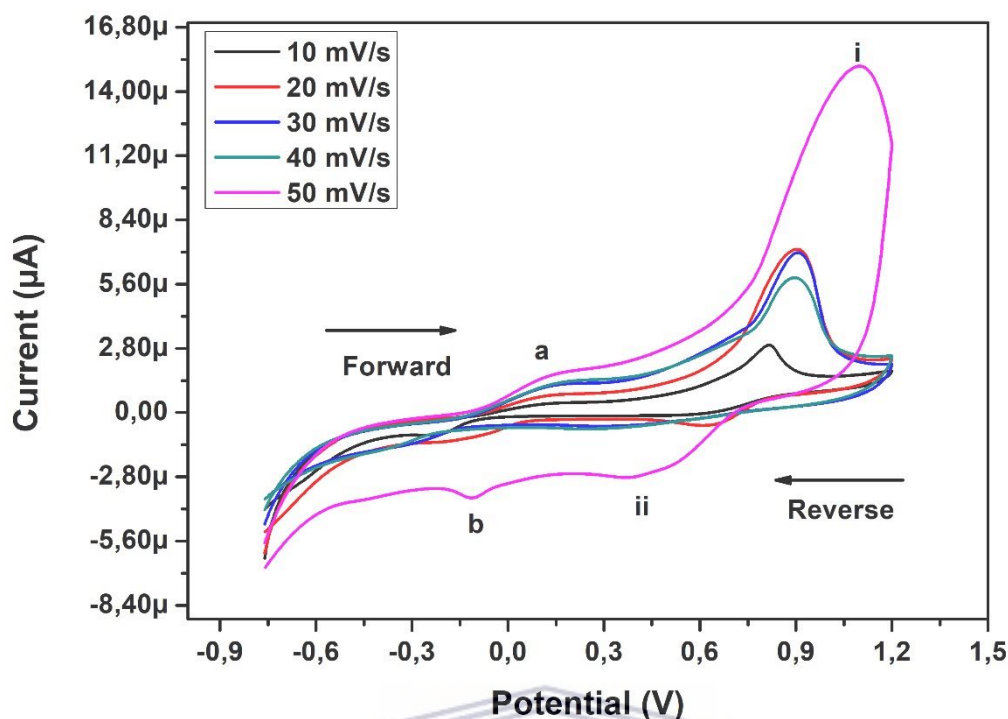
Figure 4.8: Cyclic voltammograms of G1PPT-CuInSe2 QDs in 0.05 M TBAClO4/chloroform solution at different scan rate

The dependence of peak current and potential on scan rate (v) from 10 to 50 mVs^{-1} is shown in figure 4.8 above. The voltammograms show an increase in current (I_{pc} from 10 to 20 mVs^{-1} accompanied by a shift to higher potentials of the oxidation peak. A further slightly shift to higher potentials of the oxidation peak is seen going from 20 to 30 mVs^{-1} and this is coupled by a slight decrease in I_{pc} values. There was a significant decrease in I_{pc} going from 30 to 40 mVs^{-1} and a slight shift to higher potentials. The reduction of potential peaks remained constant until 40 mVs^{-1}. The oxidation peak saw an exponential increase at 50 mVs^{-1}, while the first reduction peak moved to lower potentials. The current response showed no clear proportionality to the scan rate nor V. In Figure 4.7 and Figure 4.8 the anodic region shows two oxidation peaks marked a and i with potential values of 0.122 V and 0.809 V respectively. These peaks are proposed due to the oxidation of selenium rich/Se-

rich phase phases of $CuInSe_2$ [300]. A sweep over a wider potential window shown in Figure 4.9 revealed three reduction peaks marked c, d and e. The reduction of Cu is marked by c at -0.228 V and the reduction of Se -0497 V. The region -0.5 V to -1.2 V has a peak appearing at -0.976 V (e) assigned to the reduction of In-rich phases of $CuInSe_2$ [299–302].

A sweep over a wide potential window is required for the accurate determination of the HOMO and LUMO levels. Figure 4.9 shows a scan from -3 to +3 V vs. Ag/AgCl (0.01 M). As stated before, the experiments were carried out in solution and chloroform was used as a solvent to prepare the electrolyte, and this allowed probing of the QDs in their dissolved solvent and therefore native environment. However, with this choice came the compromise of not getting a "perfect" voltammogram that allowed for easy determination of the HOMO and LUMO levels of the QDs. The reason for this is that chloroform, together with toluene are usually used as solvent systems when conducting many electrochemical studies of QDs and they have been found to be rigid in allowing for scans over wide potential window [304]. Nevertheless, the onset oxidation and reduction potentials corresponding to the HOMO and LUMO levels of the as-prepared G1PPT-$CuInSe_2$ QDs were extrapolated and using the dotted lines. The onset oxidation and reduction potentials are 0.740 V (**E**) and -0.863 V (**F**) and the corresponding HOMO and LUMO levels are -5.140 eV and 3.537 eV, respectively. The electrochemical bandgap calculated from the previous values is 1.60 eV, which as expected from theory is slightly higher than the calculated optical bandgap (1.51 eV) of the as-prepared G1PPT-$CuInSe_2$ QDs. As observed, $E_{gap}^{el} > E_{gap}^{opt}$ and their difference can approximately be defined as $J_{e,h}$ the total electron-hole Coulomb interaction energy or exciton binding energy in simple terms. The $J_{e,h}$ valued was found to be 90 meV and is comparable to the reported value of 80 meV for typical CISe QDs.

70
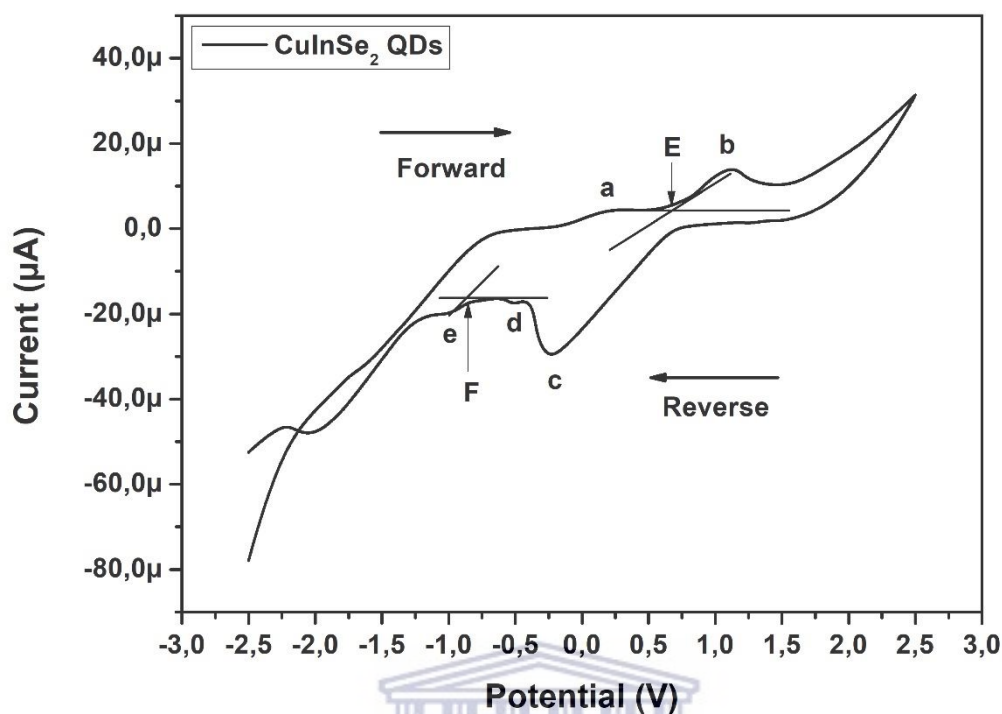
Figure 4.9: Cyclic voltammograms of G1PPT-CuInSe2 QDs in 0.05 M TBAClO4/chloroform solution at 10 mVs-1 scan rate in the range -3 V to +3 V

4.3.3.2 Electrochemical Impedance Spectroscopic Studies

EIS was used to investigate the electrical resistance and diffusion processes occurring at the electrochemical interfaces of the as-prepared G1PPT-CuInSe$_2$ QDs 0.05 M tetrabutylammonium perchlorate (TBAClO4)/chloroform solution again as an electrolyte. Figure 5.1 and Figure 5.2 below show the Nyquist and Bode plot of the G1PPT-CuInSe$_2$ QDs. The Nyquist plot consists of a semicircle that describes the electron transfer limiting process and a linear part that provides information about the diffusion-controlled processes. The Bode plot, on the other hand, gives information on the conductivity and reactivity of the G1PPT-CuInSe$_2$

71

QDs from the value of the log of the total impedance and the log frequency maxima and the phase angle plot respectively. The Randles circuit (Figure 4.12) which is a commonly used equivalent circuit for EIS data fitting was used to fit the data obtained for the as-prepared G1PPT-CuInSe$_2$ QDs. The Nyquist plot shows a well-defined semicircle with a radius of 7800 Ω. The Bode plot reveals a higher impedance to electron transfer as demonstrated by the impedance and phase angle values at low frequencies where the disturbances to the equilibrium position of the system are minimal.
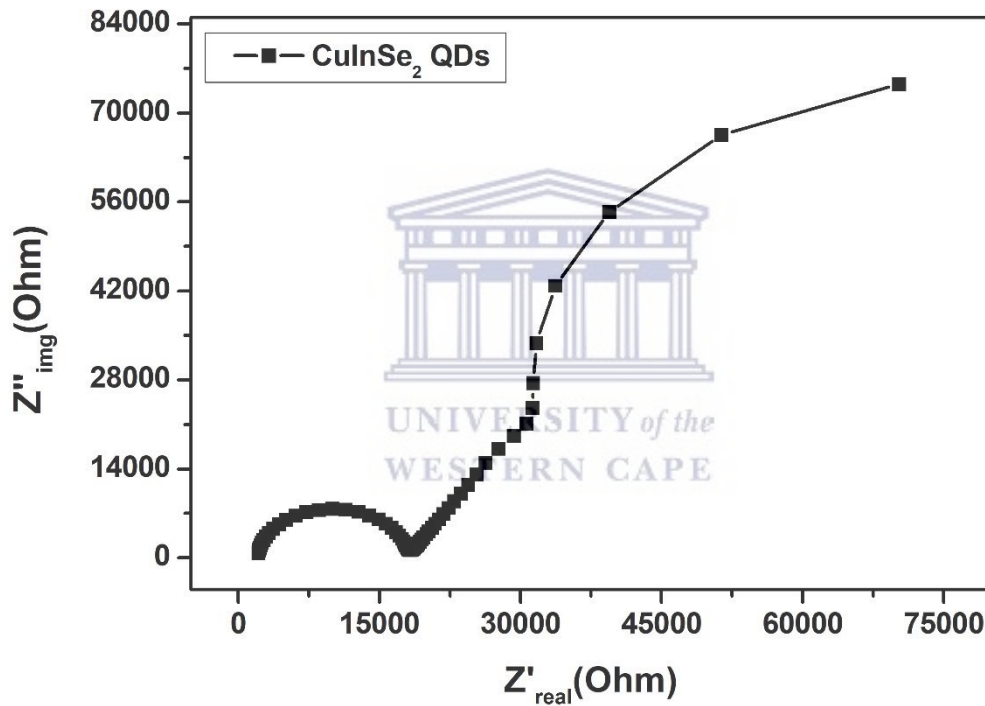
Figure 4.10: Nyquist plots for the G1PPT-CuInSe2 QDs obtained at a frequency range of 0.1 Hz – 100 kHz in 0.05 M TBAClO4/chloroform solution
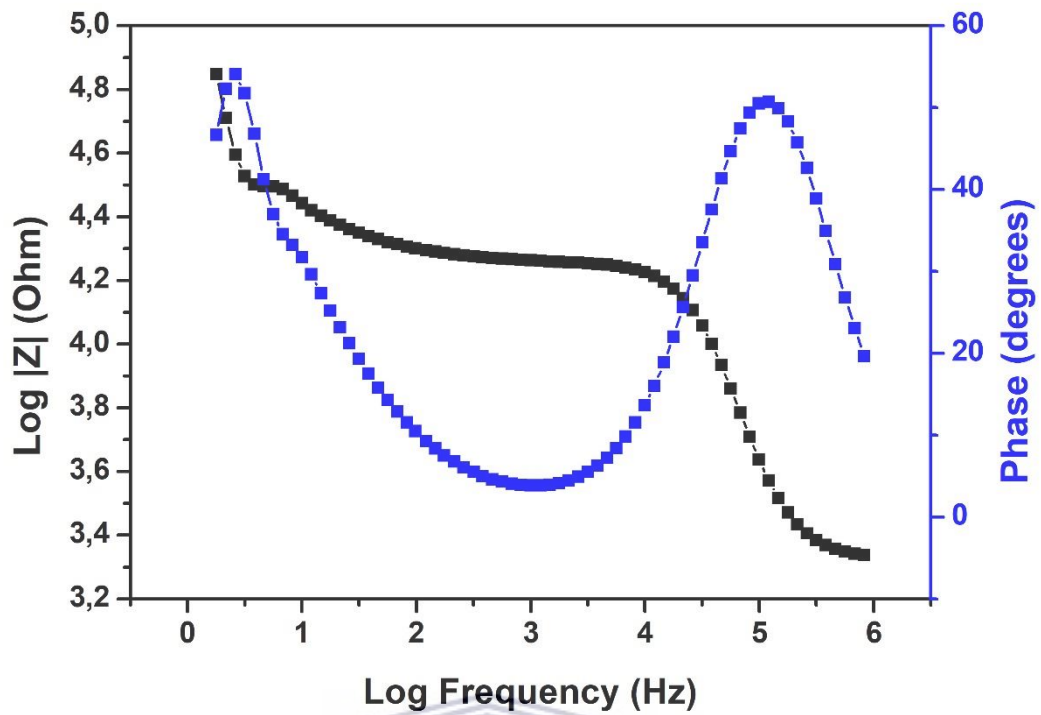
Figure 4.11: Bode plot for the G1PPT-CuInSe2 QDs obtained at a formal potential of 298 mV in 0.05 M TBAClO4/chloroform solution
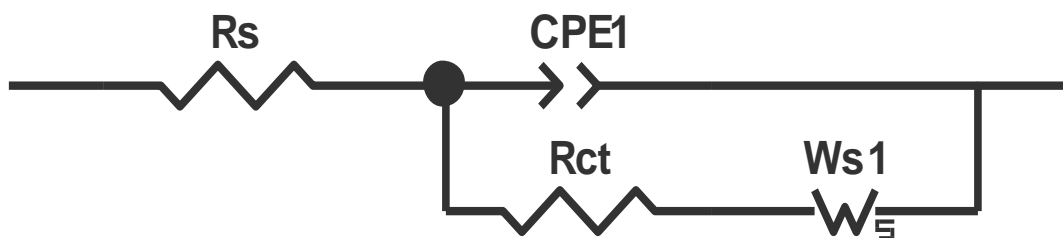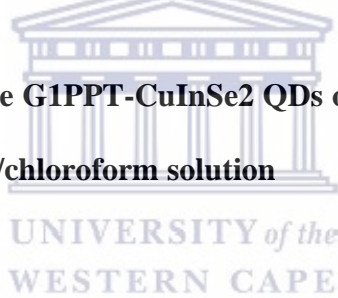
Figure 4.12: The Randles equivalent circuit model

In Figure 5.2 above, Rs represents the solution resistance to the flow of electrons, Rct, the charge transfer resistance formed by the kinetically controlled electrochemical reaction occurring at the surface of the G1PPT-CuInSe$_2$ QDs when in contact with the electrolyte. *CPE* is the constant phase element (double layer capacitance) generated by non-uniform current distributions when ions from the electrolyte solution adsorb onto the electrode surface and Ws is the Warburg impedance component arising from ion diffusion quotients [305].

The following kinetic parameters (Table 4.1) below were obtained from fitting the EIS plot of the G1PPT-CuInSe$_2$ QDs.

Table 4.1: Kinetic parameters obtained from the EIS Plot of G1PPT-CuInSe$_2$ QDs

Element	G1PPT-CuInSe$_2$ QDs	% Error
Rs (Ω)	2116	2.33
CPE1-T (μ F)	$\mathbf{3.35 \times 10^{-10}}$	13.4
CPE1-P	0.980	1.04
Rct (Ω)	15856	1.01
Ws-R (Ω.s$^{-1/2}$)	$\mathbf{1.04 \times 10^{5}}$	3.09
Ws-T (cm^2 s^{-1})	0.191	3.41

74

Ws-P	0.673	0.923

From the frequency at the maximum imaginary impedance of the semi-circle ω_{max} important kinetic parameters of the electron transfer process such as the time constant τ; the exchange current I_0 , which is a measure of the rate of charge exchange between the oxidized and reduced species at equilibrium potential with no net overall change; the heterogeneous rate constant of electron transfer (Ket) and the apparent or approximate diffusion coefficient (D_{app}) can be calculated according to the following equations:

$$\omega_{max} = \frac{1}{R_{ct}C_{dl}} \tag{10}$$

$$\tau = \frac{1}{\omega_{max}} \tag{11}$$

$$i_0 = \frac{RT}{nFR_{ct}} \tag{12}$$

$$K_{et} = \frac{i_0}{nFAC_0} \tag{13}$$

$$\sigma = (R_s + R_{ct})\omega^{\frac{1}{2}} \tag{14}$$

$$D_{app} = \frac{2RT^2}{(\sigma n^2 F^2 AC_0)^2} \tag{15}$$

Where: C_{dl} is the double layer capacitance (*CPE*); R is the molar gas constant = 8.314 J. mol^{-1}. k^{-1}; T is the room temperature = 293 K; n is the number of electrons exchanged; F is the

Faraday's constant = 96486 c.mol^{-1}; A is the area of the GCE = 0.071 cm^2 and C_0 is the concentration (mol cm^{-3}). The values obtained are presented in Table 4.2 below.

Table 4.2: Kinetic Parameters of G1PPT-CuInSe$_2$ QDs Obtained from EIS

Material	ω_{max} (rad s^{-1})	I_0 (A)	τ (s rad^{-1})	K_{et} (cm s^{-1})	σ (Ω S$^{-1/2}$)	D_{app} (cm^{2}S^{-1})
CuInSe$_2$ QDs	6.44×10^{-5}	1.59×10^{-6}	15538	4.64×10^{-9}	144	6.31×10^{-14}

From the tabulated results, no clear conclusion can be drawn about the overall performance of the material since literature studies on electrochemical impedance of semiconductor nanocrystals applied in solar cells are focused on the overall device performance instead of the material itself. The R_{ct} and τ were significantly high, which may indicate poor ionic conductivity. The heterogeneous rate constant is a measure of the rate of electron transfer at the surface of the electrode and its low value supports the previous assumption.

CHAPTER 5

CONCLUSION AND RECOMMENDATIONS

5.1   Conclusion

In the past few years, there has been immense interest in the preparation of cost-effective photovoltaic devices derived from nontoxic and highly efficient materials. Ternary semiconductor nanocrystals such $CuInSe_2$ have recently emerged at the forefront as suitable materials for the development of these next-generation photovoltaic devices. In the present study, $CuInSe_2$ QDs have been prepared using the hot injection method and capped with generation 1 poly (propylene imine) dendrimer which was previously modified by capping with thiophene to improve electronic properties and effective surface passivation. To the best of our knowledge, no similar approach has been done to improve the overall performance of the ternary $CuInSe_2$ quantum dots. The synthesis of G1PPT-$CuInSe_2$ QDs began with the functionalization of the capping material generation 1 poly(propyleneimine) tetramine dendrimer G1PPI into generation 1 poly(propylenethiopheneimine) G1PPT vai Schiff condensation in an inert environment. The Proton Nuclear Magnetic Resonance (^{1}H NMR) of G1PPT gave rise to a new chemical shift at 8.31 ppm for N=C-H, which confirmed the incorporation of 2-Thiophenecarboxaldehyde into the G1-PPI dendrimer structure and Fourier transform infrared spectroscopy (FT-IR) showed that strong bands appeared at 1673 cm^{-1} for N=C in the dendrimer moiety, and 755 cm^{-1} for C-H at α-position of the thiophene ring. Uv-vis spectroscopy showed two distinct absorption peaks for the at 241 nm and 304 nm, characteristic to the absorbance of the two chromophores C=N and C-S-C respectively present in the dendrimer moiety. Powder x-ray diffraction (XRD) showed that G1PPT has

an amorphous morphology and therefore no measurable X-ray patterns or does not display any crystallinity as was expected. Cyclic voltammetry revealed no electrochemical activity, a feature that makes the prepared G1PPT suitable as ligand for QDs for reasons discussed in section 4.3.3.1.

The optical properties of the G1PPT-CuInSe$_2$ QDs were studied with Uv-vis spectroscopy. The absorption spectrum showed a disappearance of the peak at 306 nm belonging to C-S-C, indicating the effective passivation of the G1PPT on the surface of the nanocrystals, and FT-IR further confirmed this with the S-H vibration at 2572 cm^{-1} for 1-dodecanethiol and the C-S bending vibration and C-S-C ring deformation stretching at 891 cm^{-1} and at 661 cm^{-1} for G1PPT were absent in CuInSe$_2$ sample, suggesting the formation of metal–sulfide bonds. The Tauc plot extrapolation allowed for the determination of the bandgap at 1,51 eV, a value close to the values reported for typical CuInSe$_2$ QDs of size 7-9 nm. Aliquots taken during synthesis showed a gradual shift towards longer wavelengths and no apparent excitonic peak, similar to previous reports. HR-TEM was used for morphological studies and size determination. The EDS spectrum confirmed the presence of all the relevant elements and the crystallinity was evidenced by the continuous lattice fringes and very clear crystal facets on the TEM images and SAED. The average size of the as-prepared G1PPT-CISe QDs determined from TEM is 8,5 nm. Powder x-ray diffraction revealed Bragg's reflections for CuInSe$_2$ QDs are observed in XRD pattern at 2θ value of 27,71°, 46,39°, 54,63° representing (111), (220) and (311) planes of the zincblende metastable structure of CuInSe$_2$ and the crystal diameter was estimated by Debye–Scherrer equation (d = 0.9 k/b cosh) which was found to be about 6,3 nm, which is less than the average size determined from TEM as is always the expected case. Raman spectroscopy was employed for further phase purity and crystal structure studies and the vibration of the Se in the x–y plane with

the cations at rest (A1 mode) peak appeared at 169 cm^{-1}, while the B2 and E vibration mode of CuInSe$_2$ chalcopyrite were attributed at 212 cm^{-1} and 225 cm^{-1}. Hence, the main phase of the G1PPT-CISe dots synthesized in this study is CuInSe$_2$. Small-angle X-ray scattering (SAXS) was further used to study the shape and size distribution of the as-prepared G1PPT-CuInSe$_2$ QDs. The PDDF curve suggested the particles have a lamellar shape and the particle size distribution determined by the Fourie indirect method yielded two distinct populations with an average particle diameter of 6.9 nm and 35 nm respectively. From the ratio of the areas under the two main peaks in the size distribution curve, the volume ratio ϕv,1/ϕv,2 could be estimated to be 4.3. From the particle size intensity curve, the bigger sized particles showed a high intensity due to biased interaction with the x-rays caused by their big sizes. Particle size distribution by number also showed the already expected results, population 1 had a high number of particles with an average diameter of 6.95 nm.
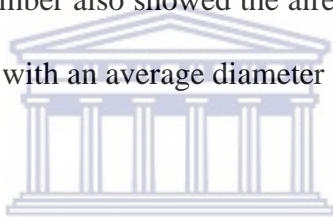
Lastly, electrochemical studies were done using cyclic voltammetry (CV) and electrochemical impedance spectroscopy (EIS). CV revealed no apparent proportionality between scan rate, potential, and current. Cyclic voltammetry revealed two oxidation peaks with potential values of 0.122 V and 0.809 V and were proposed to due to the oxidation of selenium rich/Se-rich phase phases of CuInSe$_2$. The reduction potentials for Cu and Se appeared at -0.228 V and -0.497 V respectively. A peak assigned to the In-rich phased of CuInSe$_2$ was determined at -0.976 V. The HOMO and LUMO levels were calculated from the onset redox potentials 0.740 V and -0.863 and were found to be -5.140 eV and -3.537 eV, respectively. The electrochemical bandgap calculated from the previous values is 1.60 eV, which is slightly higher than the calculated optical bandgap (1.51 eV). From these values, the electron-hole Coulomb interaction energy $J_{e,h}$ found to be 90 meV and is

comparable to the reported value of 80 meV for typical CISe QDs. A well-defined semicircle with a radius of 10015 Ω was observed from the Nyquist plot, while the Bode plot revealed a higher impedance to electron transfer as demonstrated by the impedance and phase angle values at low frequencies where the disturbances to the equilibrium position of the system are at minimal. All the important parameters were calculated from the fitted results and resulting in the Randles equivalent circuit.

The results obtained in this study suggest that G1PPT-CuInSe$_2$ QDs are suitable for solar cell application, owing to its clear superior optical and electronic properties and as well as complete solubility in the electrolyte to allow native electrochemical probing.

5.2   Recommendations
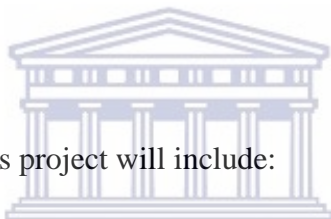
Future work with respect to this project will include:

- A comparative study of the G1PPT capped- and uncapped CuInSe$_2$ QDs in order to map out the effects and/or improvements of incorporating G1PPT into CuInSe$_2$

- Device fabrication for both the G1PPT capped- and non-capped CuInSe$_2$ QDs

- Investigation of the power conversion efficiency improvement

REFERENCES

[1] C. Xiao, Z. Li, K. Li, P. Huang, and Y. Xie, "Decoupling Interrelated Parameters for Designing High Performance Thermoelectric Materials," *Acc. Chem. Res.*, vol. 47, no. 4, pp. 1287–1295, Apr. 2014.

[2] D. Acemoglu, U. Akcigit, D. Hanley, and W. Kerr, "Transition to Clean Technology," *J. Polit. Econ.*, vol. 124, no. 1, pp. 52–104, Feb. 2016.

[3] M. L. Weitzman, "Book Review--A Review of William Nordhaus' The Climate Casino: Risk, Uncertainty, and Economics for a Warming World," *Rev. Environ. Econ. Policy*, vol. 9, no. 1, pp. 145–156, Jan. 2015.

[4] B. Obama, "The irreversible momentum of clean energy," *Science (80-.).*, vol. 355, no. 6321, pp. 126–129, Jan. 2017.

[5] J. Butler *et al.*, "The NOAA Annual Greenhouse Gas Index (AGGI)," 1950.

[6] D. Roemmich, J. Church, J. Gilson, D. Monselesan, P. Sutton, and S. Wijffels, "Unabated planetary warming and its ocean structure since 2006," *Nat. Clim. Chang.*, vol. 5, no. 3, pp. 240–245, Mar. 2015.

[7] P. V. Kamat*, "Meeting the Clean Energy Demand: Nanostructure Architectures for Solar Energy Conversion," 2007.

[8] Y. Jiang *et al.*, "ITO@Cu $_2$ S Tunnel Junction Nanowire Arrays as Efficient Counter Electrode for Quantum-Dot-Sensitized Solar Cells," *Nano Lett.*, vol. 14, no. 1, pp. 365–372, Jan. 2014.
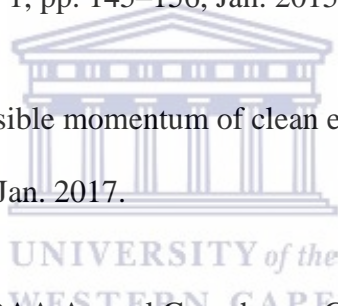
[9]   A. V Herzog, T. E. Lipman, and D. M. Kammen, "RENEWABLE ENERGY SOURCES."

[10]   N. L. Panwar, S. C. Kaushik, and S. Kothari, "Role of renewable energy sources in environmental protection: A review," *Renew. Sustain. Energy Rev.*, vol. 15, no. 3, pp. 1513–1524, Apr. 2011.

[11]   S. Bond, N. Holmes, and B. Norton, "Using Photovoltaics to Power Electrochemical Chloride Extraction from Concrete."

[12]   M. Pierre Kalenga, "SYNTHESIS AND CHARACTERIZATION OF COPPER CHALCOGENIDE NANOPARTICLES AND THEIR USE IN SOLUTION PROCESSED PHOTOVOLTAICS," 2015.

[13]   P. C. Choubey, A. Oudhia, and R. Dewangan, *Recent research in science and technology : an international refereed journal for all aspects of science research.*, vol. 4, no. 8. Recent Research in Science and Technology, 2009.

[14]   X. Wang *et al.*, "Tandem colloidal quantum dot solar cells employing a graded recombination layer," *Nat. Photonics*, vol. 5, no. 8, pp. 480–484, Aug. 2011.

[15]   M. Hong *et al.*, "Air-exposing microwave-assisted synthesis of CuInS $_2$ /ZnS quantum dots for silicon solar cells with enhanced photovoltaic performance," *RSC Adv.*, vol. 5, no. 124, pp. 102682–102688, 2015.

[16]   H. K. Jun, M. A. Careem, and A. K. Arof, "Quantum dot-sensitized solar cells— perspective and recent developments: A review of Cd chalcogenide quantum dots as

sensitizers," *Renew. Sustain. Energy Rev.*, vol. 22, pp. 148–167, Jun. 2013.

[17]   M. A. Hossain, J. R. Jennings, N. Mathews, and Q. Wang, "Band engineered ternary
        solid solution CdS x Se 1Àx-sensitized mesoscopic TiO 2 solar cellsw," *Phys.
        Chem. Chem. Phys*, vol. 14, pp. 7154–7161, 2012.

[18]   R. Zhou *et al.*, "Tailoring band structure of ternary CdSxSe1−x quantum dots for
        highly efficient sensitized solar cells," *Sol. Energy Mater. Sol. Cells*, vol. 155, pp.
        20–29, Oct. 2016.

[19]   T. Omata, K. Nose, and S. Otsuka-Yao-Matsuo, "Size dependent optical band gap of
        ternary I-III-VI2 semiconductor nanocrystals," *J. Appl. Phys.*, vol. 105, no. 7, p.
        073106, Apr. 2009.

[20]   G. Halder and S. Bhattacharyya, "Zinc-diffused silver indium selenide quantum dot
        sensitized solar cells with enhanced photoconversion efficiency," *J. Mater. Chem.
        A*, vol. 5, no. 23, pp. 11746–11755, Jun. 2017.

[21]   R. Soltani *et al.*, "Light harvesting enhancement upon incorporating alloy structured
        CdSe x Te 1−x quantum dots in DPP:PC 61 BM bulk heterojunction solar cells," *J.
        Mater. Chem. C*, vol. 5, no. 3, pp. 654–662, 2017.

[22]   S. Liu and X. Su, "The synthesis and application of I–III–VI type quantum dots,"
        RSC Adv., vol. 4, no. 82, pp. 43415–43428, Aug. 2014.

[23]   M. E. Norako, M. A. Franzman, and R. L. Brutchey, "Growth Kinetics of
        Monodisperse Cu−In−S Nanocrystals Using a Dialkyl Disulfide Sulfur Source,"
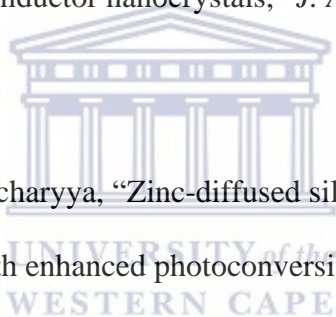
Chem. Mater., vol. 21, no. 18, pp. 4299–4304, Sep. 2009.

[24]   P. K. Santra *et al.*, "CuInS 2 -Sensitized Quantum Dot Solar Cell. Electrophoretic
       Deposition, Excited-State Dynamics, and Photovoltaic Performance," *J. Phys.*
       Chem. Lett., vol. 4, no. 5, pp. 722–729, 2013.

[25]   J. Park and S.-W. Kim, "CuInS2/ZnS core/shell quantum dots by cation exchange
       and their blue-shifted photoluminescence," *J. Mater. Chem.*, vol. 21, no. 11, p.
       3745, 2011.

[26]   D. P. Dutta and G. Sharma, "A facile route to the synthesis of CuInS2
       nanoparticles," *Mater. Lett.*, vol. 60, no. 19, pp. 2395–2398, Aug. 2006.

[27]   S. K. Batabyal, L. Tian, N. Venkatram, W. Ji, and J. J. Vittal, "Phase-Selective
       Synthesis of CuInS 2 Nanocrystals," *J. Phys. Chem. C*, vol. 113, no. 33, pp. 15037–
       15042, Aug. 2009.

[28]   A. L. Abdelhady, M. A. Malik, and P. O'Brien, "iso-Propylthiobiuret-copper and
       indium complexes as novel precursors for colloidal synthesis of CuInS2
       nanoparticles," *J. Mater. Chem.*, vol. 22, no. 9, p. 3781, 2012.

[29]   Y. Chen, S. Li, L. Huang, and D. Pan, "Green and Facile Synthesis of Water-
       Soluble Cu–In–S/ZnS Core/Shell Quantum Dots," *Inorg. Chem.*, vol. 52, no. 14, pp.
       7819–7821, Jul. 2013.

[30]   W.-W. Xiong, G.-H. Yang, X.-C. Wu, and J.-J. Zhu, "Aqueous Synthesis of Color-
       Tunable CuInS 2 /ZnS Nanocrystals for the Detection of Human Interleukin 6," *ACS*
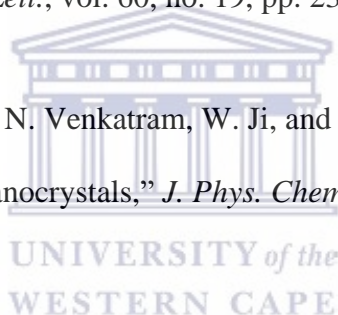
Appl. Mater. Interfaces, vol. 5, no. 16, pp. 8210–8216, Aug. 2013.

[31] M. Yousefi, M. Sabet, M. Salavati-Niasari, and S. M. Hosseinpour-Mashkani, "Facile Microwave Approach for Synthesis of Copper–Indium Sulfide Nanoparticles and Study of Their Behavior in Solar Cell," *J. Clust. Sci.*, vol. 23, no. 2, pp. 491–502, Jun. 2012.

[32] S. M. Hosseinpour-Mashkani, M. Salavati-Niasari, F. Mohandes, and K. Venkateswara-Rao, "CuInS2 nanoparticles: Microwave-assisted synthesis, characterization, and photovoltaic measurements," *Mater. Sci. Semicond. Process.*, vol. 16, no. 2, pp. 390–402, Apr. 2013.

[33] P. V. Kamat, "Quantum Dot Solar Cells. Semiconductor Nanocrystals as Light Harvesters," *J. Phys. Chem. C*, vol. 112, no. 48, pp. 18737–18753, Dec. 2008.

[34] N. M. Gabor *et al.*, "Extremely efficient multiple electron-hole pair generation in carbon nanotube photodiodes.," *Science*, vol. 325, no. 5946, pp. 1367–71, Sep. 2009.

[35] H. Lee *et al.*, "Efficient CdSe Quantum Dot-Sensitized Solar Cells Prepared by an Improved Successive Ionic Layer Adsorption and Reaction Process," *Nano Lett.*, vol. 9, no. 12, pp. 4221–4227, Dec. 2009.

[36] W. Ma, J. M. Luther, H. Zheng, Y. Wu, and A. P. Alivisatos, "Photovoltaic Devices Employing Ternary PbS$_x$ Se$_{1-x}$ Nanocrystals," *Nano Lett.*, vol. 9, no. 4, pp. 1699–1703, Apr. 2009.

[37] P. K. Santra and P. V. Kamat, "Mn-Doped Quantum Dot Sensitized Solar Cells: A Strategy to Boost Efficiency over 5%," *J. Am. Chem. Soc.*, vol. 134, no. 5, pp. 2508–2511, Feb. 2012.

[38] H. Zhang *et al.*, "Efficient CdSe quantum dot-sensitized solar cells prepared by a postsynthesis assembly approach," *Chem. Commun.*, vol. 48, no. 91, p. 11235, 2012.

[39] *PUBLICATION NOT FOR SALE REPORT R111/2014 SOUTH AFRICA'S COAL INDUSTRY OVERVIEW, 2014 DIRECTORATE MINERAL ECONOMICS Richards Bay Coal Terminal.* .

[40] D. Aldakov, A. Lefrançois, and P. Reiss, "Ternary and quaternary metal chalcogenide nanocrystals: synthesis, properties and applications," *J. Mater. Chem. C*, vol. 1, no. 24, p. 3756, May 2013.

[41] R. J. B. Balaguru, "Quantum size effect , electrical conductivity and Quantum transport School of Electrical & Electronics Engineering."

[42] † Sameer Sapra, *,† D. D. Sarma, ‡,§ and S. Sanvito, and N. A. Hill‡, "Influence of Quantum Confinement on the Electronic and Magnetic Properties of (Ga,Mn)As Diluted Magnetic Semiconductor," 2002.

[43] P. Jorge *et al.*, "Optical Fiber Sensing Using Quantum Dots," *Sensors*, vol. 7, no. 12, pp. 3489–3534, Dec. 2007.

[44] Y. L. Lee and Y. S. Lo, "Highly efficient quantum-dot-sensitized solar cell based on co-sensitization of CdS/CdSe," *Adv. Funct. Mater.*, vol. 19, no. 4, pp. 604–609, Feb.

2009.

[45] F. Huang *et al.*, "High Efficiency CdS/CdSe Quantum Dot Sensitized Solar Cells with Two ZnSe Layers," *ACS Appl. Mater. Interfaces*, vol. 8, no. 50, pp. 34482–34489, Dec. 2016.

[46] Z. Zhang *et al.*, "Significant Improvement in the Performance of PbSe Quantum Dot Solar Cell by Introducing a CsPbBr3 Perovskite Colloidal Nanocrystal Back Layer," *Adv. Energy Mater.*, vol. 7, no. 5, p. 1601773, Mar. 2017.

[47] S. Niki *et al.*, "CIGS absorbers and processes," *Prog. Photovoltaics Res. Appl.*, vol. 18, no. 6, pp. 453–466, Sep. 2010.

[48] Z. Pan *et al.*, "High-Efficiency 'Green' Quantum Dot Solar Cells," *J. Am. Chem. Soc.*, vol. 136, no. 25, pp. 9203–9210, Jun. 2014.

[49] E. Witt and J. Kolny-Olesiak, "Recent developments in colloidal synthesis of CuInSe2 nanoparticles," *Chem. - A Eur. J.*, vol. 19, no. 30, pp. 9746–9753, Jul. 2013.

[50] H. Cotal *et al.*, "III-V multijunction solar cells for concentrating photovoltaics," *Energy Environ. Sci.*, vol. 2, no. 2, pp. 174–192, Jan. 2009.

[51] P. Rudolph, "Non-stoichiometry related defects at the melt growth of semiconductor compound crystals – a review," *Cryst. Res. Technol.*, vol. 38, no. 78, pp. 542–554, Jul. 2003.

[52] P. M. Allen and M. G. Bawendi, "Ternary I−III−VI Quantum Dots Luminescent in
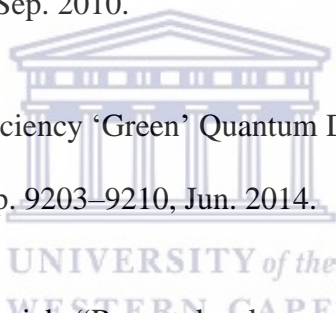
the Red to Near-Infrared," *J. Am. Chem. Soc.*, vol. 130, no. 29, pp. 9240–9241, Jul. 2008.

[53]   S. P. Hong, H. K. Park, J. H. Oh, H. Yang, and Y. R. Do, "Comparisons of the structural and optical properties of o-AgInS2, t-AgInS2, and c-AgIn5S8 nanocrystals and their solid-solution nanocrystals with ZnS," *J. Mater. Chem.*, vol. 22, no. 36, p. 18939, Aug. 2012.

[54]   B. Chen *et al.*, "Highly Emissive and Color-Tunable CuInS2-Based Colloidal Semiconductor Nanocrystals: Off-Stoichiometry Effects and Improved Electroluminescence Performance," *Adv. Funct. Mater.*, vol. 22, no. 10, pp. 2081–2088, May 2012.

[55]   M. Ko, H. C. Yoon, H. Yoo, J. H. Oh, H. Yang, and Y. R. Do, "Highly Efficient Green Zn☐Ag☐In☐S/Zn☐In☐S/ZnS QDs by a Strong Exothermic Reaction for Down-Converted Green and Tripackage White LEDs," *Adv. Funct. Mater.*, vol. 27, no. 4, p. 1602638, Jan. 2017.

[56]   E.-P. Jang, W.-S. Song, K.-H. Lee, and H. Yang, "Preparation of a photo-degradation- resistant quantum dot–polymer composite plate for use in the fabrication of a high-stability white-light-emitting diode," *Nanotechnology*, vol. 24, no. 4, p. 045607, Feb. 2013.

[57]   O. Yarema *et al.*, "Highly Luminescent, Size- and Shape-Tunable Copper Indium Selenide Based Colloidal Nanocrystals," *Chem. Mater.*, vol. 25, no. 18, pp. 3753–3757, Sep. 2013.
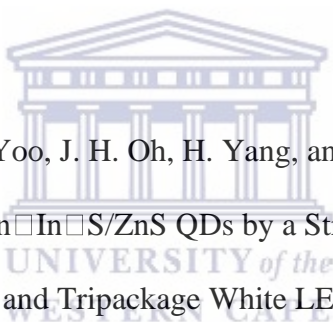
[58] O. Yarema, M. Yarema, D. Bozyigit, W. M. M. Lin, and V. Wood, "Independent Composition and Size Control for Highly Luminescent Indium-Rich Silver Indium Selenide Nanocrystals," *ACS Nano*, vol. 9, no. 11, pp. 11134–11142, Nov. 2015.

[59] S. Lany and A. Zunger, "Anion vacancies as a source of persistent photoconductivity in II-VI and chalcopyrite semiconductors," *Phys. Rev. B - Condens. Matter Mater. Phys.*, vol. 72, no. 3, p. 035215, Jul. 2005.

[60] J. Parkes, R. D. Tomlinson, and M. J. Hampshire, "The fabrication of p and n type single crystals of CuInSe2," *J. Cryst. Growth*, vol. 20, no. 4, pp. 315–318, Nov. 1973.

[61] L. L. Kazmerski and G. A. Sanborn, "CuInS $_2$ thin-film homojunction solar cells," *J. Appl. Phys.*, vol. 48, no. 7, pp. 3178–3180, Jul. 1977.

[62] R. G. Pearson, "PHYSICAL AND INORGANIC CHEMISTRY Hard and Soft Acids and Bases," UTC, 2018.

[63] R. G. Parr and R. . Pearson, ""Hardness companion parameter to absolute electronegavity," 1983.

[64] C. Coughlan, M. Ibáñez, O. Dobrozhan, A. Singh, A. Cabot, and K. M. Ryan, "Compound copper chalcogenide nanocrystals," *Chem. Rev.*, vol. 117, no. 9, pp. 5865–6109, May 2017.

[65] O. Yarema, M. Yarema, and V. Wood, "Tuning the Composition of Multicomponent Semiconductor Nanocrystals: The Case of I–III–VI Materials,"

Chem. Mater., vol. 30, no. 5, pp. 1446–1461, Mar. 2018.

[66] R. Xie, M. Rutherford, and X. Peng, "Formation of High-Quality I−III−VI Semiconductor Nanocrystals by Tuning Relative Reactivity of Cationic Precursors," *J. Am. Chem. Soc.*, vol. 131, no. 15, pp. 5691–5697, Apr. 2009.

[67] M. Kruszynska, H. Borchert, J. Parisi, and J. Kolny-Olesiak, "Synthesis and Shape Control of CuInS $_2$ Nanoparticles," *J. Am. Chem. Soc.*, vol. 132, no. 45, pp. 15976–15986, Nov. 2010.

[68] L. Liu *et al.*, "Optimizing the synthesis of red- and near-infrared CuInS2 and AgInS2 semiconductor nanocrystals for bioimaging," *Analyst*, vol. 138, no. 20, p. 6144, Sep. 2013.

[69] H. C. Yoon, J. H. Oh, M. Ko, H. Yoo, and Y. R. Do, "Synthesis and Characterization of Green Zn–Ag–In–S and Red Zn–Cu–In–S Quantum Dots for Ultrahigh Color Quality of Down-Converted White LEDs," *ACS Appl. Mater. Interfaces*, vol. 7, no. 13, pp. 7342–7350, Apr. 2015.

[70] H. Zhong *et al.*, "Noninjection Gram-Scale Synthesis of Monodisperse Pyramidal CuInS $_2$ Nanocrystals and Their Size-Dependent Properties," *ACS Nano*, vol. 4, no. 9, pp. 5253–5262, Sep. 2010.

[71] D. H. Jara, K. G. Stamplecoskie, and P. V. Kamat, "Two Distinct Transitions in Cu $_x$ InS $_2$ Quantum Dots. Bandgap versus Sub-Bandgap Excitations in Copper-Deficient Structures," *J. Phys. Chem. Lett.*, vol. 7, no. 8, pp. 1452–1459, Apr. 2016.
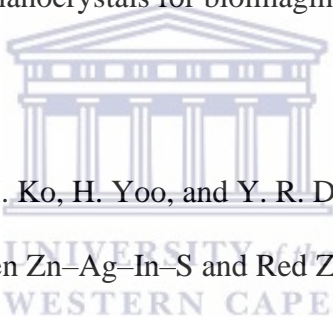
[72]   L. Li, T. J. Daou, I. Texier, T. T. Kim Chi, N. Q. Liem, and P. Reiss, "Highly

        Luminescent CuInS $_2$ /ZnS Core/Shell Nanocrystals: Cadmium-Free Quantum Dots

        for In Vivo Imaging," *Chem. Mater.*, vol. 21, no. 12, pp. 2422–2429, Jun. 2009.

[73]   H. Zhong *et al.*, "Controlled Synthesis and Optical Properties of Colloidal Ternary

        Chalcogenide CuInS $_2$ Nanocrystals," *Chem. Mater.*, vol. 20, no. 20, pp. 6434–6443,

        Oct. 2008.

[74]   E. Cassette *et al.*, "Synthesis and Characterization of Near-Infrared Cu−In−Se/ZnS

        Core/Shell Quantum Dots for In vivo Imaging," *Chem. Mater.*, vol. 22, no. 22, pp.

        6117–6124, Nov. 2010.

[75]   M.-A. Langevin, A. M. Ritcey, and C. N. Allen, "Air-Stable Near-Infrared AgInSe $_2$

        Nanocrystals," *ACS Nano*, vol. 8, no. 4, pp. 3476–3482, Apr. 2014.

[76]   *,† Stephanie L. Castro, ‡ Sheila G. Bailey, § Ryne P. Raffaelle, † and Kulbinder K.

        Banger, and A. F. Hepp‡, "Nanocrystalline Chalcopyrite Materials (CuInS2 and

        CuInSe2) via Low-Temperature Pyrolysis of Molecular Single-Source Precursors,"

        2003.

[77]   T. Uematsu, T. Doi, T. Torimoto, and S. Kuwabata, "Preparation of Luminescent

        AgInS $_2$ −AgGaS $_2$ Solid Solution Nanoparticles and Their Optical Properties," *J.

        Phys. Chem. Lett.*, vol. 1, no. 22, pp. 3283–3287, Nov. 2010.

[78]   Q. Guo *et al.*, "Development of CuInSe $_2$ Nanocrystal and Nanoring Inks for Low-

        Cost Solar Cells," *Nano Lett.*, vol. 8, no. 9, pp. 2982–2987, Sep. 2008.
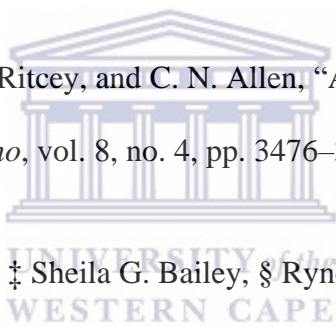
[79]   M. G. Panthani *et al.*, "Synthesis of CuInS $_2$, CuInSe $_2$, and Cu(In $_x$ Ga $_{1-x}$)Se $_2$ (CIGS) Nanocrystal 'Inks' for Printable Photovoltaics," *J. Am. Chem. Soc.*, vol. 130, no. 49, pp. 16770–16777, Dec. 2008.

[80]   J. Tang, S. Hinds, S. O. Kelley, and E. H. Sargent, "Synthesis of Colloidal CuGaSe $_2$, CuInSe $_2$, and Cu(InGa)Se $_2$ Nanoparticles," *Chem. Mater.*, vol. 20, no. 22, pp. 6906–6910, Nov. 2008.

[81]   M. G. Panthani *et al.*, "CuInSe $_2$ Quantum Dot Solar Cells with High Open-Circuit Voltage," *J. Phys. Chem. Lett.*, vol. 4, no. 12, pp. 2030–2034, Jun. 2013.

[82]   O. Yarema *et al.*, "Highly Luminescent, Size- and Shape-Tunable Copper Indium Selenide Based Colloidal Nanocrystals," *Chem. Mater.*, vol. 25, no. 18, pp. 3753–3757, Sep. 2013.

[83]   O. Yarema, M. Yarema, D. Bozyigit, W. M. M. Lin, and V. Wood, "Independent Composition and Size Control for Highly Luminescent Indium-Rich Silver Indium Selenide Nanocrystals," *ACS Nano*, vol. 9, no. 11, pp. 11134–11142, Nov. 2015.

[84]   O. Yarema, M. Yarema, W. M. M. Lin, and V. Wood, "Cu–In–Te and Ag–In–Te colloidal nanocrystals with tunable composition and size," *Chem. Commun.*, vol. 52, no. 72, pp. 10878–10881, Aug. 2016.

[85]   P. M. Allen and M. G. Bawendi, "Ternary I−III−VI Quantum Dots Luminescent in the Red to Near-Infrared," *J. Am. Chem. Soc.*, vol. 130, no. 29, pp. 9240–9241, Jul. 2008.
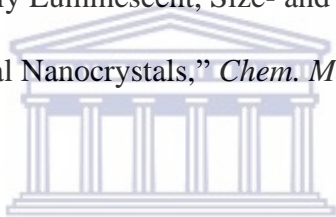
[86] J. Park *et al.*, "CuInSe/ZnS core/shell NIR quantum dots for biomedical imaging," *Small*, vol. 7, no. 22, pp. 3148–3152, Nov. 2011.

[87] Jonathan S. Steckel, Brian K. H. Yen, and David C. Oertel, and M. G. Bawendi*, "On the Mechanism of Lead Chalcogenide Nanocrystal Formation," 2006.

[88] K. E. Knowles *et al.*, "Luminescent Colloidal Semiconductor Nanocrystals Containing Copper: Synthesis, Photophysics, and Applications," *Chem. Rev.*, vol. 116, no. 18, pp. 10820–10851, Sep. 2016.

[89] Q. A. Akkerman *et al.*, "From Binary Cu_2S to Ternary Cu–In–S and Quaternary Cu–In–Zn–S Nanocrystals with Tunable Composition *via* Partial Cation Exchange," *ACS Nano*, vol. 9, no. 1, pp. 521–531, Jan. 2015.

[90] P. Reiss, M. Carrière, C. Lincheneau, L. Vaure, and S. Tamang, "Synthesis of Semiconductor Nanocrystals, Focusing on Nontoxic and Earth-Abundant Materials," *Chem. Rev.*, vol. 116, no. 18, pp. 10731–10819, Sep. 2016.

[91] Y. Vahidshad, R. Ghasemzadeh, A. Irajizad, S. M. Mirkazemi, and C. Solvent, "Synthesis and Characterization of Copper Indium Sulfide Chalcopyrite Structure with Hot Injection Method," *J. Nanostructures*, vol. 3, no. 2, pp. 145–154, Jun. 2013.

[92] Y. Yuan, F.-S. Riehle, H. Gu, R. Thomann, G. Urban, and M. Krüger, "Critical Parameters for the Scale-Up Synthesis of Quantum Dots," *J. Nanosci. Nanotechnol.*, vol. 10, no. 9, pp. 6041–6045, Sep. 2010.

[93] B. G. Rao, D. Mukherjee, and B. M. Reddy, "Novel approaches for preparation of nanoparticles," *Nanostructures Nov. Ther.*, pp. 1–36, Jan. 2017.

[94] Y. Jia *et al.*, "A facile method for the synthesis of CuInS $_2$ –ZnS quantum dots with tunable photoluminescent properties," *RSC Adv.*, vol. 6, no. 96, pp. 93303–93308, Sep. 2016.

[95] Sang-Hyun Choi, and Eung-Gyu Kim, and T. Hyeon*, "One-Pot Synthesis of Copper−Indium Sulfide Nanocrystal Heterostructures with Acorn, Bottle, and Larva Shapes," 2006.

[96] J. Park and S.-W. Kim, "CuInS2/ZnS core/shell quantum dots by cation exchange and their blue-shifted photoluminescence," *J. Mater. Chem.*, vol. 21, no. 11, p. 3745, Mar. 2011.

[97] N. T. M. Thuy, T. T. K. Chi, U. T. D. Thuy, and N. Q. Liem, "Low-cost and large-scale synthesis of CuInS2 and CuInS2/ZnS quantum dots in diesel," *Opt. Mater. (Amst).*, vol. 37, pp. 823–827, Nov. 2014.

[98] M. D. Regulacio, C. Ye, S. H. Lim, Y. Zheng, Q.-H. Xu, and M.-Y. Han, "Facile noninjection synthesis and photocatalytic properties of wurtzite-phase CuGaS2 nanocrystals with elongated morphologies," *CrystEngComm*, vol. 15, no. 26, p. 5214, 2013.

[99] N. Gacem and P. Diao, "Effect of solvent polarity on the assembly behavior of PVP coated rhodium nanoparticles," *Colloids Surfaces A Physicochem. Eng. Asp.*, vol. 417, pp. 32–38, Jan. 2013.
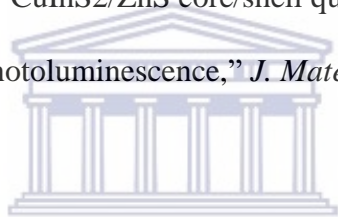
[100] † Xinhua Zhong, *,†,‡ Mingyong Han, § Zhili Dong, § and Timothy J. White, and † Wolfgang Knoll*, "Composition-Tunable ZnxCd1-xSe Nanocrystals with High Luminescence and Stability," 2003.

[101] B.-B. Xie, B.-B. Hu, L.-F. Jiang, G. Li, and Z.-L. Du, "The phase transformation of CuInS2 from chalcopyrite to wurtzite," *Nanoscale Res. Lett.*, vol. 10, no. 1, p. 86, Dec. 2015.

[102] Y. Zheng, B. Sadeghimakki, N. M. S. Jahed, and S. Sivoththaman, "Scalable Non-injection Synthesis of Cd-Free Copper Indium Sulfide/Zinc Sulfide Quantum Dots for Third-Gen Photovoltaic Application," *MRS Adv.*, vol. 1, no. 30, pp. 2193–2198, Jul. 2016.

[103] Y. su Kim *et al.*, "Synthesis of efficient near-infrared-emitting $CuInS_2$ /ZnS quantum dots by inhibiting cation-exchange for bio application," *RSC Adv.*, vol. 7, no. 18, pp. 10675–10682, Feb. 2017.

[104] H. Chen, Y.-M. Yeh, C. H. Liao, J. Z. Chen, and C. Wang, "Removal of CuS phases from electrodeposited CuInS2 films," *Ceram. Int.*, vol. 40, no. 1, pp. 67–72, Jan. 2014.

[105] L. Liu *et al.*, "Optimizing the synthesis of red- and near-infrared CuInS2 and AgInS2 semiconductor nanocrystals for bioimaging," *Analyst*, vol. 138, no. 20, p. 6144, Sep. 2013.

[106] D. Koziej *et al.*, "Interplay between size and crystal structure of molybdenum dioxide nanoparticlesâ-synthesis, growth mechanism, and electrochemical

performance," *Small*, vol. 7, no. 3, pp. 377–387, Feb. 2011.

[107] I. Olliges-Stadler *et al.*, "Study of the chemical mechanism involved in the
formation of tungstite in benzyl alcohol by the advanced QEXAFS technique,"
Chem. - A Eur. J., vol. 18, no. 8, pp. 2305–2312, Feb. 2012.

[108] B. Ludi, M. J. Süess, I. A. Werner, and M. Niederberger, "Mechanistic aspects of
molecular formation and crystallization of zinc oxide nanoparticles in benzyl
alcohol," *Nanoscale*, vol. 4, no. 6, pp. 1982–1995, Mar. 2012.

[109] D. Carriazo, M. D. Rossell, G. Zeng, I. Bilecka, R. Erni, and M. Niederberger,
"Formation mechanism of LiFePO4sticks grown by a microwave-assisted liquid-
phase process," *Small*, vol. 8, no. 14, pp. 2231–2238, Jul. 2012.

[110] A. Cho *et al.*, "The growth of Cu2 - xSe thin films using nanoparticles," *Thin Solid
Films*, vol. 546, pp. 299–307, Nov. 2013.

[111] L. Gou and C. J. Murphy, "Controlling the size of Cu2O nanocubes from 200 to 25
nm," *J. Mater. Chem.*, vol. 14, no. 4, pp. 735–738, Feb. 2004.

[112] M. Li *et al.*, "Synthesis of pure metastable wurtzite CZTS nanocrystals by facile
one-pot method," *J. Phys. Chem. C*, vol. 116, no. 50, pp. 26507–26516, Dec. 2012.

[113] Y. Sun, B. Mayers, and Y. Xia, "Transformation of silver nanospheres into
nanobelts and triangular nanoplates through a thermal process," *Nano Lett.*, vol. 3,
no. 5, pp. 675–679, 2003.

[114] P. W. Voorhees, "The theory of Ostwald ripening," *J. Stat. Phys.*, vol. 38, no. 1–2,

pp. 231–252, Jan. 1985.

[115] S. Govindraju, M. P. Kalenga, M. Airo, M. J. Moloto, L. M. Sikhwivhilu, and N. Moloto, "Size quantization in Cu2Se nanocrystals," *Opt. Mater. (Amst).*, vol. 38, pp. 310–313, Dec. 2014.

[116] J. Tang, S. Hinds, S. O. Kelley, and E. H. Sargent, "Synthesis of colloidal CuGaSe2, CuInSe2, and Cu(InGa)Se2 nanoparticles," *Chem. Mater.*, vol. 20, no. 22, pp. 6906–6910, Nov. 2008.

[117] Y. su Kim *et al.*, "Synthesis of efficient near-infrared-emitting CuInS $_2$ /ZnS quantum dots by inhibiting cation-exchange for bio application," *RSC Adv.*, vol. 7, no. 18, pp. 10675–10682, Feb. 2017.

[118] X. Kang, Y. Yang, L. Huang, Y. Tao, L. Wang, and D. Pan, "Large-scale synthesis of water-soluble CuInSe $_2$ /ZnS and AgInSe $_2$ /ZnS core/shell quantum dots," *Green Chem.*, vol. 17, no. 8, pp. 4482–4488, Aug. 2015.

[119] Y. Chen, S. Li, L. Huang, and D. Pan, "Green and Facile Synthesis of Water-Soluble Cu–In–S/ZnS Core/Shell Quantum Dots," *Inorg. Chem.*, vol. 52, no. 14, pp. 7819–7821, Jul. 2013.

[120] A. Raevskaya, O. Rosovik, A. Kozytskiy, O. Stroyuk, V. Dzhagan, and D. R. T. Zahn, "Non-stoichiometric Cu–In–S@ZnS nanoparticles produced in aqueous solutions as light harvesters for liquid-junction photoelectrochemical solar cells," *RSC Adv.*, vol. 6, no. 102, pp. 100145–100157, Oct. 2016.

[121] A. D. P. Leach and J. E. Macdonald, "Optoelectronic Properties of CuInS $_2$ Nanocrystals and Their Origin," *J. Phys. Chem. Lett.*, vol. 7, no. 3, pp. 572–583, Feb. 2016.

[122] M. S. Hosseini and H. Jahanbani, "Synthesis of CdS nanoparticles quantum dots capped by 2,2′-dithiodibenzoic acid and study of its interaction with some transition metal ions," *J. Lumin.*, vol. 140, pp. 65–70, Aug. 2013.

[123] *,† Dmitri V. Talapin *et al.*, "Highly Emissive Colloidal CdSe/CdS Heterostructures of Mixed Dimensionality," 2003.

[124] A. Fiore *et al.*, "Tetrapod-Shaped Colloidal Nanocrystals of II−VI Semiconductors Prepared by Seeded Growth," *J. Am. Chem. Soc.*, vol. 131, no. 6, pp. 2274–2282, Feb. 2009.

[125] M. Li *et al.*, "Synthesis of Pure Metastable Wurtzite CZTS Nanocrystals by Facile One-Pot Method," *J. Phys. Chem. C*, vol. 116, no. 50, pp. 26507–26516, Dec. 2012.

[126] S. G. Kwon and T. Hyeon, "Formation Mechanisms of Uniform Nanocrystals via Hot-Injection and Heat-Up Methods," *Small*, vol. 7, no. 19, pp. 2685–2702, Oct. 2011.

[127] Y. Zhou *et al.*, "Efficient polymer nanocrystal hybrid solar cells by improved nanocrystal composition," *Sol. Energy Mater. Sol. Cells*, vol. 95, no. 12, pp. 3227–3232, Dec. 2011.

[128] L. Li, A. Pandey, D. J. Werder, B. P. Khanal, J. M. Pietryga, and V. I. Klimov,

"Efficient Synthesis of Highly Luminescent Copper Indium Sulfide-Based Core/Shell Nanocrystals with Surprisingly Long-Lived Emission," *J. Am. Chem. Soc.*, vol. 133, no. 5, pp. 1176–1179, Feb. 2011.

[129] W.-S. Song and H. Yang, "Fabrication of white light-emitting diodes based on solvothermally synthesized copper indium sulfide quantum dots as color converters," *Appl. Phys. Lett.*, vol. 100, no. 18, p. 183104, Apr. 2012.

[130] H. Zhong *et al.*, "Noninjection Gram-Scale Synthesis of Monodisperse Pyramidal CuInS $_2$ Nanocrystals and Their Size-Dependent Properties," *ACS Nano*, vol. 4, no. 9, pp. 5253–5262, Sep. 2010.

[131] M. Nam, S. Lee, J. Park, S.-W. Kim, and K.-K. Lee, "Development of Hybrid Photovoltaic Cells by Incorporating CuInS $_2$ Quantum Dots into Organic Photoactive Layers," *Jpn. J. Appl. Phys.*, vol. 50, no. 6, p. 06GF02, Jun. 2011.

[132] J.-J. He, W.-H. Zhou, M. Li, Z.-L. Hou, Y.-F. Du, and S.-X. Wu, "One-pot route for preparation of monodisperse CuInS2 nanocrystals," *Mater. Lett.*, vol. 66, no. 1, pp. 96–98, Jan. 2012.

[133] H. Zhong *et al.*, "Controlled Synthesis and Optical Properties of Colloidal Ternary Chalcogenide CuInS $_2$ Nanocrystals," *Chem. Mater.*, vol. 20, no. 20, pp. 6434–6443, Oct. 2008.

[134] X. Tang, W. Cheng, E. S. G. Choo, and J. Xue, "Synthesis of CuInS2–ZnS alloyed nanocubes with high luminescence," *Chem. Commun.*, vol. 47, no. 18, p. 5217, Apr. 2011.
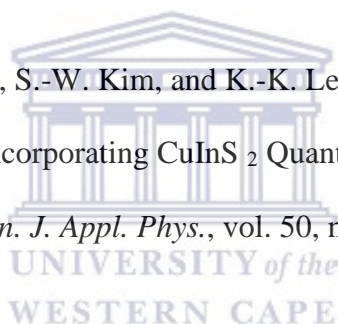
[135] K. Das, S. K. Panda, S. Gorai, P. Mishra, and S. Chaudhuri, "Effect of Cu/In molar ratio on the microstructural and optical properties of microcrystalline CuInS2 prepared by solvothermal route," *Mater. Res. Bull.*, vol. 43, no. 10, pp. 2742–2750, Oct. 2008.

[136] B. Koo, R. N. Patel, and B. A. Korgel, "Synthesis of CuInSe $_2$ Nanocrystals with Trigonal Pyramidal Shape," *J. Am. Chem. Soc.*, vol. 131, no. 9, pp. 3134–3135, Mar. 2009.

[137] A. de Kergommeaux *et al.*, "Synthesis of colloidal CuInSe2 nanocrystals films for photovoltaic applications," *Sol. Energy Mater. Sol. Cells*, vol. 95, pp. S39–S43, May 2011.

[138] D. Pan *et al.*, "Synthesis of Cu−In−S Ternary Nanocrystals with Tunable Structure and Composition," *J. Am. Chem. Soc.*, vol. 130, no. 17, pp. 5620–5621, Apr. 2008.

[139] D. Astruc, E. Boisselier, and C. Ornelas, "Dendrimers Designed for Functions: From Physical, Photophysical, and Supramolecular Properties to Applications in Sensing, Catalysis, Molecular Electronics, Photonics, and Nanomedicine," *Chem. Rev.*, vol. 110, no. 4, pp. 1857–1959, Apr. 2010.

[140] I. J. Majoros, C. R. Williams, A. Becker, J. R. Baker, and Jr., "Methotrexate delivery via folate targeted dendrimer-based nanotherapeutic platform.," *Wiley Interdiscip. Rev. Nanomed. Nanobiotechnol.*, vol. 1, no. 5, pp. 502–10, 2009.

[141] A. Almonam and A. Alsalam Baleg, "Synthesis and Electrochemistry of Novel Conducting Dendrimeric Star Copolymers on Poly(Propylene imine) Dendrimer
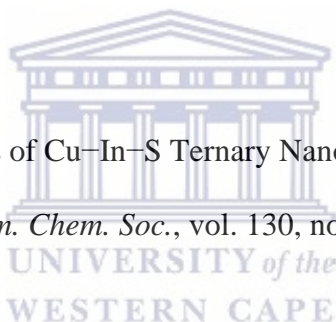
Title," 2011.

[142] P. Holister, C. R. Vas, and T. Harper, "Dendrimers Technology White Papers nr. 6."

[143] E. Abbasi *et al.*, "Dendrimers: synthesis, applications, and properties.," *Nanoscale Res. Lett.*, vol. 9, no. 1, p. 247, 2014.

[144] "Full-Text."

[145] D. A. Tomalia *et al.*, "A New Class of Polymers: Starburst-Dendritic Macromolecules," *Polym. J.*, vol. 17, no. 1, pp. 117–132, Jan. 1985.

[146] U. Hahn *et al.*, "Light-Harvesting Dendrimers: Efficient Intra- and Intermolecular Energy-Transfer Processes in a Species Containing 65 Chromophoric Groups of Four Different Types," *Angew. Chemie*, vol. 114, no. 19, pp. 3747–3750, Oct. 2002.

[147] † Daniel L. Dermody, *,†,‡ and Richard M. Crooks, and § Taisun Kim*, "Interactions between Organized, Surface-Confined Monolayers and Vapor-Phase Probe Molecules. 11. Synthesis, Characterization, and Chemical Sensitivity of Self-Assembled Polydiacetylene/Calix[n]arene Bilayers," 1996.

[148] J. Bu, Z. M. A. Judeh, C. B. Ching, and S. Kawi, "Epoxidation of Olefins Catalyzed by Mn(II) Salen Complex Anchored on PAMAM–SiO2 Dendrimer," *Catal. Letters*, vol. 85, no. 3/4, pp. 183–187, 2003.

[149] B. D. Viers, B. J. Bauer, Y. Akpalu, F. Gröhn, D. Liu, and G. Kim, "Polymer Preprints," 2000.

[150] S. I. Stupp, S. Son, H. C. Lin, and L. S. Li, "Synthesis of two-dimensional polymers.," *Science*, vol. 259, no. 5091, pp. 59–63, Jan. 1993.

[151] D. A. Tomalia, A. M. Naylor, and W. A. Goddard, "Starburst Dendrimers: Molecular-Level Control of Size, Shape, Surface Chemistry, Topology, and Flexibility from Atoms to Macroscopic Matter," *Angew. Chemie Int. Ed. English*, vol. 29, no. 2, pp. 138–175, Feb. 1990.

[152] D. Gudat, "Inorganic Cauliflower: Functional Main Group Element Dendrimers Constructed from Phosphorus- and Silicon-Based Building Blocks," *Angew. Chemie Int. Ed. English*, vol. 36, no. 18, pp. 1951–1955, Oct. 1997.

[153] J. M. J. Fréchet, C. J. Hawker, I. Gitsov, and J. W. Leon, "Dendrimers and Hyperbranched Polymers: Two Families of Three-Dimensional Macromolecules with Similar but Clearly Distinct Properties," *J. Macromol. Sci. Part A*, vol. 33, no. 10, pp. 1399–1425, Oct. 1996.

[154] A. A. A. Baleg *et al.*, "Synthesis and characterization of poly(propylene imine) dendrimer – Polypyrrole conducting star copolymer," *J. Electroanal. Chem.*, vol. 652, no. 1–2, pp. 18–25, Mar. 2011.

[155] "Poly(propylene imine) dendrimers - SyMO-Chem." [Online]. Available: http://www.symo-chem.nl/dendrimer-chemistry/. [Accessed: 30-Nov-2018].

[156] A. Erdem, E. Eksin, E. Kesici, and E. Yaralı, "Dendrimers Integrated Biosensors for Healthcare Applications," *Nanotechnol. Biosens.*, pp. 307–317, Jan. 2018.

[157] C. Wörner and R. Mülhaupt, "Polynitril- und polyaminfunktionalisierte Poly(trimethylenimin)-Dendrimere," *Angew. Chemie*, vol. 105, no. 9, pp. 1367–1370, Sep. 1993.

[158] E. M. M. de Brabander-van den Berg and E. W. Meijer, "Poly(propylene imine) Dendrimers: Large-Scale Synthesis by Hetereogeneously Catalyzed Hydrogenations," *Angew. Chemie Int. Ed. English*, vol. 32, no. 9, pp. 1308–1311, Sep. 1993.

[159] S. Watanabe and S. L. Regen, "Supramolecular Chemistry I: Directed Synthesis and Molecular Recognition," Berlin, 1994.

[160] V. Percec, P. Chu, and M. Kawasumi, ""Willowlike" Thermotropic Dendrimers," 1994.

[161] P. Nadrah, F. Porta, O. Planinšek, A. Kros, and M. Gaberšček, "Poly(propylene imine) dendrimer caps on mesoporous silica nanoparticles for redox-responsive release: smaller is better," *Phys. Chem. Chem. Phys.*, vol. 15, no. 26, p. 10740, Jun. 2013.

[162] S. P. Malinga, O. A. Arotiba, R. W. Krause, S. F. Mapolie, and B. B. Mamba, "Synthesis and characterisation of generation 2 and 3 poly(propylene imine) dendrimer capped NiFe nanoalloy," *Mater. Lett.*, vol. 68, pp. 324–326, Feb. 2012.

[163] Q. Gao, J. Han, and Z. Ma, "Polyamidoamine dendrimers-capped carbon dots/Au nanocrystal nanocomposites and its application for electrochemical immunosensor," *Biosens. Bioelectron.*, vol. 49, pp. 323–328, Nov. 2013.

[164] S. K. Gayen *et al.*, "Synthesis and optical spectroscopy of a hybrid cadmium sulfide-dendrimer nanocomposite," *J. Opt. Soc. Am. B*, vol. 24, no. 12, p. 3064, Dec. 2007.

[165] A. C. Wisher, I. Bronstein, and V. Chechik, "Thiolated PAMAM dendrimer-coated CdSe/ZnSe nanoparticles as protein transfection agents," *Chem. Commun.*, vol. 0, no. 15, p. 1637, Mar. 2006.

[166] S. Shukla *et al.*, "Polymeric Nanocomposites Involving a Physical Blend of IR Sensitive Quantum Dots and Carbon Nanotubes for Photodetection," *J. Phys. Chem. C*, vol. 114, no. 7, pp. 3180–3184, Feb. 2010.

[167] J. M. Lee *et al.*, "Exciton Dissociation and Charge-Transport Enhancement in Organic Solar Cells with Quantum-Dot/N-doped CNT Hybrid Nanomaterials," *Adv. Mater.*, vol. 25, no. 14, pp. 2011–2017, Apr. 2013.

[168] H. Kim, H. Jeong, T. K. An, C. E. Park, and K. Yong, "Hybrid-type quantum-dot cosensitized ZnO nanowire solar cell with enhanced visible-light harvesting," *ACS Appl. Mater. Interfaces*, vol. 5, no. 2, pp. 268–275, Jan. 2013.

[169] P. K. De and D. C. Neckers, "Polymer-quantum dot-carbon nanotube composites formation under visible light irradiation," *J. Photochem. Photobiol. A Chem.*, vol. 252, pp. 8–13, Jan. 2013.

[170] R. Soltani *et al.*, "Light harvesting enhancement upon incorporating alloy structured CdSeXTe1−X quantum dots in DPP:PC61BM bulk heterojunction solar cells," *J. Mater. Chem. C*, vol. 5, no. 3, pp. 654–662, 2017.
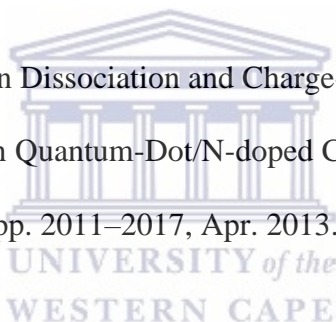
[171] S. R, K. AA, and A. T, "Recent Developments in Quantum Dots/CNT Co-Sensitized Organic Solar Cells," *J. Mater. Sci. Eng.*, vol. 06, no. 03, 2017.

[172] J. Min *et al.*, "Two Similar Near-Infrared (IR) Absorbing Benzannulated Aza-BODIPY Dyes as Near-IR Sensitizers for Ternary Solar Cells," *ACS Appl. Mater. Interfaces*, vol. 5, no. 12, pp. 5609–5616, Jun. 2013.

[173] M. Ye *et al.*, "Recent advances in quantum dot-sensitized solar cells: insights into photoanodes, sensitizers, electrolytes and counter electrodes," *Sustain. Energy Fuels*, vol. 1, no. 6, pp. 1217–1231, 2017.

[174] D. Astruc, E. Boisselier, and C. Ornelas, "Dendrimers designed for functions: From physical, photophysical, and supramolecular properties to applications in sensing, catalysis, molecular electronics, photonics, and nanomedicine," *Chem. Rev.*, vol. 110, no. 4, pp. 1857–1959, Apr. 2010.

[175] F. Vögtle, S. Gestermann, R. Hesse, H. Schwierz, and B. Windisch, "Functional dendrimers," *Progress in Polymer Science (Oxford)*, vol. 25, no. 7. Elsevier Science Ltd, pp. 987–1041, 2000.

[176] K. Inoue, "Functional dendrimers, hyperbranched and star polymers," *Progress in Polymer Science (Oxford)*, vol. 25, no. 4. Elsevier Science Ltd, pp. 453–571, 2000.

[177] G. M. Dykes, "Dendrimers: A review of their appeal and applications," *Journal of Chemical Technology and Biotechnology*, vol. 76, no. 9. pp. 903–918, 2001.

[178] R. VTambe, S. SPakhare, M. GJadhav, S. STiwari, and C. RRai, "DENDRIMER: A

SMART POLYMER," *IJRRPAS*, vol. 2, no. 3, pp. 513–528.

[179] A. Trinchi and T. H. Muster, "A review of surface functionalized amine terminated dendrimers for application in biological and molecular sensing," *Supramolecular Chemistry*, vol. 19, no. 7. pp. 431–445, Oct-2007.

[180] B. K. Nanjwade, H. M. Bechra, G. K. Derkar, F. V. Manvi, and V. K. Nanjwade, "Dendrimers: Emerging polymers for drug-delivery systems," *European Journal of Pharmaceutical Sciences*, vol. 38, no. 3. pp. 185–196, 08-Oct-2009.

[181] W. D. Jang, K. M. Kamruzzaman Selim, C. H. Lee, and I. K. Kang, "Bioinspired application of dendrimers: From bio-mimicry to biomedical applications," *Progress in Polymer Science (Oxford)*, vol. 34, no. 1. pp. 1–23, Jan-2009.

[182] S. Tripathy and M. K. Das, "Dendrimers and their Applications as Novel Drug Delivery Carriers," *J. Appl. Pharm. Sci.*, vol. 3, no. 09, pp. 142–149, 2013.

[183] A. W. Bosman, H. M. Janssen, and E. W. Meijer, "About Dendrimers: Structure, Physical Properties, and Applications," *Chem. Rev.*, vol. 99, no. 7, pp. 1665–1688, 1999.

[184] E. Abbasi *et al.*, "Dendrimers: Synthesis, applications, and properties," *Nanoscale Research Letters*, vol. 9, no. 1. Springer New York LLC, pp. 1–10, 2014.

[185] C. Wörner and R. Mülhaupt, "Polynitril- und polyaminfunktionalisierte Poly(trimethylenimin)-Dendrimere," *Angew. Chemie*, vol. 105, no. 9, pp. 1367–1370, Sep. 1993.

[186] E. M. M. de Brabander-van den Berg and E. W. Meijer, "Poly(propylene imine) Dendrimers: Large-Scale Synthesis by Hetereogeneously Catalyzed Hydrogenations," *Angew. Chemie Int. Ed. English*, vol. 32, no. 9, pp. 1308–1311, 1993.

[187] S. Watanabe and S. L. Regen, "Dendrimers as Building Blocks for Multilayer Construction," *J. Am. Chem. Soc.*, vol. 116, no. 19, pp. 8855–8856, Sep. 1994.

[188] V. Percec, P. Chu, and M. Kawasumi, "Toward 'Willowlike' Thermotropic Dendrimers," *Macromolecules*, vol. 27, no. 16, pp. 4441–4453, Aug. 1994.

[189] S. R. Barman, A. Nain, S. Jain, N. Punjabi, S. Mukherji, and J. Satija, "Dendrimer as a multifunctional capping agent for metal nanoparticles for use in bioimaging, drug delivery and sensor applications," *Journal of Materials Chemistry B*, vol. 6, no. 16. Royal Society of Chemistry, pp. 2368–2384, 2018.

[190] W. Sun, S. Mignani, M. Shen, and X. Shi, "Dendrimer-based magnetic iron oxide nanoparticles: their synthesis and biomedical applications," *Drug Discovery Today*, vol. 21, no. 12. Elsevier Ltd, pp. 1873–1885, 01-Dec-2016.

[191] L. Zhao, X. Shi, and J. Zhao, "Dendrimer-based contrast agents for PET imaging," *Drug Delivery*, vol. 24, no. 2. Taylor and Francis Ltd, pp. 81–93, 01-Nov-2017.

[192] M. Hasanzadeh, N. Shadjou, M. Eskandani, J. Soleymani, F. Jafari, and M. de la Guardia, "Dendrimer-encapsulated and cored metal nanoparticles for electrochemical nanobiosensing," *TrAC - Trends in Analytical Chemistry*, vol. 53. Elsevier B.V., pp. 137–149, 2014.

[193] V. S. Myers, M. G. Weir, E. V. Carino, D. F. Yancey, S. Pande, and R. M. Crooks, "Dendrimer-encapsulated nanoparticles: New synthetic and characterization methods and catalytic applications," *Chemical Science*, vol. 2, no. 9. pp. 1632–1646, Sep-2011.

[194] X. Peng, Q. Pan, and G. L. Rempel, "Bimetallic dendrimer-encapsulated nanoparticles as catalysts: A review of the research advances," *Chemical Society Reviews*, vol. 37, no. 8. pp. 1619–1628, 2008.

[195] Y. J. Jin *et al.*, "Application of photoluminescent CdS/PAMAM nanocomposites in fingerprint detection," *Forensic Sci. Int.*, vol. 179, no. 1, pp. 34–38, Jul. 2008.

[196] K. Sooklal, L. H. Hanus, H. J. Ploehn, and C. J. Murphy, "A Blue-Emitting CdS/Dendrimer Nanocomposite," *Adv. Mater.*, vol. 10, no. 14, pp. 1083–1087, 1998.

[197] A. C. Wisher, I. Bronstein, and V. Chechik, "Thiolated PAMAM dendrimer-coated CdSe/ZnSe nanoparticles as protein transfection agents," *Chem. Commun.*, no. 15, pp. 1637–1639, 2006.

[198] J. G. G. E. da Silva, M. Algarra, and B. B., "Synthesis and Analytical Applications of Quantum Dots Coated with Different Generations of DAB Dendrimers," in *Advances in Nanocomposites - Synthesis, Characterization and Industrial Applications*, InTech, 2011.

[199] B. I. Lemon and R. M. Crooks, "Preparation and characterization of dendrimer-encapsulated CdS semiconductor quantum dots [12]," *Journal of the American*
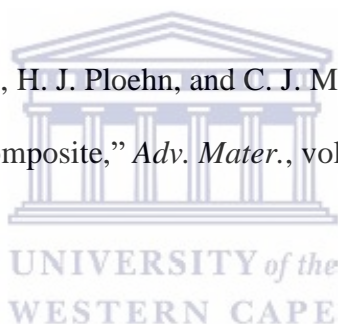
Chemical Society, vol. 122, no. 51. pp. 12886–12887, 27-Dec-2000.

[200] S. K. Gayen *et al.*, "Synthesis and optical spectroscopy of a hybrid cadmium sulfide-dendrimer nanocomposite," *J. Opt. Soc. Am. B*, vol. 24, no. 12, p. 3064, Dec. 2007.

[201] G. Jie, L. Wang, J. Yuan, and S. Zhang, "Versatile electrochemiluminescence assays for cancer cells based on dendrimer/CdSe-ZnS-quantum dot nanoclusters," *Anal. Chem.*, vol. 83, no. 10, pp. 3873–3880, May 2011.

[202] Q. Gao, J. Han, and Z. Ma, "Polyamidoamine dendrimers-capped carbon dots/Au nanocrystal nanocomposites and its application for electrochemical immunosensor," *Biosens. Bioelectron.*, vol. 49, pp. 323–328, Nov. 2013.

[203] D. Banerjee, "ii MULTIDIMENSIONAL NMR STUDIES OF THE HYPERBRANCHED POLYMERS AND PHOSPHAZENE SYSTEMS."

[204] D. Appelhans *et al.*, "Dense-shell glycodendrimers: UV/Vis and electron paramagnetic resonance study of metal ion complexation," *Proc. R. Soc. A Math. Phys. Eng. Sci.*, vol. 466, no. 2117, pp. 1489–1513, May 2010.

[205] K. Tamano and T. Imae, "Investigation of Luminescent poly(propylene imine) dendrimer," *J. Nanosci. Nanotechnol.*, vol. 8, no. 9, pp. 4329–4334, Sep. 2008.

[206] R. A. Olowu *et al.*, "Spectroelectrochemical Dynamics of Dendritic Poly (Propylene-Estradiol Biosensor,imine)-Polythiophene Star Copolymer Aptameric 17β-Estradiol Biosensor Sythensis and characterization of dendritic star copolymer

View project Formulation of Slow Release Fertilizer (cellulose-g-poly(acrylamide)/HA/Soluble Fertilizer) Composite using a superabsorbent View project Spectroelectrochemical Dynamics of Dendritic Poly (Propylene imine)-Polythiophene Star Copolymer Aptameric 17□-Estradiol Biosensor," 2011.

[207] H. R. Makelane, O. Tovide, C. E. Sunday, T. Waryo, and E. I. Iwuoha, "Electrochemical interrogation of G3-poly(propylene thiophenoimine) dendritic star polymer in phenanthrene sensing," *Sensors (Switzerland)*, vol. 15, no. 9, pp. 22343–22363, Sep. 2015.

[208] M. Franckevičius, "EXCITED-STATE DYNAMICS OF PPI AND PAMAM DENDRIMERS FUNCTIONALIZED WITH PHOTOCHROMIC TERMINAL GROUPS," 2011.

[209] M. Franckevičius, R. Vaišnoras, M. Marcos, J. L. Serrano, and V. Gulbinas, "Excited state dynamics of PPI dendrimers functionalized with 4-(4′-ethoxybenzoyloxy)salicylaldehyde chromophores," *Chem. Phys.*, vol. 412, pp. 77–83, Feb. 2013.

[210] E. Badaeva *et al.*, "Excited-state structure of oligothiophene dendrimers: Computational and experimental study," *J. Phys. Chem. B*, vol. 114, no. 48, pp. 15808–15817, Dec. 2010.

[211] M. Franckevičius *et al.*, "Poli(propileno-imino) dendrimeru{ogonek} UV spektru{ogonek} savybes," *Lith. J. Phys.*, vol. 51, no. 3, pp. 205–209, 2011.

[212] M. Golshan, M. Salami-Kalajahi, M. Mirshekarpour, H. Roghani-Mamaqani, and

M. Mohammadi, "Synthesis and characterization of poly(propylene imine)-dendrimer-grafted gold nanoparticles as nanocarriers of doxorubicin," *Colloids Surfaces B Biointerfaces*, vol. 155, pp. 257–265, Jul. 2017.

[213] S. Salimpour Abkenar, R. Mohammad, and A. Malek, "Preparation, characterization, and antimicrobial property of cotton cellulose fabric grafted with poly (propylene imine) dendrimer."

[214] B. Devarakonda, R. A. Hill, W. Liebenberg, M. Brits, and M. M. De Villiers, "Comparison of the aqueous solubilization of practically insoluble niclosamide by polyamidoamine (PAMAM) dendrimers and cyclodextrins," *Int. J. Pharm.*, vol. 304, no. 1–2, pp. 193–209, Nov. 2005.

[215] R. Jenkins and R. L. Snyder, *Chemical Analysis Vol 138: Introduction to X-ray Powder Diffraction*, vol. 138. 1996.

[216] A. C. Bakir, N. Ahin, R. Polat, and Z. Dursun, "Electrocatalytic reduction of oxygen on bimetallic copper-gold nanoparticles-multiwalled carbon nanotube modified glassy carbon electrode in alkaline solution," *J. Electroanal. Chem.*, vol. 662, no. 2, pp. 275–280, Nov. 2011.

[217] E. A. Songa, O. A. Arotiba, J. H. O. Owino, N. Jahed, P. G. L. Baker, and E. I. Iwuoha, "Electrochemical detection of glyphosate herbicide using horseradish peroxidase immobilized on sulfonated polymer matrix," *Bioelectrochemistry*, vol. 75, no. 2, pp. 117–123, Jun. 2009.

[218] S. K. Shukla, A. K. Mishra, B. B. Mamba, and O. A. Arotiba, "Amperometric and

Photometric Responses of in Situ Coupled Glucose Oxidase-Poly (Propylene Imine) Dendrimer Based Glucose Biosensor," 2013.

[219] P. U. Londhe, A. B. Rohom, M. G. Lakhe, G. R. Bhand, and N. B. Chaure, "Electrochemically synthesized CuInSe2 thin films from non-aqueous electrolyte for solar cell applications," *Semicond. Sci. Technol.*, vol. 31, no. 12, Nov. 2016.

[220] "(16) (PDF) Synthesis of CuInSe 2 Nanopowder in Polyethylene Glycol." [Online]. Available:

https://www.researchgate.net/publication/278024471_Synthesis_of_CuInSe_2_Nan opowder_in_Polyethylene_Glycol. [Accessed: 30-Oct-2019].

[221] F. W. Ohrendorf and H. Haeuseler, "Lattice dynamics of chalcopyrite type compounds. Part I. Vibrational frequencies," *Cryst. Res. Technol.*, vol. 34, no. 3, pp. 339–349, 1999.

[222] H. S. You *et al.*, "Preparation and characterization of various surface-modified semiconductor nanocrystals," *Bull. Korean Chem. Soc.*, vol. 30, no. 12, pp. 3137–3140, Dec. 2009.

[223] K. A. Desai, "FABRICATION AND CHARACTERIZATION OF 3-D ALL POLYMER FLEXIBLE SOLAR CELL," 2011.

[224] D. Dorfs, R. Krahne, A. Falqui, L. Manna, C. Giannini, and D. Zanchet, "Quantum Dots: Synthesis and Characterization," in *Comprehensive Nanoscience and Technology*, vol. 1–5, Elsevier Inc., 2010, pp. 219–270.

[225] V. T. Chebrolu and H. J. Kim, "Recent progress in quantum dot sensitized solar cells: An inclusive review of photoanode, sensitizer, electrolyte, and the counter electrode," *J. Mater. Chem. C*, vol. 7, no. 17, pp. 4911–4933, 2019.

[226] H. Lee *et al.*, "Efficient CdSe quantum dot-sensitized solar cells prepared by an improved successive ionic layer adsorption and reaction process," *Nano Lett.*, vol. 9, no. 12, pp. 4221–4227, Dec. 2009.

[227] X. Shen, J. Jia, Y. Lin, and X. Zhou, "Enhanced performance of CdTe quantum dot sensitized solar cell via anion exchanges," *J. Power Sources*, vol. 277, pp. 215–221, Mar. 2015.

[228] B.-C. Serban *et al.*, "6 Quantum Dots versus Dyes in Sensitized Solar Cells: Synthesis, Optimization, Performance."

[229] Z. Pan, H. Rao, I. Mora-Seró, J. Bisquert, and X. Zhong, "Quantum dot-sensitized solar cells."

[230] K. C. Cheng *et al.*, "Synthesis of near-infrared silver-indium-sulfide (AgInS 2) quantum dots as heavy-metal free photosensitizer for solar cell applications," *Chem. Phys. Lett.*, vol. 515, no. 4–6, pp. 254–257, Oct. 2011.

[231] D. Aldakov and P. Reiss, "Safer-by-Design Fluorescent Nanocrystals: Metal Halide Perovskites vs Semiconductor Quantum Dots," *J. Phys. Chem. C*, vol. 123, no. 20, pp. 12527–12541, May 2019.

[232] L. Hu *et al.*, "Metal-based quantum dots: Synthesis, surface modification, transport

and fate in aquatic environments and toxicity to microorganisms," *RSC Adv.*, vol. 6, no. 82, pp. 78595–78610, 2016.

[233] A. S. Fuhr, H. Jin Yun, N. S. Makarov, H. Li, H. McDaniel, and V. I. Klimov, "Light Emission Mechanisms in CuInS 2 Quantum Dots Evaluated by Spectral Electrochemistry," vol. 30, p. 7, 2019.

[234] J. Lee and C.-S. Han, "Large-scale synthesis of highly emissive and photostable CuInS 2 /ZnS nanocrystals through hybrid flow reactor," 2014.

[235] M. G. Panthani *et al.*, "Synthesis of CuInS2, CuInSe2, and Cu(In xGa1-x)Se2 (CIGS) nanocrystal 'inks' for printable photovoltaics," *J. Am. Chem. Soc.*, vol. 130, no. 49, pp. 16770–16777, Dec. 2008.

[236] K. T. Yong *et al.*, "Synthesis of ternary CuInS2/ZnS quantum dot bioconjugates and their applications for targeted cancer bioimaging," *Integr. Biol.*, vol. 2, no. 2–3, pp. 121–129, 2010.

[237] X. Bai, F. Purcell-Milton, and Y. K. Gun'ko, "Optical properties, synthesis, and potential applications of cu-based ternary or quaternary anisotropic quantum dots, polytypic nanocrystals, and core/shell heterostructures," *Nanomaterials*, vol. 9, no. 1. MDPI AG, 01-Jan-2019.

[238] A. C. Berends, M. J. J. Mangnus, C. Xia, F. T. Rabouw, and C. De Mello Donega, "Optoelectronic Properties of Ternary I-III-VI 2 Semiconductor Nanocrystals: Bright Prospects with Elusive Origins," *Journal of Physical Chemistry Letters*, vol. 10, no. 7. American Chemical Society, pp. 1600–1616, 04-Apr-2019.

[239] H. Limborço *et al.*, " CuInSe 2 quantum dots grown by molecular beam epitaxy on amorphous SiO 2 surfaces ," *Beilstein J. Nanotechnol.*, vol. 10, pp. 1103–1111, May 2019.

[240] Z. Khéfacha, N. Safta, and M. Dachraoui, "The Band Gap Energy Calculated for Cd 1-x Zn x S Quantum Dots grown by the Sol gel Method," 2016.

[241] A. De Kergommeaux *et al.*, "Synthesis of colloidal CuInSe2 nanocrystals films for photovoltaic applications," in *Solar Energy Materials and Solar Cells*, 2011, vol. 95, no. SUPPL. 1.

[242] D. R. Pernik *et al.*, "Plastic Microgroove Solar Cells Using CuInSe2 Nanocrystals," *ACS Energy Lett.*, vol. 1, no. 5, pp. 1021–1027, Nov. 2016.

[243] R. Kondrotas *et al.*, "Towards In-reduced photovoltaic absorbers: Evaluation of zinc-blende CuInSe2-ZnSe solid solution," *Sol. Energy Mater. Sol. Cells*, vol. 160, pp. 26–33, Feb. 2017.

[244] S. Mandati, B. V. Sarada, S. R. Dey, and S. V. Joshi, "Pulsed Electrochemical Deposition of CuInSe2 and Cu(In,Ga)Se2 Semiconductor Thin Films," in *Semiconductors - Growth and Characterization*, InTech, 2018.

[245] M. Kemell, M. Ritala, and M. Leskelä, "Thin Film Deposition Methods for CuInSe 2 Solar Cells," *Crit. Rev. Solid State Mater. Sci.*, vol. 30, pp. 1–31, 2005.

[246] M. Zhao, L. Sun, and R. M. Crooks, "Preparation of Cu Nanoclusters within Dendrimer Templates," *J. Am. Chem. Soc.*, vol. 120, no. 19, pp. 4877–4878, May

1998.

[247] H. Zhong, Z. Wang, E. Bovero, Z. Lu, F. C. J. M. Van Veggel, and G. D. Scholes, "Colloidal CuInSe2 nanocrystals in the quantum confinement regime: Synthesis, optical properties, and electroluminescence," *J. Phys. Chem. C*, vol. 115, no. 25, pp. 12396–12402, Jun. 2011.

[248] B. Sciacca, A. O. Yalcin, and E. C. Garnett, "Transformation of Ag Nanowires into Semiconducting AgFeS<inf>2</inf> Nanowires," *J. Am. Chem. Soc.*, vol. 137, no. 13, pp. 4340–4343, Mar. 2015.

[249] R. Bose *et al.*, "Direct femtosecond observation of charge carrier recombination in ternary semiconductor nanocrystals: The effect of composition and shelling," *J. Phys. Chem. C*, vol. 119, no. 6, pp. 3439–3446, Feb. 2015.

[250] O. Yarema, M. Yarema, D. Bozyigit, W. M. M. Lin, and V. Wood, "Independent Composition and Size Control for Highly Luminescent Indium-Rich Silver Indium Selenide Nanocrystals," *ACS Nano*, vol. 9, no. 11, pp. 11134–11142, Nov. 2015.

[251] R. Xie, M. Rutherford, and X. Peng, "Formation of high-quality I#III#VI semiconductor nanocrystals by tuning relative reactivity of cationic precursors," *J. Am. Chem. Soc.*, vol. 131, no. 15, pp. 5691–5697, Apr. 2009.

[252] H. Zhong *et al.*, "Controlled synthesis and optical properties of colloidal ternary chalcogenide CuInS2 nanocrystals," *Chem. Mater.*, vol. 20, no. 20, pp. 6434–6443, Oct. 2008.

[253] H. Zhong *et al.*, "Noninjection gram-scale synthesis of monodisperse pyramidal

CuInS 2 nanocrystals and their size-dependent properties," *ACS Nano*, vol. 4, no. 9,

pp. 5253–5262, Sep. 2010.

[254] K. Wang *et al.*, "Formation and photoluminescence properties of colloidal

ZnCuIn(SexS1 − x)2/ZnS nanocrystals with gradient composition," *J. Mater. Sci.*,

vol. 54, no. 3, pp. 2037–2048, Feb. 2019.

[255] W. Li, Z. Pan, and X. Zhong, "CuInSe2and CuInSe2-ZnS based high efficiency

'green' quantum dot sensitized solar cells," *J. Mater. Chem. A*, vol. 3, no. 4, pp.

1649–1655, Jan. 2015.

[256] M. Hjiri *et al.*, "Effect of indium doping on ZnO based-gas sensor for CO," *Mater.

Sci. Semicond. Process.*, vol. 27, no. 1, pp. 319–325, 2014.

[257] C. Xia, J. D. Meeldijk, H. C. Gerritsen, and C. De Mello Donega, "Highly

Luminescent Water-Dispersible NIR-Emitting Wurtzite CuInS2/ZnS Core/Shell

Colloidal Quantum Dots," *Chem. Mater.*, vol. 29, no. 11, pp. 4940–4951, Jun. 2017.

[258] L. Mu, F. Wang, and W. E. Buhro, "Exciton Splitting in Thin Copper Indium

Disulfide Nanosheets," *Chem. Mater.*, vol. 29, no. 8, pp. 3686–3693, Apr. 2017.

[259] H. Guo *et al.*, "Electrodeposited CuInSe2 counter electrodes for efficient and stable

quantum dot-sensitized solar cells," *Ceram. Int.*, vol. 44, no. 13, pp. 16092–16098,

Sep. 2018.

[260] D. Li *et al.*, "One-Pot Synthesis of Zincblende CuInSe 2 Nanocrystals via a Green

Solution Reaction Route," *Nano*, vol. 12, no. 9, Sep. 2017.

[261] B. Koo, R. N. Patel, and B. A. Korgel, "Synthesis of CuInSe2 nanocrystals with trigonal pyramidal shape," *J. Am. Chem. Soc.*, vol. 131, no. 9, pp. 3134–3135, Mar. 2009.

[262] V. Sousa *et al.*, "Superstructural Ordering in Hexagonal CuInSe $_2$ Nanoparticles," *Chem. Mater.*, vol. 31, no. 1, pp. 260–267, Jan. 2019.

[263] S. Ghosh, K. Ghosal, S. A. Mohammad, and K. Sarkar, "Dendrimer functionalized carbon quantum dot for selective detection of breast cancer and gene therapy," *Chem. Eng. J.*, vol. 373, pp. 468–484, Oct. 2019.

[264] P. U. Londhe, A. B. Rohom, M. G. Lakhe, G. R. Bhand, and N. B. Chaure, "Electrochemically synthesized CuInSe 2 thin films from non-aqueous electrolyte for solar cell applications," 2016.

[265] R. Chandran, A. K. Behera, and A. Mallik, "A novel CISe/Ga-Se two–step stack approach to electrodeposit photovoltaic quality Cu-poor CuInGaSe2 thin films," *Mater. Lett.*, vol. 252, pp. 244–247, Oct. 2019.

[266] J. Álvarez-García *et al.*, "Vibrational and crystalline properties of polymorphic CuInC 2 "C = Se, S… chalcogenides."

[267] R. Chandran, A. K. Behera, and A. Mallik, "Composition Tuning of Single Step Electrodeposited CuInSe2 Thin Films Using Sodium Dodecyl Sulfate as Additive," *J. Electron. Mater.*, vol. 48, no. 12, pp. 8129–8137, Dec. 2019.

[268] A. Mohan and S. Rajesh, "Temperature induced CuInSe 2 nanocrystal formation in the Cu 2 Se-In 3 Se 2 multilayer thin films," *Superlattices Microstruct.*, vol. 104, pp. 186–204, Apr. 2017.

[269] V. Perner *et al.*, "Hot injection synthesis of CuInS 2 nanocrystals using metal xanthates and their application in hybrid solar cells †," *This J. is Cite this New J. Chem*, vol. 43, p. 356, 2019.

[270] G. Socrates, *Infrared and Raman characteristic group frequencies, third edition*. 2001.

[271] C. Buchmaier *et al.*, "Room temperature synthesis of CuInS2 nanocrystals," *RSC Adv.*, vol. 6, no. 108, pp. 106120–106129, 2016.

[272] "Small Angle X-Ray Scattering (SAXS) from Bulks and Surfaces."

[273] "SAXS nanostructure analysis :: Anton Paar Wiki." [Online]. Available: https://wiki.anton-paar.com/za-en/saxs-nanostructure-analysis/. [Accessed: 01-Nov-2019].

[274] K. Nose, T. Omata, and O. Y. M. Shinya, "Colloidal synthesis of ternary copper indium diselenide quantum dots and their optical properties," *J. Phys. Chem. C*, vol. 113, no. 9, pp. 3455–3460, Mar. 2009.

[275] J. Bolze, V. Kogan, D. Beckers, and M. Fransen, "High-performance small-and wide-angle X-ray scattering (SAXS/WAXS) experiments on a multi-functional laboratory goniometer platform with easily exchangeable X-ray modules

ARTICLES YOU MAY BE INTERESTED IN High-performance small-and wide-angle X-ray scattering (SAXS/WAXS) experiments on a multi-functional laboratory goniometer platform with easily exchangeable X-ray modules," *Rev. Sci. Instrum.*, vol. 89, p. 85115, 2018.

[276] J. C. Porsiel, B. Temel, A. Schirmacher, E. Buhr, and G. Garnweitner, "Dimensional characterization of cadmium selenide nanocrystals via indirect Fourier transform evaluation of small-angle X-ray scattering data," *Nano Res.*, vol. 12, no. 11, pp. 2849–2857, Nov. 2019.

[277] H. Borchert *et al.*, "Determination of nanocrystal sizes: A comparison of TEM, SAXS, and XRD studies of highly monodisperse CoPt 3 particles," *Langmuir*, vol. 21, no. 5, pp. 1931–1936, Mar. 2005.

[278] J. Liu, W. Yang, Y. Li, L. Fan, and Y. Li, "Electrochemical studies of the effects of the size, ligand and composition on the band structures of CdSe, CdTe and their alloy nanocrystals," *Phys. Chem. Chem. Phys.*, vol. 16, no. 10, pp. 4778–4788, Mar. 2014.

[279] J. Liu, W. Yang, Y. Li, L. Fan, and Y. Li, "Electrochemical studies of the effects of the size, ligand and composition on the band structures of CdSe, CdTe and their alloy nanocrystals," *Phys. Chem. Chem. Phys.*, vol. 16, no. 10, pp. 4778–4788, Mar. 2014.

[280] M. Amelia, C. Lincheneau, S. Silvi, and A. Credi, "Electrochemical properties of CdSe and CdTe quantum dots.," *Chem. Soc. Rev.*, vol. 41, no. 17, pp. 5728–43, Sep. 2012.

[281] G. L. Xu *et al.*, "Tuning the structure and property of nanostructured cathode materials of lithium ion and lithium sulfur batteries," *Journal of Materials Chemistry A*, vol. 2, no. 47. Royal Society of Chemistry, pp. 19941–19962, 21-Dec-2014.

[282] D. Li, G. Xing, S. Tang, X. Li, L. Fan, and Y. Li, "Ultrathin ZnSe nanowires: One-pot synthesis: Via a heat-triggered precursor slow releasing route, controllable Mn doping and application in UV and near-visible light detection," *Nanoscale*, vol. 9, no. 39, pp. 15044–15055, Oct. 2017.

[283] H. Zhong *et al.*, "Noninjection Gram-Scale Synthesis of Monodisperse Pyramidal CuInS 2 Nanocrystals and Their Size-Dependent Properties method · CuInS 2 nanocrystals · light emitters · solar harvesters · quantum confinement effects · energy levels · cyclic voltammetry," vol. 4, p. 2, 2019.

[284] D. Aldakov *et al.*, "Oligothiophene-functionalized CdSe nanocrystals: Preparation and electrochemical properties," *Microchim. Acta*, vol. 160, no. 3, pp. 335–344, 2008.

[285] Y. Li, H. Zhong, R. Li, Y. Zhou, C. Yang, and Y. Li, "High-yield fabrication and electrochemical characterization of tetrapodal CdSe, CdTe, and CdSexTe1-x nanocrystals," *Adv. Funct. Mater.*, vol. 16, no. 13, pp. 1705–1716, Sep. 2006.

[286] H. Eckhardt, L. W. Shacklette, K. Y. Jen, and R. L. Elsenbaumer, "The electronic and electrochemical properties of poly(phenylene vinylenes) and poly(thienylene vinylenes): An experimental and theoretical study," *J. Chem. Phys.*, vol. 91, no. 2, pp. 1303–1315, 1989.

[287] H. Zhong *et al.*, "Noninjection gram-scale synthesis of monodisperse pyramidal CuInS2 nanocrystals and their size-dependent properties.," *ACS Nano*, vol. 4, no. 9, pp. 5253–62, Sep. 2010.

[288] M. Skompska, "Hybrid conjugated polymer/semiconductor photovoltaic cells," *Synthetic Metals*, vol. 160, no. 1–2. pp. 1–15, Jan-2010.

[289] A. S. Fuhr, H. J. Yun, N. S. Makarov, H. Li, H. McDaniel, and V. I. Klimov, "Light Emission Mechanisms in CuInS2 Quantum Dots Evaluated by Spectral Electrochemistry," *ACS Photonics*, vol. 4, no. 10, pp. 2425–2435, Oct. 2017.

[290] J. Jasieniak, M. Califano, and S. E. Watkins, "Size-dependent valence and conduction band-edge energies of semiconductor nanocrystals," in *ACS Nano*, 2011, vol. 5, no. 7, pp. 5888–5902.

[291] S. N. Inamdar, P. P. Ingole, and S. K. Haram, "Determination of band structure parameters and the quasi-particle gap of CdSe quantum dots by cyclic voltammetry.," *Chemphyschem*, vol. 9, no. 17, pp. 2574–9, Dec. 2008.

[292] P. P. Ingole *et al.*, "Band gap bowing at nanoscale: Investigation of CdSxSe 1-x alloy quantum dots through cyclic voltammetry and density functional theory," *J. Phys. Chem. C*, vol. 117, no. 14, pp. 7376–7383, Apr. 2013.

[293] M. Amelia *et al.*, "Redox properties of CdSe and CdSe-ZnS quantum dots in solution," *Pure Appl. Chem.*, vol. 83, no. 1, pp. 1–8, 2011.

[294] S. C. Boehme, H. Wang, L. D. A. Siebbeles, D. Vanmaekelbergh, and A. J.

Houtepen, "Electrochemical charging of CdSe quantum dot films: Dependence on void size and counterion proximity," *ACS Nano*, vol. 7, no. 3, pp. 2500–2508, Mar. 2013.

[295] V. Lesnyak *et al.*, "Alloyed copper chalcogenide nanoplatelets via partial cation exchange reactions," *ACS Nano*, vol. 8, no. 8, pp. 8407–8418, 2014.

[296] M. Ahmadi, S. S. Pramana, S. K. Batabyal, C. Boothroyd, S. G. Mhaisalkar, and Y. M. Lam, "Synthesis of Cu $_2$ SnSe $_3$ Nanocrystals for Solution Processable Photovoltaic Cells," *Inorg. Chem.*, vol. 52, no. 4, pp. 1722–1728, Feb. 2013.

[297] A. Lefranois, E. Couderc, J. Faure-Vincent, S. Sadki, A. Pron, and P. Reiss, "Effect of the treatment with (di-)amines and dithiols on the spectroscopic, electrochemical and electrical properties of CdSe nanocrystals' thin films," *J. Mater. Chem.*, vol. 21, no. 31, pp. 11524–11531, Aug. 2011.

[298] C. Querner, P. Reiss, S. Sadki, M. Zagorska, and A. Pron, "Size and ligand effects on the electrochemical and spectroelectrochemical responses of CdSe nanocrystals," *Phys. Chem. Chem. Phys.*, vol. 7, no. 17, pp. 3204–3209, Sep. 2005.

[299] J. De Girolamo *et al.*, "Layer-by-layer assembled composite films of side-functionalized poly(3-hexylthiophene) and CdSe nanocrystals: Electrochemical, spectroelectrochemical and photovoltaic properties," *Phys. Chem. Chem. Phys.*, vol. 10, no. 27, pp. 4027–4035, Jul. 2008.

[300] A. B. Rohom, P. U. Londhe, and N. B. Chaure, "Rapid thermal processed CuInSe2 layers prepared by electrochemical route for photovoltaic applications," *J.*
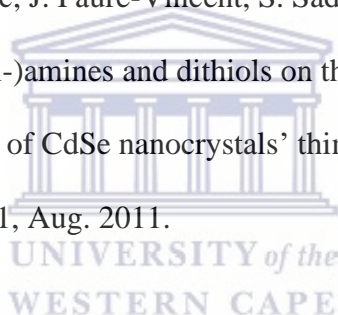
Electrochem. Soc., vol. 165, no. 4, pp. H3051–H3060, 2018.

[301] S. Das *et al.*, "Electrochemical Infilling of CuInSe $_2$ within TiO $_2$ Nanotube Layers and Subsequent Photoelectrochemical Studies," *ChemElectroChem*, vol. 4, no. 3, pp. 495–499, Mar. 2017.

[302] A. B. Rohom, P. U. Londhe, G. R. Bhand, M. G. Lakhe, and N. B. Chaure, "Study of electrochemically grown copper indium diselenide (CIS) thin films for photovoltaic applications," *J. Mater. Sci. Mater. Electron.*, vol. 27, no. 12, pp. 12374–12384, Dec. 2016.

[303] R. N. Bhattacharya, M. K. Oh, and Y. Kim, "CIGS-based solar cells prepared from electrodeposited precursor films," *Sol. Energy Mater. Sol. Cells*, vol. 98, pp. 198–202, Mar. 2012.

[304] A. Jana, K. N. Lawrence, M. B. Teunis, M. Mandal, A. Kumbhar, and R. Sardar, "Investigating the Control by Quantum Confinement and Surface Ligand Coating of Photocatalytic Efficiency in Chalcopyrite Copper Indium Diselenide Nanocrystals," *Chem. Mater.*, vol. 28, no. 4, pp. 1107–1120, Feb. 2016.

[305] Gamry, "Physical Electrochemistry & Equivalent Circuit Elements," 1988.